Overview of the Computational Fluid Dynamic Analyses of the Virginia Tech/NASA BeVERLI Hill Experiments

Thomas A. Ozoroski

Thesis submitted to the Faculty of the
Virginia Polytechnic Institute and State University
in partial fulfillment of the requirements for the degree of

Masters of Science
in
Aerospace Engineering

Christopher J. Roy, Chair
K. Todd Lowe
William J. Devenport

May 9th, 2022
Blacksburg, Virginia

Keywords: Turbulence Modeling, CFD, Separated Bump Flows, Validation Experiments,
Non-Equillibirum Flows

Overview of the Computational Fluid Dynamic Analyses of the Virginia Tech/NASA BeVERLI Hill Experiments

Thomas A. Ozoroski

(ABSTRACT)

Computational fluid dynamics (CFD) methods and schemes have been evolving at a rate that significantly outpaces the equipment needed to readily utilize them at scale. This lack of computational resources has resulted in an increased reliance on turbulence models and the need to know where turbulence models do well, where they do poorly, and where/how they can be improved upon. The BeVERLI Hill experiments aim to address this issue by providing experimental data that achieves a completeness level of three, which has never been done for this type of project. The experimental data collected is studied along side computational results from CFD solvers in order to help address and answer these questions. This paper provides an overview of the current computational status of the BeVERLI Hill project at Virginia Tech. The computational grids used for the analyses are presented such that the reader can gain an appreciation for the modeling techniques and methods being implemented. An analysis of the numerical error associated with the computational results is presented to provide confidence in the results obtained. An in-depth analysis will be presented that shows the results for the various grid levels that are being utilized to determine any grid based effects that are occurring within the solutions. Then, an analysis of the influence of the Reynolds numbers being run is shown. An investigation into the differences between the two different solvers being utilized, SENSEI and Fluent, is shown. An analysis of the effects on the solutions due to numerical limiters is presented to assist in increasing the computational efficiency of the workflow while not adversely affecting the results. Finally,

an analysis of the differences between the two turbulence models being utilized is presented. Computational results are compared to available experimentally obtained data to further motivate and identify flow features.

Overview of the Computational Fluid Dynamic Analyses of the Virginia Tech/NASA BeVERLI Hill Experiments

Thomas A. Ozoroski

(GENERAL AUDIENCE ABSTRACT)

An analysis has been done using high-fidelity computational fluid dynamic solvers that are utilized in order to solve for the flow over a three-dimensional bump called BeVERLI. An analysis is provided that discusses the use of different computational meshes, solvers, turbulence models, and numerical limiters within the computational tools to characterize the flow over the bump. An analysis of the estimated amount of numerical error within the solutions is provided along with a comparison to experimentally obtained data.

Dedication

I dedicate this to everyone who has supported my progression both academically and within CFD from my mentors at NASA, Virginia Tech, and most importantly my friends and family.

Acknowledgments

Many aspects of this work were sponsored by NASA's Transformational Tools and Technologies Project. I gratefully acknowledge the support provided by NASA through an NRA award, grant 80NSSC18M0146. The computational results obtained were run on Virginia Tech's Advanced Research Computing division on their flagship cluster Tinkercliffs and the dedication, support, and assistance through the years has been crucial. I would like to thank everyone on the BeVERLI team who has helped me along the way through advice with my computational results, providing experimental results, and for helping to answer questions I may have had. I would like to thank the SENSEI code development team for helping me along the way with any issues I ran into and for implementing all the changes that I desired over the years. I would like to thank Dr. Roy for providing me this opportunity so many years ago and for teaching me an extraordinary amount about producing good CFD results.

Contents

List of Figures

List of Tables

List of Abbreviations

δ	boundary layer thickness (m)
δ^*	displacement thickness (m)
$\hat{p}$	order of accuracy
μ	dynamic viscosity $(Pa - s)$
ρ_∞	freestream density (kg/m^3)
τ_x	X-direction surface shear stress (Pa)
θ	momentum thickness (m)
a	polynomial coefficient
C_f	friction coefficient
C_p	pressure coefficient
dCp	difference in pressure coefficient
h	bump height (m)
M_∞	freestream Mach number
P	pressure
$p_{0,in}$	stagnation pressure at the inlet (Pa)
p_{out}	static pressure at the outlet (Pa)

r	grid refinement factor
Re_H	Reynolds number with respect to the bump height
$T_{0,in}$	stagnation temperature at the inlet (K)
U_∞	freestream velocity (m/s)
w, w_{bump}	bump width (m)
w, w_{tunnel}	wind tunnel width (m)
x, y, z	Cartesian position variables
BeVERLI	Benchmark Validation Experiment for RANS/LES Investigations
CAD	Computer-aided design
CCW	Counter-clockwise
CFD	Computational fluid dynamics
CW	Clockwise
DE	Discretization error
FVM	Finite volume method
k-ω-SST	2003 Menter two-equation turbulence model
LDV	Laser doppler velocimetry
LES	Large-eddy simulation
OOA	Order of accuracy
PIV	Particle-image velocimetry

RANS	Reynolds-averaged Navier Stokes
SA-neg	Spalart-Allmaras negative turbulence model
VT SWT	Virginia Tech Stability Wind Tunnel

Chapter 1

Introduction

1.1 Outline

The first chapter provides background and context to the work being done currently and what is being presented. The second chapter focuses on the methodology and the computational domain setup, the estimation of computational errors, and the results obtained during the analysis. The third chapter focuses on a discussion and conclusion of the results that were presented within the second chapter.

1.2 Contribution

A method of estimating the numerical error associated with the SENSEI computational solutions on the surface and within the flow field is developed. A method of referencing the computational data to be consistent and unambiguous is presented. An analysis of the grid levels generated and the differences within the results obtained is done. A comparison between the different Reynolds numbers run and the effect these changes have on the flow is identified. The numerical differences that appear due to different turbulence models, numerical solvers, and numerical limiters is presented to help understand complex flow features.

1.3 Attribution

Since a manuscript is being presented, Chapter 2 is attributed to multiple authors. A brief summary of their contributions is presented here:

- Aldo Gargiulo (Second Author): The second author contributed the computational grids that were used for the analyses presented and provided the CAD images that were used. The second author also assisted in the obtainment of the experimental pressure data within the Virginia Tech Stability Wind Tunnel.
- Tom Hallock (Third Author): The third author contributed the Fluent results that are shown within the paper and assisted in the obtainment of the experimental pressure data within the Virginia Tech Stability Wind Tunnel.
- Julie Duetsch-Patel (Fourth Author): The fourth author contributed the uncertainty bands for the experimental data shown, provided the CAD images that were used, and assisted in the obtainment of the experimental pressure data within the Virginia Tech Stability Wind Tunnel.
- Vignesh Sundarraj (Fifth Author): The fifth author assisted in the obtainment of the experimental pressure data within the Virginia Tech Stability Wind Tunnel.
- Christopher Roy (Sixth Author): The sixth author contributed valuable feedback and suggestions that helped to guide the work while serving as the main advisor.
- William J. Devenport (Seventh Author): The seventh author contributed valuable feedback and suggestions that helped to guide the direction of the work.
- K. Todd Lowe (Eighth Author): The eighth author contributed valuable feedback and suggestions that helped to guide the direction of the work.

- Aurelien Borgoltz (Ninth Author): The ninth author contributed valuable feedback and suggestions that helped to guide the direction of the work.

Chapter 2

CFD Analysis of the BeVERLI Hill Turbulence Model Validation Experiments

Thomas Ozoroski[*], Aldo Gargiulo[†], Tom Hallock[*], Julie Duetsch-Patel[†], Vignesh Sundarraj[*], Christopher J. Roy[‡], William J. Devenport[‡], Todd Lowe‡, Aurelien Borgoltz[¶]

2.1 Abstract

Wind tunnel tests and computational fluid dynamics simulations have been conducted in an effort to fully characterize the flow around a novel superelliptic-shaped hill called BeVERLI (BEnchmark Validation Experiment for RANS/LES Investigation.) The goal of the BeVERLI Hill set of experiments is to produce detailed experimental data to meet the requirements of the highest level of CFD validation per the guidelines set by Oberkampf and Smith [1]. The computational domain has been set up to represent the experimental con-

---

[*] Graduate Researcher, Crofton Department of Aerospace and Ocean Engineering, AIAA Student Member

[†] Graduate Research Assistant, Crofton Department of Aerospace and Ocean Engineering, AIAA Student Member

[*] Graduate Researcher, Crofton Department of Aerospace and Ocean Engineering, AIAA Student Member

[*] Graduate Researcher, Crofton Department of Aerospace and Ocean Engineering, AIAA Student Member

[‡] Professor, Crofton Department of Aerospace and Ocean Engineering, AIAA Associate Fellow

[¶] Research Associate Professor, Crofton Department of Aerospace and Ocean Engineering, AIAA Member ditions and has been systematically refined to create a family of four grids that are used for analyzing discretization errors. A method for obtaining the discretization error and the iterative error of the grids has been used to further support the computational results. An iterative error analysis is conductive to determine a necessary convergence criteria. A comparison of the different grid levels being used and the effects on flow topology and a comparison to experimental data is shown. The effects of different numerical solvers, limiter schemes, and RANS based turbulence models are presented. The flow behavior through the Reynolds number sweep being examined is presented and a comparison to experimental data is conducted.

2.2 Introduction

With the ever-increasing reliance on CFD results and analyses to drive design and predictions, the ability of current turbulence modeling techniques to compute accurate results is still an ongoing challenge [2, 3]. Currently, more fundamental methods of computing turbulence like direct numerical simulations and large eddy simulations can require billions of grid points and be computationally expensive to run even for simple cases [4]. The exact limits for where turbulence modeling can still provide accurate and trustworthy results for RANS based CFD is still largely case dependent [2]. With CFD being an integral part of innovation and research as a way to decrease the costs typically incurred by wind tunnel testing, the need to assess the reliability of any turbulence modeled result is crucial.

Due to the sensitivity of turbulence and computational models to many different conditions within the computational domain, it is often difficult to confirm whether the results being computed are physical. In order to properly investigate the capabilities of turbulence modelling and the computationally derived results, they must be validated against benchmark problems that are able to provide insight into where the models succeed and where they fail [5, 6]. Validation efforts have been conducted previously but are often lacking fully described experimental conditions that would be needed for a CFD researcher to correctly define the problem. Important conditions such as velocity or pressure across the inflow boundary, the inflow boundary layer height, or obtaining a model of the as-built geometry for simulations are not always available. This lack of precise flow characteristics and geometry results in uncertainties accumulating throughout the computation as well as within the experiment and makes the process of validating any turbulence model more challenging.

The NASA/Virginia Tech Benchmark Experiments for Computational Fluid Dynamics is an ongoing experimental and computational effort being performed in Virginia Tech's Stability Wind Tunnel. The ongoing collaboration between NASA Langley Research Center and Virginia Tech aims to address turbulence model validation issues by employing a team of experimentalist and CFD researchers [7]. Additionally, the BeVERLI Hill case has been recently considered by a group within the Science and Technology Organization (STO) of the North Atlantic Treaty Organization (NATO), under the title NATO AVT-349 - ”Non-Equilibrium Turbulent Boundary Layers in High Reynolds Number Flow at Incompressible Conditions”, whose goal is the advancement of the accuracy and range of prediction models for high Reynolds number non-equilibrium boundary layers. The project is guided by the collaboration between experimentalists and CFD researchers which motivates the need for accurate experimental and modeling conditions as to best reduce the uncertainty that would otherwise exist. To provide an effective way of reducing the uncertainty of the experimental and computational results, the experiments are driven by the goal of meeting the necessary requirements for CFD validation as defined by Oberkampf and Smith [1].

The results given in this paper will preset a summary of the CFD efforts ongoing as well as nominal experimental results from one of the full-scale wind tunnel tests to motivate the investigation. The ongoing CFD efforts will focus on the grids that have been generated, the method in which numerical error will be estimated, and current CFD results computed. The experimental data presented will be a brief portrayal of the nominal 45° rotations and will be used to supplement the validation efforts. The paper includes an in-depth analysis of the computational results of the BeVERLI Hill under a variety of different numerical schemes, limiters, conditions, and models.

2.3 Methodology

2.3.1 Experimental Setup

The BeVERLI Hill geometry is defined by Gargiulo et al. [8] and is represented in Fig. 2.1. It is defined as a 5th degree polynomial centerline profile, superelliptic corners, and a squared flat top of width $s = 0.093472\,\text{m}$. The hill width is $w = 0.93472\,\text{m}$ and has a height of $H = 0.186944\,\text{m}$ (aspect ratio $= w/H = 5$).

The VT Stability Wind Tuennel (SWT) is a continuous, single return, subsonic wind tunnel that can produce maximum sustained speeds of 80 m/s and can produce turbulent intensity levels in the freestream as low as 0.01%-0.03% [7]. Its test section is nominally rectangular with a 1.83 m by 1.83 m cross section and a length of 7.30 m. The BeVERLI Hill is mounted at the center of the port-side wall of the test section and can be seen in Figure 2.2. A Cartesian coordinate system is used with the origin being located at the center of the hill on the port-side wall and is consistent between the experimental and computational results. The x-axis coincides with the streamwise flow direction, the y-axis is in the wall-normal direction, and the z-axis is chosen to represent the spanwise direction to enforce a right-handed coordinate system. The Reynolds number for the experiment is based on the nominal height of the

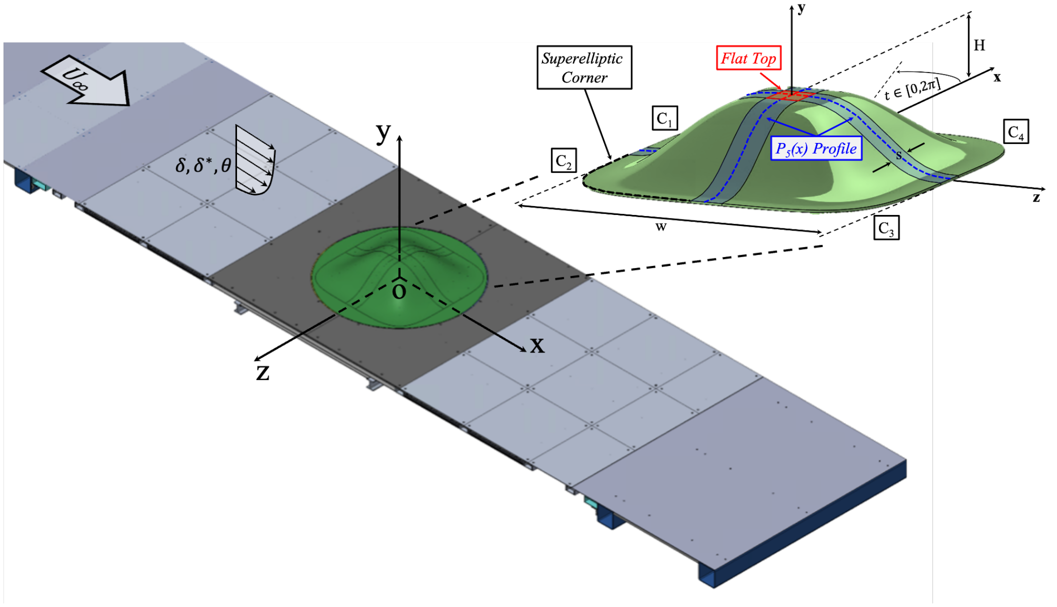

Figure 2.1: The BeVERLI Hill geometry. On the left, a wall-mounted representation of the BeVERLI Hill is illustrated along with a corresponding Cartesian coordinate system. The flow direction and a schematic of the incoming boundary layer are included. On the right, a detail view of the BeVERLI Hill geometry is depicted.

bump and is denoted as Re_H. The nominal tunnel test conditions to be analyzed within the paper are for $Re_H = 250K$, $Re_H = 325K$, and $Re_H = 650K$. The reference conditions that the three height based Reynolds numbers produce experimentally and then subsequently matched within the computational solutions are presented in Table 2.1. The $Re_H = 325K$ condition does not include experimental data for this paper.

2.3.2 Computational Domain

The computational domain employed by Virginia Tech is shown in Figure 2.3 and represents the idealized geometry of the stability wind tunnel. The computational domain is extended upstream in the -X direction by 6.5 m in order to approximately model the inflow boundary layer based on previous analyses and lies outside of the bump influence due to blockage.

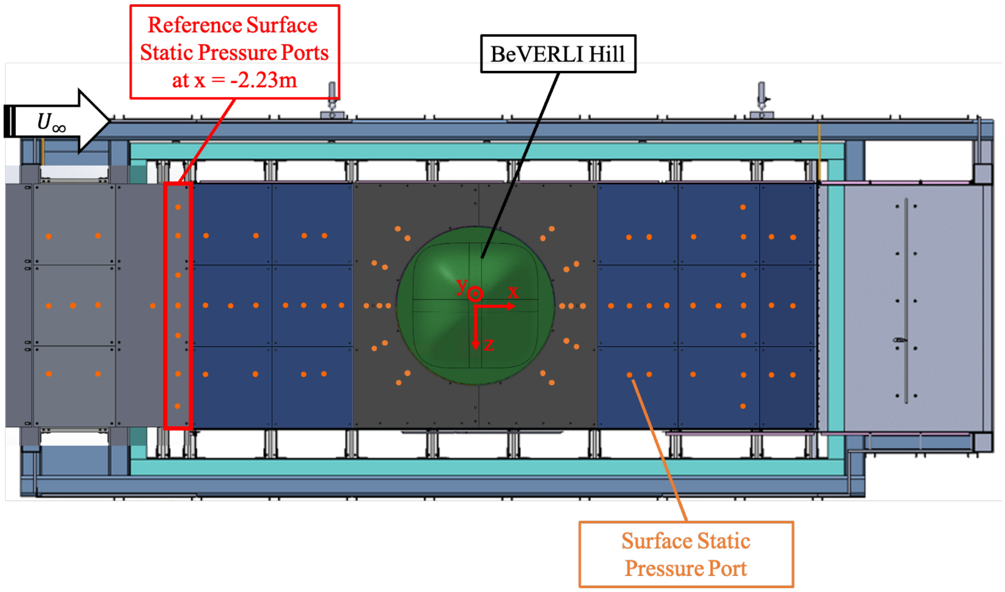

Figure 2.2: Schematic of the VT SWT test section when the bump is mounted in the tunnel. Top left: test section side view; Bottom left: contraction and test section top view; Right: Test section cross section with flow coming out of the page. The associated table provides the target-scale flow parameters.

Additionally, the domain is extended in the +X direction by 5.5 m in order to ensure that any effects seen from the bump are not influenced by the outlet domain. The domain models the wind tunnel to have a width and height of 1.83 m and is constant throughout the computational domain length. The bump represents the as built geometry as shown in Figure 2.1 and does not include the manufacturing flaws that are present on the bump. Future computations do intend to use the as built geometry but the results shown do not implement the laser scanned geometry of the model.

2.3.3 Boundary and Reference Conditions

The boundary conditions as employed by Virginia Tech and their location for the target-scale hill-height-based Reynolds number are shown in Table 1. A stagnation temperature $T_{0,in}$ and stagnation pressure $p_{0,in}$ are obtained experimentally and defined along the inlet of the computational domain. They are found by averaging the experimental data for 4 similar runs and conditions. Then, based upon the experimentally obtained reference ports that are located -2.223 m upstream of the nominal bump center on the opposite wall, a reference pressure is obtained. Once a know static pressure P_{ref} for the experiment is known, a range of static pressure are applied to the domain outlet. The Z-location of the seven reference points are at Z = (-0.6858, -0.4572, -0.2286, 0, 0.2286, 0.4572, 0.2286)m. Based upon the average static pressure that is obtained computational for the different static outlet pressure, a linear fit for the data is obtained and the desired reference pressure is solved for to define the outlet pressure. Once that reference pressure is the same between the experiment and the computations, the boundary conditions are set for the computations. This is done by first averaging the values of the reference ports to generate a value for P_{ref}. Then by using Equations 2.1, 2.2, 2.3, and 2.4 the necessary reference values are solved for within the ambiguity of freestream flow conditions.

$$M_{ref} = \sqrt{\frac{P_0}{P_{ref}}^{\frac{\frac{\gamma-1}{\gamma}-1}{\frac{\gamma-1}{2}}}} \tag{2.1}$$

$$T_{ref} = \frac{T_0}{1+\frac{\gamma-1}{2}} * M_{ref}^2 \tag{2.2}$$

$$U_{ref} = M_{ref} * \sqrt{\gamma * R * T_{ref}} \tag{2.3}$$

$$\rho_{ref} = \frac{P_{out}}{R * T_{ref}} \tag{2.4}$$

The reference values that have been solved for are then used to non-dimensionalize values of pressure and surface shear to obtain $C_{p,ref}$ and $C_{f,ref}$ using Equation 2.5 and Equation 2.6 respectively. Where P_{ref} is the reference value at the port locations for each case independently since some variation can occur and P and τ are the values within the flow or on the surface.

$$C_{p,ref} = \frac{P - P_{ref}}{\frac{\gamma}{2} * P_{ref} * M_{ref}^2} \tag{2.5}$$

$$C_{f,ref} = \frac{\tau}{\frac{1}{2} * \rho_{ref} * U_{ref}} \tag{2.6}$$

The remaining parts of the computational domain are modeled as a smooth no-slip wall. The flow is modeled to be a compressible ideal gas where the viscosity is defined using Sutherlands law to define dynamic viscosity [9].

Table 2.1: Boundary and reference conditions for the three height-based Reynolds numbers

Boundary and Reference Conditions			
Re_H	$Re_H = 250$K	$Re_H = 325$K	$Re_H = 650$K
$P_{0,in}(Pa)$	94,220	94,275	94,450
$T_{0,out}(K)$	297	297	297
$P_{out}(Pa)$	93,961	93,845	92,692
$P_{ref}(Pa)$	93,974	93,866	92,771
$U_{ref}(m/s)$	21.11	27.23	55.22
$\rho_{ref}(kg/m^3)$	1.1031	1.1023	1.0930
$T_{ref}(K)$	296.8	296.6	295.5
M_{ref}	0.0611	0.0789	0.1603

2.3.4 Computational Meshes

The meshing process was conducted and the grids were generated using the commercial software Pointwise [10]. The meshes were designed to be denser near the bump geometry as

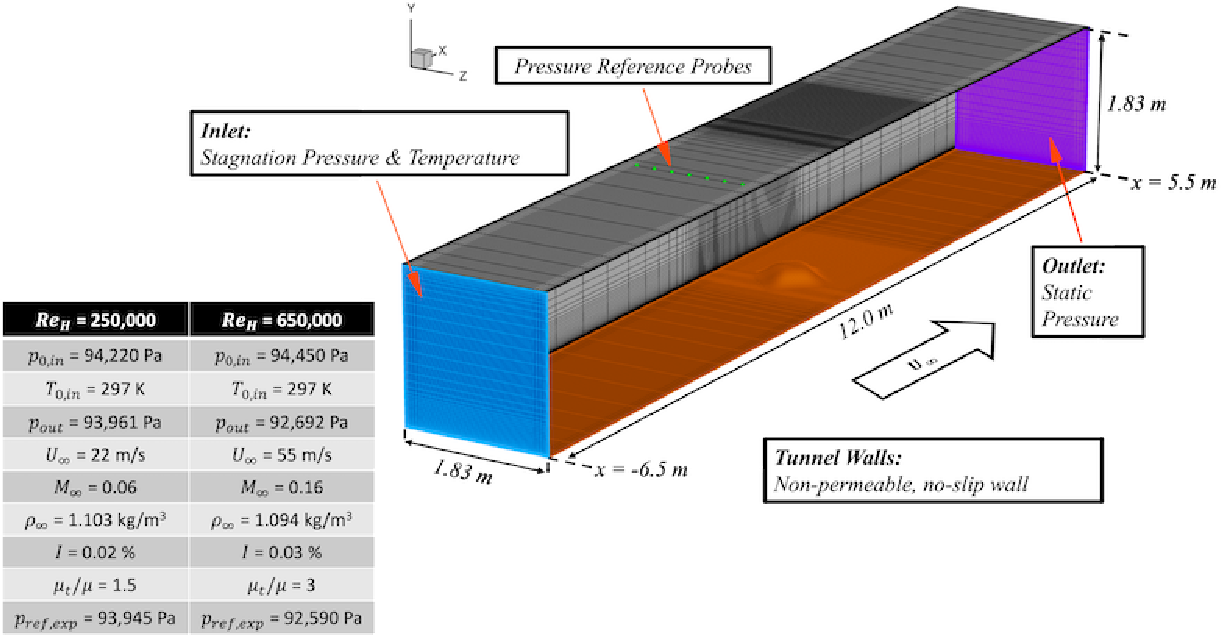

Re_H = 250,000	Re_H = 650,000
$p_{0,in}$ = 94,220 Pa	$p_{0,in}$ = 94,450 Pa
$T_{0,in}$ = 297 K	$T_{0,in}$ = 297 K
p_{out} = 93,961 Pa	p_{out} = 92,692 Pa
U_∞ = 22 m/s	U_∞ = 55 m/s
M_∞ = 0.06	M_∞ = 0.16
ρ_∞ = 1.103 kg/m^3	ρ_∞ = 1.094 kg/m^3
I = 0.02 %	I = 0.03 %
μ_t/μ = 1.5	μ_t/μ = 3
$p_{ref,exp}$ = 93,945 Pa	$p_{ref,exp}$ = 92,590 Pa

Figure 2.3: Three-dimensional view of the computational domain with the boundary conditions identified, the experimental freestream conditions are shown.

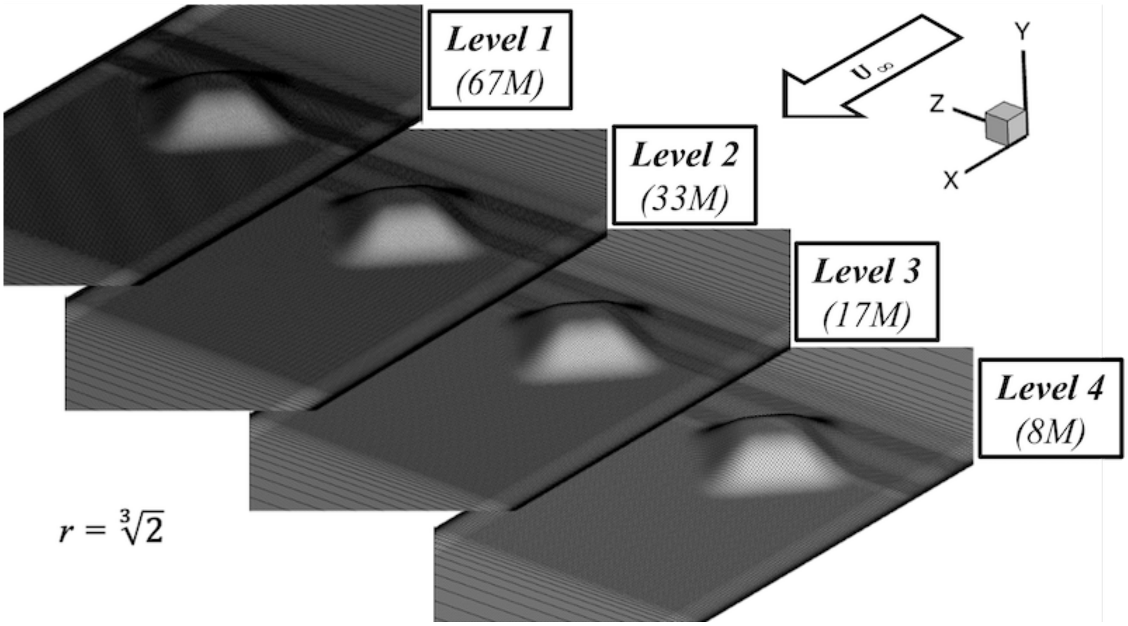

Figure 2.4: Three-dimensional view of the surface of the computational grid of the BeVERLI Hill. The finest grid, Level 1, is on the top and gets consistently coarser moving down to the coarsest grid, Level 4.

well as the inflow and outflow planes as to decrease the numerical uncertainties. The grid is highly clustered within the expected boundary layer region to assist the comparison to experimentally obtained data and assist in near wall boundary layer effects. The finest grid was systematically refined to produce three additional levels of numerical grids to allow for flexibility in computational costs as well as comparison to experimental data and obtaining the discretization error. The four grid levels generated were defined as Level 4 to Level 1 with the Level 4 grid being the coarsest of grids and Level 1 being the finest grid. The grid levels are $465 \times 353 \times 409$ (Level 1), $369 \times 281 \times 325$ (Level 2), $293 \times 223 \times 259$ (Level 3), and $233 \times 177 \times 205$ (Level 4). The aforementioned grid levels generated can be seen in Figure 2.4 where the finest grid is on the top and is systematically refined moving down to the coarsest grid. Each level is generated starting from the finest Level 1 grid an utilize a refinement factor of $r = \sqrt[3]{2}$ for each level to systematically coarsen and obtain each subsequent grid level down to the coarsest Level 4 grid. The systematically refined grids were generated to accurately estimate the discretization errors of the solution on each grid.

2.3.5 Numerical Solvers and Turbulence Models

Currently two different CFD solvers are being used by the project to obtain numerical results, the Virginia Tech in-house solver SENSEI [11, 12] and the ANSYS commercially available solver Fluent [13]. SENSEI is a fully structured cell-centered compressible FVM solver and has gone through extensive code verification done by Jackson et al. [11] and Xue et al. [14]. In SENSEI, the inviscid flux discretization was performed using Roe's flux difference splitting [15] with MUSCL extrapolation to achieve a second-order accurate scheme. The viscous and turbulent fluxes were discretized to second-order accuracy using a central flux scheme after applying the Green-Gauss theorem. Unless otherwise noted, the SENSEI results were run without the use of any limiters while the ANSYS Fluent results utilized the

Barth-Jesperson limiter [13]. In ANSYS Fluent, the available density-based solver using an algebraic multigrid method was used to solve the RANS equations numerically. The spatial discretization of the inviscid fluxes was performed using a second-order updwind scheme. Fluent achieves second-order accuracy using a multidimensional linear reconstruction approach [16]. The viscous and turbulent fluxes in Fluent were discretized to second-order accuracy using a central flux scheme and the Green-Gauss theorem. All computational results utilize the aforementioned grids in coordination with a finite volume method RANS scheme utilizing the negative Spalart-Allmaras (SA-neg) [17] one-equation eddy-viscosity model and the Menter $k - \omega$ SST (2003) two-equation eddy-viscosity model [18].

2.4 Error Estimation

2.4.1 Discretization Error

The discretization error analysis was conducted using the Level 2 and Level 3 $Re_H = 250K$ results from SENSEI using SA-neg with no limiters. Again, a refinement factor $r = \sqrt[3]{2}$ was used to coarsen the grid levels. Initially, the results for Level 4 were to be used, but due to complications with resolving $C_{p,ref}$ within the separated region, a local order of accuracy could not be established due to the solutions for each subsequent grid level resulting in a non-asymptotic grid convergence. Additionally, the computation of the Level 1 grid proved difficult to converge to the residual levels needed to establish confidence in the solution with the respective refinement factor. Additionally, the computational scheme was run 2^{nd} order for the entirety of the computation with the mean flow residuals converging to approximately machine zero for a reduction of 10 orders of magnitude and the turbulence residuals converging approximately 8 orders. In order to obtain the discretization estimates, $C_{p,ref}$ was chosen to be analyzed along the surface. The Level 2 surface solution was interpolated onto the Level 3 surface grid in order to obtain nodal interpolated values. The solution interpolation, although not shown, resulted in negligible differences between the true Level 2 solution and the interpolated solution. Since only two grid levels were being used to conduct the analysis and asymptotic behavior could therefore not be proven, a factor of safety was applied of $F.S. = 3$ as suggested by Roache [19].

$$\bar{f}_{i,j} = f^2_{i,j} + \frac{f^2_{i,j} - f^3_{i,j}}{r^{\hat{p}} - 1} \tag{2.7}$$

where $\bar{f}_{i,j}$ is the estimated exact solution for a flow value at a specific grid point in the 2D plane and $\bar{f}^k_{i,j}$ is the solution for Level $k = 2, 3$. Using a Richardson extrapolation in accordance with Eq. 2.7 an assumed observed order of accuracy was chosen and is shown along the centerline for $OOA = 1.0$ and $OOA = 1.5$ in Figure 2.5 [20]. It is seen that the difference between assuming an observed order of accuracy for the two values used produces only small differences within the exact solution with the largest variations occurring where separation occurs and within the wake.

Using the exact solutions generated for the observed order of accuracy's, the absolute value of the discretization error multiplied by the factor of safety was analyzed along the centerline of the bump for the Level 2 interpolated solution to obtain a discretization uncertainty. The results of this analysis of discretization uncertainty along the centerline can be seen in Figure 2.5. The DE is seen to rise rapidly after $x/H = 0$ up to the maximum location of DE at approximately $x/H = 1$ before dropping almost asymptotically. This large value for discretization uncertainty occurs due to the separation location of the wake moving as the grid becomes more refined. The DU increases again starting around $x/H = 2$ as $C_{p,ref}$ within the wake and recovery region highly depends on the grid resolution.

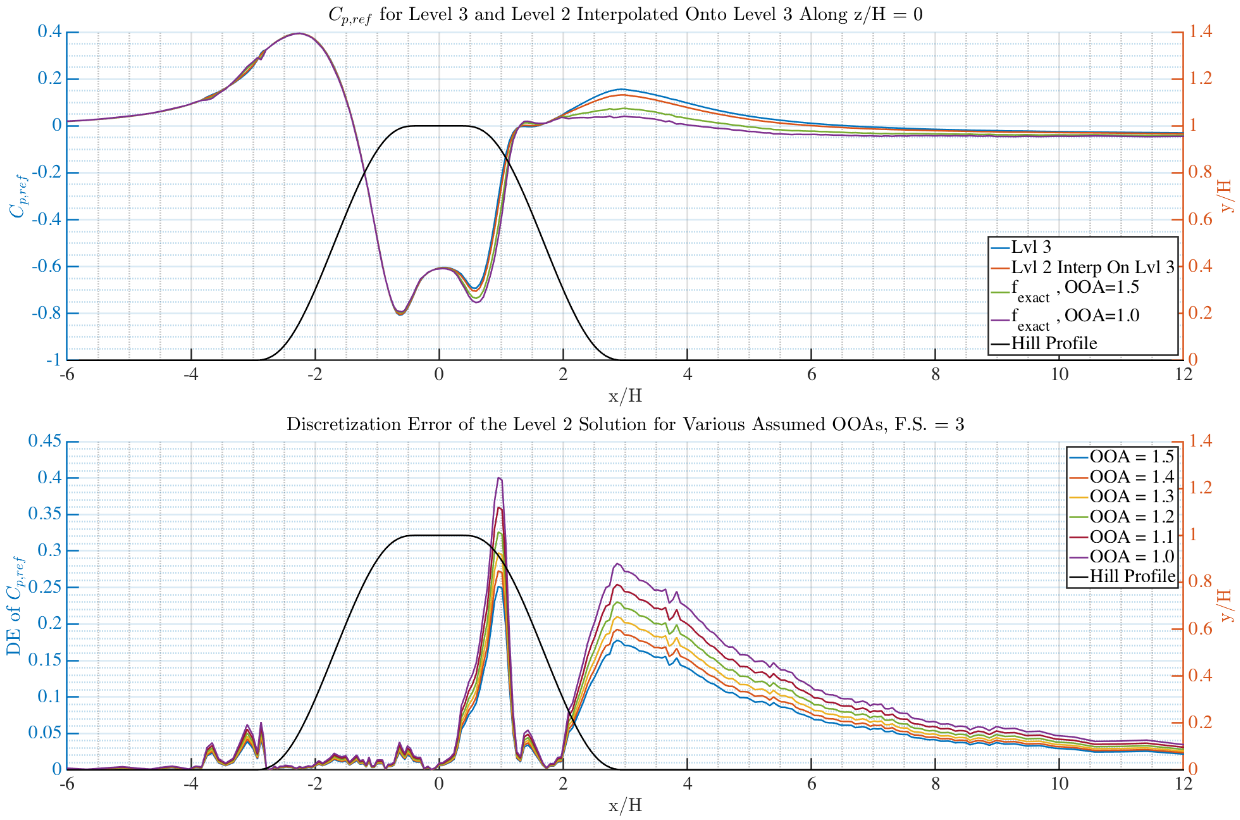

$C_{p,ref}$ for Level 3 and Level 2 Interpolated Onto Level 3 Along z/H = 0

Discretization Error of the Level 2 Solution for Various Assumed OOAs, F.S. = 3

Figure 2.5: Discretization uncertainty of $C_{p,ref}$ on Level 2 for the $Re_H = 250K$, 45° case and the SA-neg turbulence model along the centerline $z/H = 0$. Uses the Level 2 results interpolated onto Level 3 with the Level 2 discretization uncertainty shown on the Level 3 mesh with an assumed OOA = 1.5 with a factor of safety F.S. = 3.

Table 2.2: Maximum and minimum values for the Discretization uncertainty of $C_{p,ref}$ along the centerline and bump surface.

DU of $C_{p,ref}$		
Analysis	max(DE $C_{p,ref}$)	min(DU $C_{p,ref}$)
Centerline	0.25149	2.187E-04
Surface	0.26702	≈0

Since the entirety of the Level 2 surface solution was interpolated onto the Level 3 mesh, the discretization uncertainty was analyzed along the entirety of the surface for $C_{p,ref}$ instead of just along the centerline. This analysis was conducted using the same method as described

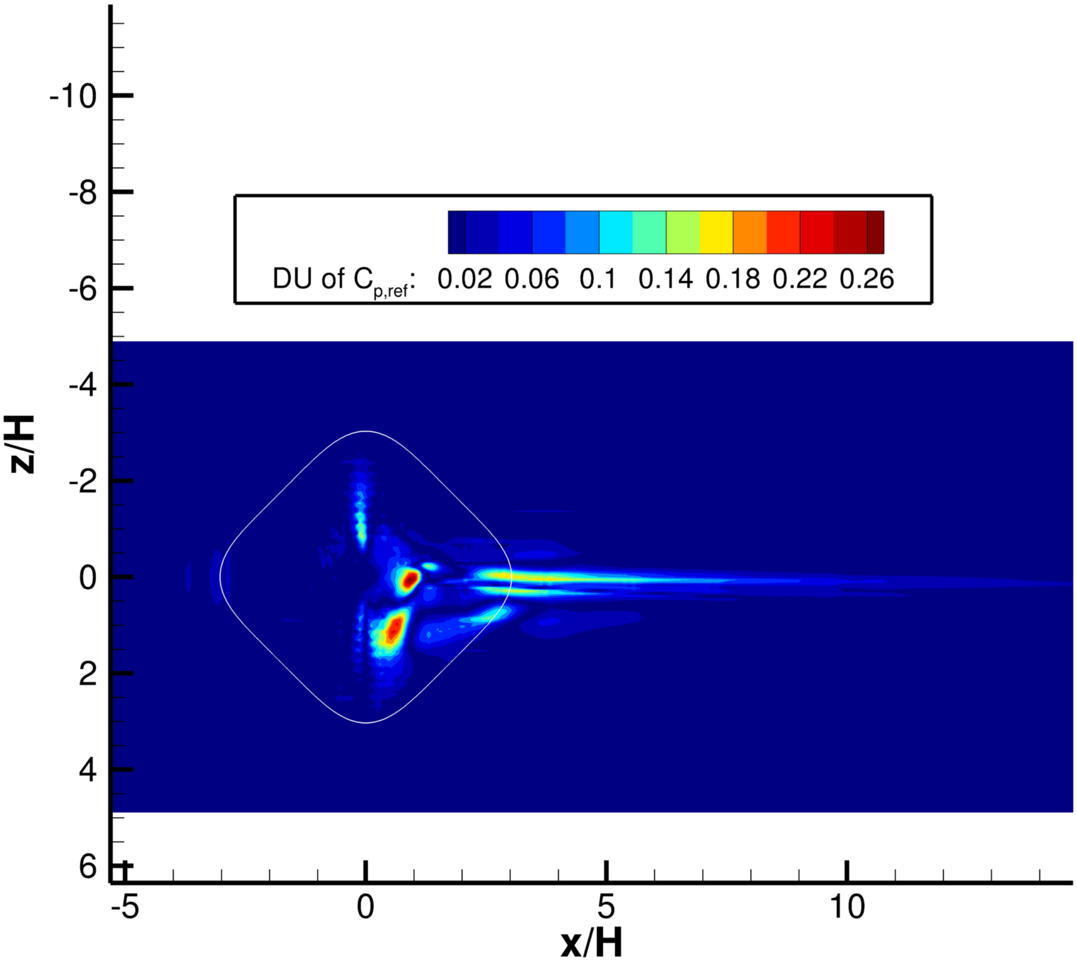

Figure 2.6: Discretization uncertainty of $C_{p,ref}$ on the Level 2 mesh for a Reynolds number of $Re_H = 250K$ at 45° using the SA-neg turbulence model. The estimation uses the Level 2 results interpolated onto the Level 3 grid before analyzing the Level 2 Discretization uncertainty on the Level 3 mesh with an assumed OOA = 1.5 and factor of safety F.S. = 3.

previously, but was done over a 2-D surface instead of a 1-D line. The results for the surface discretization uncertainty analysis using an observed order of accuracy of $OOA = 1.5$ and a factor of safety of $F.S. = 3$ are shown within Figure 2.6. The global surface analysis produces a centerline DU estimation that lines up exactly with what is shown in Figure 2.5 verifying the 2-D analysis.

The 2-D surface DU analysis shows that the majority of the error occurs after $x/H = 0$ primarily in the wake region of the flow. As discussed later, the difference in the flow topology due to an increased grid resolution produces large discretization uncertainties on the surface. Additionally, the centerline DU analysis captures the region of largest error along the surface. The maximum and minimum values of discretization uncertainty over the surface and along the centerline are shown in Table 2.

2.4.2 Iterative Error

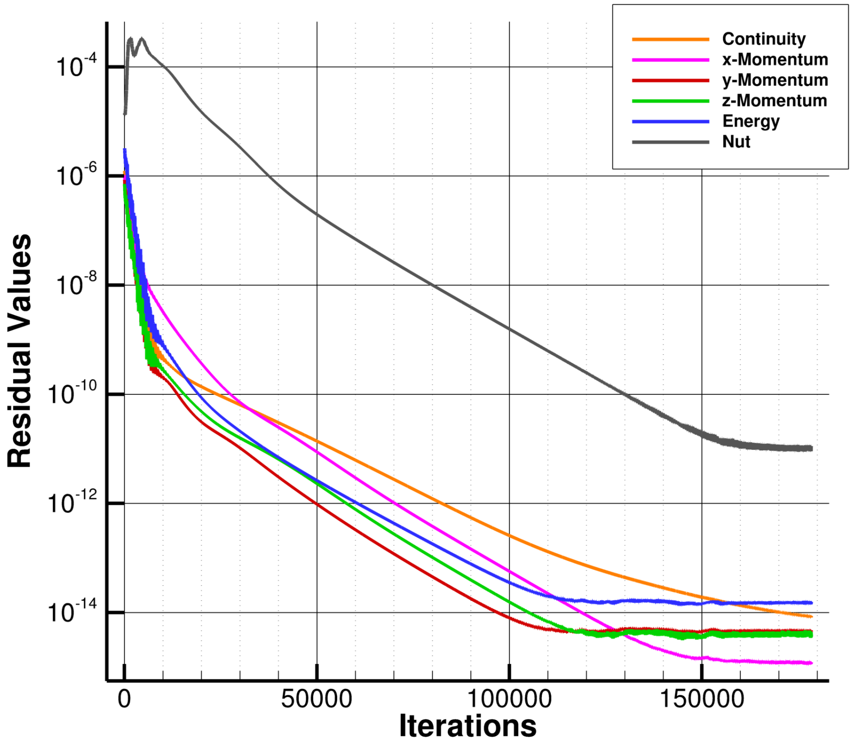

Figure 2.7: L_2 Norm iterative residuals for the Level 3 $Re_H = 650K$ SENSEI SA-neg case used for the iterative error analysis.

Table 2.3: Iterative convergence for the discretized mean flow and turbulence equations for the Level 3 $Re_H = 650K$ SENSEI SA-neg case.

Iterative Convergence Levels						
Iteration	Continuity	X-Momentum	Y-Momentum	Z-Momentum	Energy	Nut
0	1.228e-06	1.0355e-06	8.4395e-07	7.1694e-07	3.221e-06	1.402e-05
30,000	6.418e-11	7.1374e-11	1.0397e-11	1.5834e-11	2.107e-11	3.377e-06
60,000	6.213e-12	2.9471e-12	3.2863e-13	7.7817e-13	1.049e-12	6.962e-08
64,000	4.321e-12	1.8264e-12	2.0704e-13	4.8484e-13	7.028e-13	4.457e-08
90,000	5.480e-13	1.4589e-13	1.7957e-14	3.9450e-14	7.771e-14	3.952e-09
97,000	3.111e-13	7.2456e-14	9.5901e-15	1.9721e-14	4.299e-14	1.991e-09
120,000	7.262e-14	8.9499e-15	4.6754e-15	4.4355e-15	1.600e-14	2.475e-10
128,000	4.693e-14	4.2799e-15	4.9139e-15	3.9440e-15	1.609e-14	1.129e-10
150,000	1.894e-14	1.4493e-15	4.5053e-15	3.7363e-15	1.462e-14	1.737e-11
178,000	8.489e-15	1.2237e-15	4.4877e-15	3.8600e-15	1.573e-14	1.086e-11

The iterative error ϵ_h^k is defined as the difference between the iterative solution u_h^k and the exact solution u_h where there exact solution is assumed to be equal to the final fully converged solution.This is shown mathematically within Eq. 2.8.

$$\epsilon_h^k = u_h^k - u_h \tag{2.8}$$

The fully converged solution was obtained by running the simulation until the iterative residuals of the mean-flow equations entered the round off region around 1 e-15. The iterative error analysis was conducted using the Level 3 mesh with a corresponding Reynolds number of $Re_H = 650K$. Four profiles were obtained at different regions within the flow where turbulence models struggle such as where the flow is separated, under strong pressure gradients, and along regions of high curvature. From this, profiles were obtained vertically within the domain from the surface up until half the domain height of 0.915 m. The respective intermediary iterative solutions were obtained at 8 convergence levels between $Iter = 0$ and $Iter = 178K$. Following Eq. 2.8, the difference between the assumed exact solution and the respective solution for the obtained convergence level was calculated for each point within the profile. The iterative error was calculated for a discrete iterative step and respective convergence level since the profile could not be obtained for every iterative step.

The iterative error was analyzed for the following quantities: density (ρ), reference coefficient of pressure ($C_{p,ref}$), temperature (T), (U, V, W)-velocity components, turbulent eddy viscosity (μ), and Mach number (M). Solutions were outputted for Iterations: 0, 30,000, 60,000, 64,000, 90,000, 97,000, 120,000, 128,000, 150,000 and 178,000 where the final solution of 178,000 was used as the exact solution. Within the analysis plots shown in the appendix, $(Y1, X1, Z1)$ represent the starting location of the extracted profile while $(Y2, X2, Z2)$ represent the ending location of the extracted profile. The locations where the profile solutions were outputted can be seen in the Appendix.

Based upon the iterative error analysis, a convergence criteria was chosen of 1e-13 for the mean flow equations and of 5e-10 for the turbulence equation. This convergence criteria results in a maximum iterative error for $C_{p,ref}$ that is on the order of 1e-6 %. The iterative error obtained for the coefficient of pressure is similar to that seen for the other mean flow quantities within the wake. Due to the iterative error being so low for all quantities of interest, the iterative error is negligible to the overall error once the convergence criteria is met.

2.5 Results

2.5.1 Grid Level Comparison

Results have been obtained for each Reynolds number on grid levels 1,2, and 3 in order to analyze changes within the solution as the grids become more refined. This will be done by investigating the differences in the $C_{p,ref}$ profiles along the centerline Z = 0 and the centerspan X = 0 where there is available experimental data. Next, an analysis of the asymmetry of the solutions along the spanwise section will be analyzed. Finally, an examination of the surface topology will be conducted in order to visualize changes to focal structures and separation behavior.

Cp Profiles

The surface profiles for the coefficient of pressure are plotted for the lowest Reynolds number in Figure 2.8 where the centerline is seen in Figure 2.8a and the centerspan is seen in Figure 2.8b. Looking at the differences between the Level 2 and Level 3 results for the centerline first in Figure 2.8a, it is seen that both levels are extremely similar for the majority of the plot. The Level 2 case produces a slightly lower $C_{p,ref}$ value before separation than the Level 3 case does. Both cases predict the $C_{p,ref}$ values up until separation extremely well, but do not do as great predicting the $C_{p,ref}$ values within the separated region. It is seen that the Level 3 case separates slightly before the Level 2 case does and predicts a lower value of $C_{p,ref}$ immediately after. Within the separated region, the Level 2 case predicts a lower value of $C_{p,ref}$ than Level 3 does with this behavior continuing through the rest of the domain shown. Moving onto the centerspan distribution in Figure 2.8b, it is seen that there are almost no differences in the entirety of the domain between the two levels. The Level 2 result predicts a slightly lower value of $C_{p,ref}$ at the location of lowest pressure around $z/H = 1.25$. Both grid levels again do an extremely good job at capturing the $C_{p,ref}$ distribution seen experimentally. The only regions in which noticeable differences arise for both grid levels is at the location of minimum pressure where both grids fail to fully predict the minimum $C_{p,ref}$ value seen experimentally. This difference though is extremely small and represents around a difference in $C_{p,ref}$ of around 0.05.

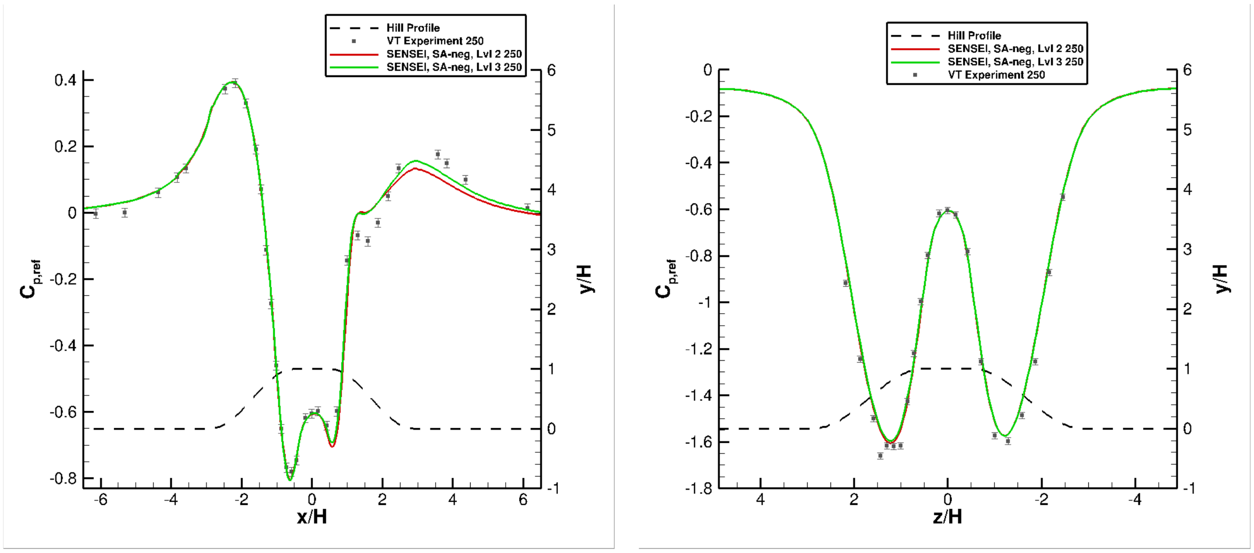

(a) Centerline

(b) Centerspan

Figure 2.8: SENSEI SA-neg centerline and centerspan $C_{p,ref}$ distributions on grid Level 2 and 3 for a Reynolds number of $Re_H = 250K$.

The surface profiles of the coefficient of pressure for the middle Reynolds number of $Re_H = 325K$ are plotted in Figure 2.9 where the centerline is seen in Figure 2.9a and the centerspan is seen in Figure 2.9b. Looking at the centerline plot first, it is seen that all of the values for $C_{p,ref}$ appear to be collocated up until around $x/H = 0$. After this location, it is seen that the Level 3 result diverges from the Level 1 and 2 result and does not generate as low of a $C_{p,ref}$ value before separation. This is most likely caused by the flow separating earlier for Level 3 than for Levels 1 and 2. The Level 3 $C_{p,ref}$ value within the separated region behaves differently than the other two levels. It appears that, regardless of the overall value of $C_{p,ref}$, that as the grids become more refined, there is less of a decrease of $C_{p,ref}$ immediately after separation. Moving past the separated region, the $C_{p,ref}$ value within the high curvature region on the leeward side of the bump is seen to decrease as the grids become more refined. Even though the pressure recovery region after separation trends upwards, the $C_{p,ref}$ within the high curvature region trends downwards. This behavior continues through the rest of the plot past $x/H = 6$. Furthermore, the results are insightful into the difficulties with obtaining an asymptotically converged grid solution throughout the entirety of the domain. It is seen that up until around $x/H = 1.5$, that the Level 1 and 2 solutions mimic each other extremely close, but this behavior does not last long after separation as Levels 2 and 3 begin to trend closer to each other and further from Level 1.

Looking now at the centerspan $C_{p,ref}$ profile in Figure 2.9b, Levels 1, 2, and 3 are plotted along X = 0. It is seen that around $z/H = 1.25$ the value of $C_{p,ref}$ at the global minimum continues to trend downwards as the grid becomes more refined. The changes only present themselves on the region half way up the hill to the high curvature region, before the flat top. Here, it is seen that the Level 2 and 3 solutions are much closer together than the Level 1 solution, but that the differences between them all are extremely minimal. It is also seen that the same region on the negative z/H region of the bump presents the only other significant variation between grid levels. On the negative z/H side of the bump, the changes between successive grid levels are smaller than on the positive z/H side of the bump between the Level 2 and Level 1 results. The changes in the $C_{p,ref}$ asymmetry will be evaluated later to quantify the grid level effects on asymmetry for this case.

The surface profiles of the coefficient of pressure for the highest Reynolds number of $Re_H = 650K$ is plotted in Figure 2.10 where the centerline is seen in Figure 2.10a and the centerspan is seen in Figure 2.10b. The $Re_H = 650K$ results show the largest discrepancies as the grids are refined. Looking at the centerline $C_{p,ref}$ in Figure 2.10a, it is immediately apparently that the results changed significantly between Levels 1 and 2. These changes first appear along the centerline when the $C_{p,ref}$ does not reach the peak location of $C_{p,ref}$ along the windward high curvature region while the flow is traveling up the hill. The Level 1 value is lower than that of both Levels 2 and 3, which appear collocated within the region, while aligning with the experimental data. Level 1 does not reach this peak $C_{p,ref}$ when compared to the experimentally obtained results. Interestingly enough though, the lower $C_{p,ref}$ value

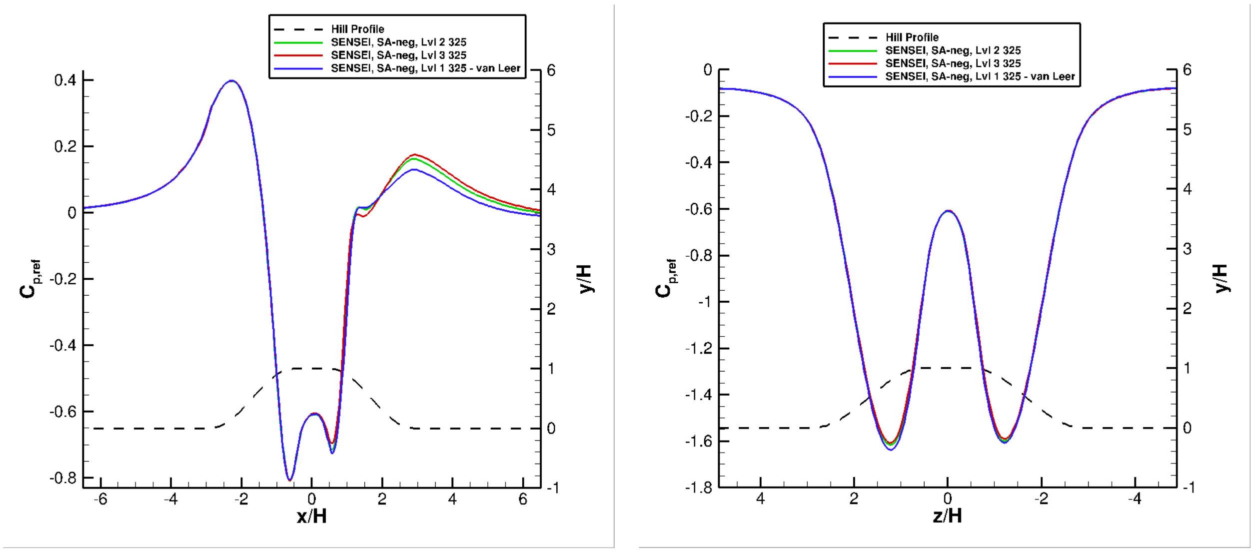

(a) Centerline

(b) Centerspan

Figure 2.9: SENSEI SA-neg centerline and centerspan $C_{p,ref}$ distributions on grid Level 1, 2, and 3 for a Reynolds number of $Re_H = 325K$.

at the peak within the FPG region does not significantly affect the results decreasing within the APG region and does so similarly to both Levels 2 and 3. The Level 1 result does produce a higher value of $C_{p,ref}$ at the beginning of the flat top region of the hill which is not seen within the Levels 2 and 3 results and is more consistent with the experimentally obtained results. This agreement with experimental data continues over the flat top region of the bump for Level 1. Levels 2 and 3 produce lower $C_{p,ref}$ values at the beginning of the flat top region and continue to remain lower than Level 1 and the experiment for the entirety of it. As the flow begins to separate, it is seen that the decrease in $C_{p,ref}$ at the end of the flat top region remains higher as the grids get more refined. Traveling into the separated region, it is seen that as the grid gets more refined, the separation locations occurs sooner. Of note, is that all three grid levels appear to agree with two of the experimental $C_{p,ref}$ data while increasing rapidly during separation. Levels 2 and 3 produce $C_{p,ref}$ values during separation that are significantly higher than both the Level 1 data and the experimental data. It, by nature, looks to be more consistent with what is seen for the lower Reynolds numbers. This is contrary to what is seen for Level 1. The Level 1 result does not recover to as high of a $C_{p,ref}$ value as Levels 2 and 3, but remains much lower. Level 1 produces a much more noticeable dip in $C_{p,ref}$ as well within the separated region which is more consistent with the experimental $C_{p,ref}$ behavior. But, the Level 1 data does not dip back down at the correct location when compared to experimental data. Furthermore, the Level 1 data only agrees with a single pressure tap value within the region around $x/H = 2$. At around $x/H = 3.5$, it is seen that the Level 1 results begin to agree with the experimental results again and does so before the Level 2 and 3 results.

Looking now at the centerspan $C_{p,ref}$ results in Figure 2.10b it is again seen that significant grid effects are occurring. Of immediate note is that the results are significantly different in a large portion of the plot. This, as discussed previous for $Re_H = 325K$ is a drastic change between grid level results. It is seen that the Level 2 and 3 results are extremely symmetric through the slice which is drastically different than what was seen experimentally. This behavior changes though within the Level 1 results which are far more asymmetric than Level 2 and 3 and more consistent with the asymmetric nature of the experimental results. Looking around where $z/H = 1.25$, it is seen that the experimental data has an extremely sharp increase in $C_{p,ref}$ over the high curvature region going to the flat top of the bump. Levels 2 and 3 are much more similar to the lower Reynolds number data in that it produces a more gradual rise in $C_{p,ref}$ up to the flat top. The Level 1 results, although more skewed than the Level 2 and 3 results do not see as sharp of a rise in Cp. It also does not predict the minimum $C_{p,ref}$ to be as low as the experimental data or both Level 2 and 3. Within the flat top region of the bump, all three grid levels predict the rise in $C_{p,ref}$ fairly well. The significant differences occur in the value of the local maximum of $C_{p,ref}$ at around $z/H = 0$. It is seen that the Level 1 results match the peak $C_{p,ref}$ values from the experiment better than both Levels 2 and 3. Level 1 continues to match the experimental data well within the negative z/H region of the plot on the flat top region which is not seen with Levels 2 and 3. Within the negative z/H region, the asymmetric nature of the experimental data is visible. It is seen that on one side of the bump, the $C_{p,ref}$ values at the local minimum are significantly higher than the other. The Level 2 and 3 results do not support this as they are both extremely symmetric across the centerspan. The Level 1 results, predict the experimental data well, and are far more consistent with what is expected based on the experimental results. It is seen within Figure 2.10 that there are significant grid effects that are not seen at the lower Reynolds numbers. This implies that even at Level 2, the grid is not refined enough for the highest Reynolds number. With the Level 1 grid being extremely resolved, the asymmetric effects can be solved for within SENSEI and the results are more consistent with the behavior and data seen experimentally.

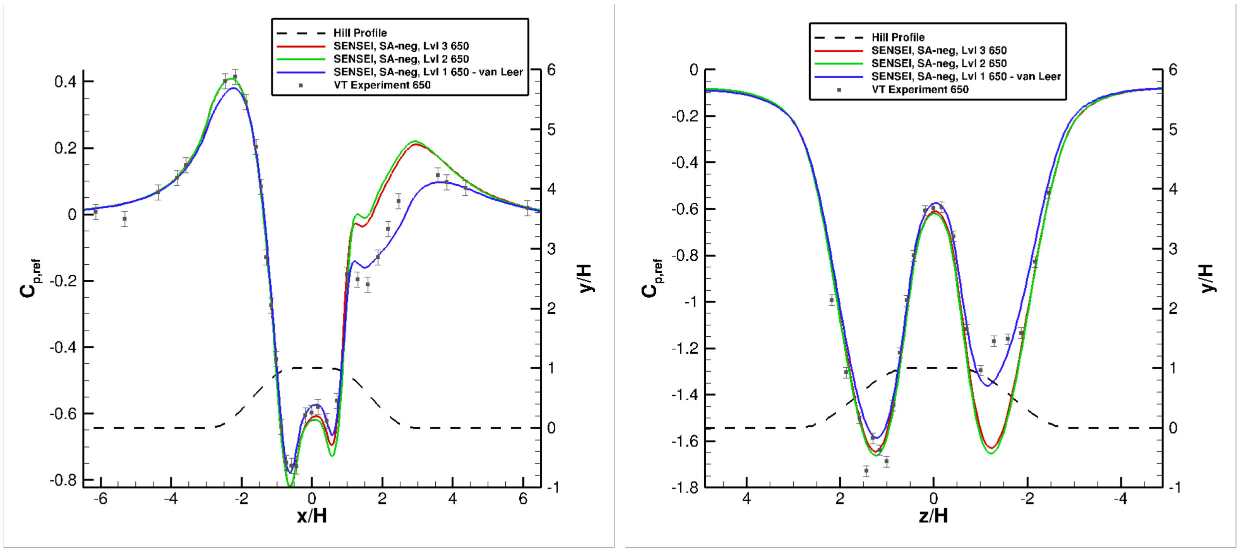

(a) Centerline

(b) Centerspan

Figure 2.10: SENSEI SA-neg centerline and centerspan $C_{p,ref}$ distributions on grid Level 1, 2, and 3 for a Reynolds number of $Re_H = 650K$.

CenterSpan Asymmetry

In order to quantify the asymmetry within the results along the centerline, the data from each case was plotted such that the lowest $C_{p,ref}$ dip within the CFD data were all on the same side. By taking advantage of the spanwise symmetry of the grids, a data point from one side of the domain was subtracted from its collocated point on the opposite side of the domain. By doing so, the asymmetry of the result could be quantified about the centerline for the centerspan data as ΔCp which represents the difference in $C_{p,ref}$ between these points. This analysis is presented for all three Reynolds numbers for each grid level. Unexpected jumps and sharp deviations are present within the plots. These jumps mainly represent an extremely small deviation between the oppositely located points and are not of concern for this analysis.

Looking at a Reynolds number of $Re_H = 250K$ first, while keeping in mind the uncertainty in the convergence of the Level 1 results, the ΔCp values for Levels 1, 2, and 3 are shown in Figure 2.11. It is seen that the Level 1 results are the most symmetric grid level result but it must be kept in mind that there is uncertainty in the overall convergence of the results. The Level 2 results, as previously discussed, are to be taken as the best result for $Re_H = 250K$. It is seen for the Level 3 grid result that there is noticeable asymmetry located at the high curvature region between the floor and the bump. Although it is not large, it does show that the flow, near the floor, is asymmetric as it is going around the bump within this high curvature region. The size of the asymmetry increases until approximately $z/H = -1.3$ where it is seen to reach the maximum difference in $C_{p,ref}$ which corresponds to the approximate location of the local minimum of $C_{p,ref}$ shown previously. It is then seen that there exists, for Level 3, significant asymmetry again at around $z/H = -0.5$ where the flat top begins. This indicates a shift most likely in the $C_{p,ref}$ profile on each side of the centerspan about the centerline. This is further supported by the fact that right before

$z/H = 0$ (since z/H cannot have a difference) that the difference between sides is not equal to 0. For Level 2, it is seen that the region seen at the beginning of the flat top in Level 3 showing ΔCp, has flattened out. Level 2 also shows a larger ΔCp value at the regions of lowest pressure in the $C_{p,ref}$ profile than both Levels 3 and 1. The overall behavior of the Level 2 result is much smoother in nature showing that all of the asymmetries have begun to coalesce into a single asymmetry that occurs only at the region of lowest Cp. Furthermore, it is seen that the Level 2 solution, even near the wall, is lower than Level 3 indicating that the asymmetries, although small, propagate out to the wall. Looking at Level 1, the shaping of ΔCp is much more consistent with that of Level 3. The peaks and troughs occur at similar spots with Level 1 having lower values of ΔCp when compared to Level 3.

Looking now at a Reynolds number of $Re_H = 325K$, Figure 2.12 shows the value of ΔCp for Levels 1, 2, and 3. It is seen that the asymmetry around the high curvature region between the bump and the floor is seen to be present again representing the flow asymmetry around the base of the bump even at low Reynolds numbers. Looking at Level 3, it is seen that this asymmetry around the base peaks briefly before decreasing to $z/H = -1.5$ around the region of lowest pressure. It then exhibits a sharp rise in ΔCp within the middle of the high curvature region before decreasing again at the beginning of the flat top region. The value of ΔCp then reaches its lowest position for the Level 3 grid shortly after the beginning of the flat top region around $z/H = -0.5$ before rising again moving towards $z/H = 0$. Looking now at Level 2, it is seen that the results mimic the behavior of Level 3. The Level 2 results near the base of the bump do not peak as high as what is seen in Level 3 but do decrease and align with each other while approaching the region of lowest Cp. The Level 2 results produce a lower value of ΔCp when compared to Level 3 indicating more asymmetry within the region of lowest Cp. The Level 2 result then increases similarly to Level 3, but the local maximum shifts closer to the flat top region shifting slightly from approximately

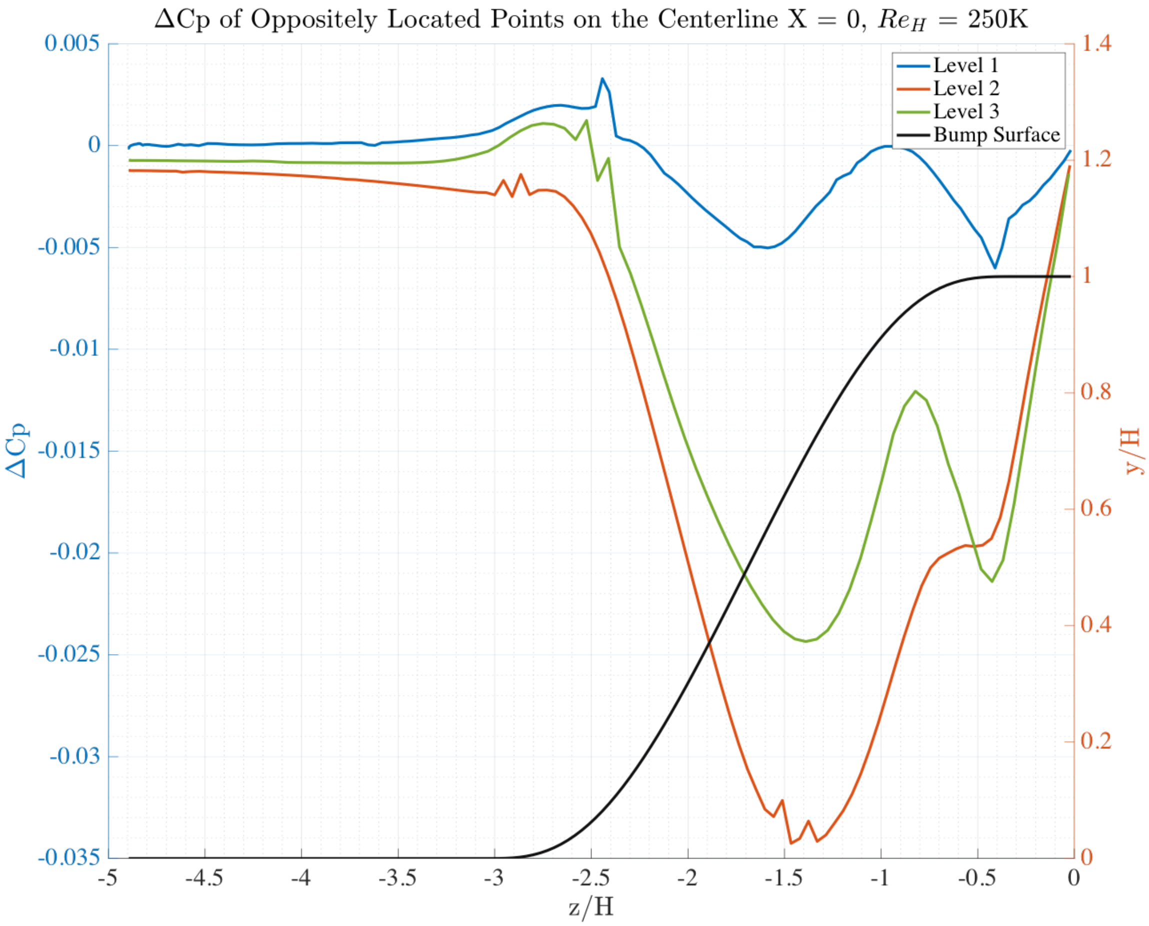

Figure 2.11: Difference in Cp (ΔCp) across the centerspan for $Re_H = 250K$ for Levels 1, 2, and 3.

$z/H = -1$ for Level 3 to $z/H = -0.75$ for Level 2. Furthermore, the changes in ΔCp are not nearly as rapid as is seen within Level 3. The Level 2 data also produces the lowest value of ΔCp at the location of minimum $C_{p,ref}$ which is not what is seen within Level 3. Level 2 then decreases again as did Level 3, to a local minimum that occurs at approximately the same location between levels, but Level 2 not produce as low as a value of ΔCp as Level 3 does. Level 2 then rises again to a similar value about the centerline as Level 3. Looking now at Level 1, the high curvature region around the base of the bump does not produce the same sort of peak that was seen in Level 2 and 3. It is a much more gradual decline in ΔCp towards the location of lowest Cp. Furthermore, as stated previously, the data was positioned such that the peak of lowest $C_{p,ref}$ was on the same side of the bump between all of the data. Looking at the high curvature region at the base of the bump, it is seen that the asymmetry along the centerspan has switched sides, as indicated by the sign of ΔCp, as the grids have gotten more refined. Looking now at the positioning of the lowest value of ΔCp for Level 1, as well as all of the levels, it is seen that it occurs around the region of lowest Cp. Additionally, there is no local maxima or minima of ΔCp as z/H trends towards 0. There is a slight dip present at the same location where Levels 2 and 3 were seen to have a dip in ΔCp, but it is not nearly the same shape or overall behavior.

This analysis indicates that for a Reynolds number of $Re_H = 325K$ as the grid becomes more refined, there is a coalescence of the peaks that are seen within the data. Between Level 3 and Level 2, there is a smoothing out of these peaks of ΔCp and rapid changes in ΔCp. As mentioned previously, there was a shift in the location of the local maxima between Level 3 and Level 2 towards $z/H = -0.5$. Then, between Level 2 and 1, there is further movement of this local maxima to the point in which the shifting local maxima has now coalesced with the stationary local minima and have smoothed out significantly. By doing so, the location of lowest ΔCp has decreased significantly and is located at the region of lowest Cp. This further supports the behavior of Level 2 and Level 3 seen within the $Re_H = 250$ ΔCp plot shown previously and allows for the verification there was a coalescence of peaks occurring when Level 1 was not considered.

Looking now at a Reynolds number of $Re_H = 650K$, Figure 2.13 shows the value of ΔCp for Levels 1, 2, and 3. Immediately it is obvious that the changes within grid levels is significant. As was previously discussed, the Level 2 and 3 grids were not able to pick up on the asymmetry seen experimentally when $Re_H = 650K$. Looking at Levels 2 and 3,

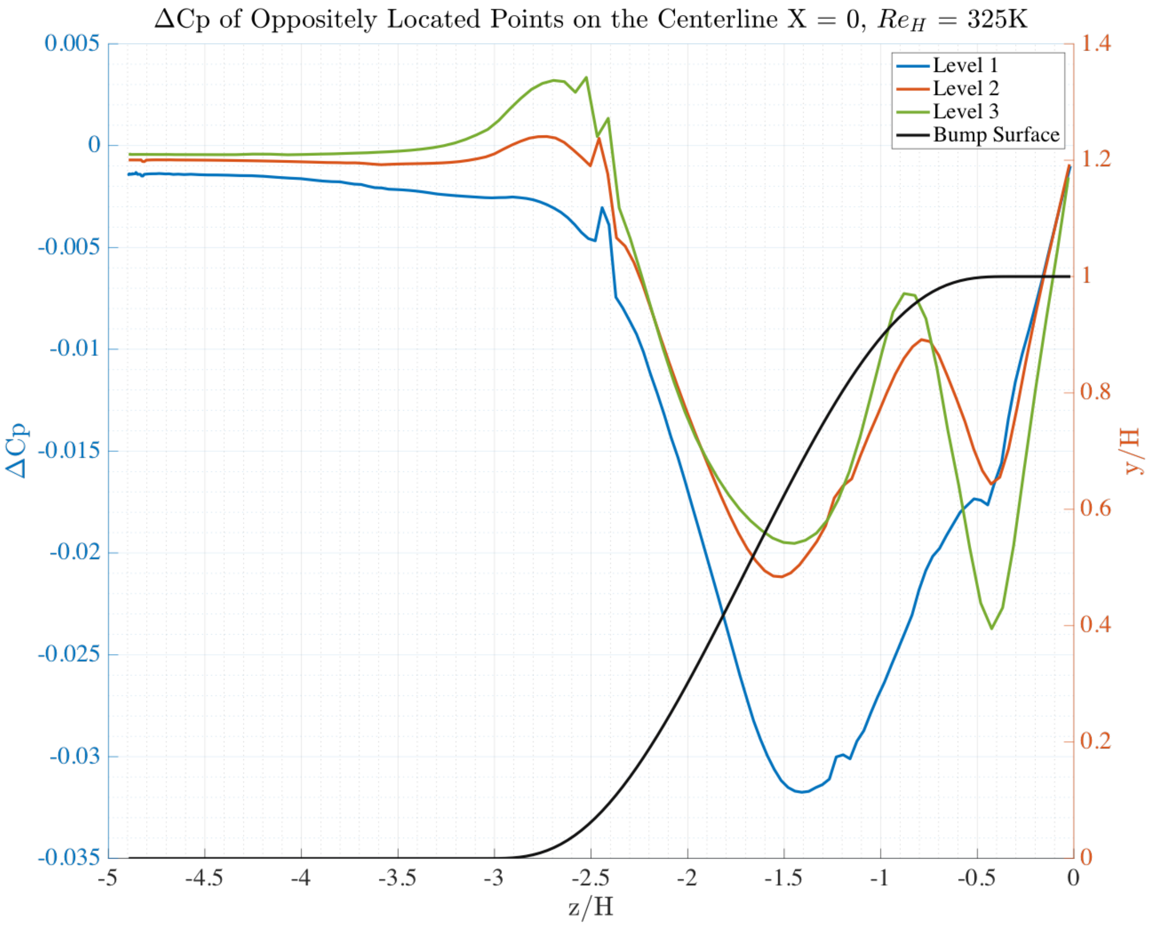

Figure 2.12: Difference in Cp (ΔCp) across the centerspan for $Re_H = 325K$ for Levels 1, 2, and 3.

it mimics the behavior seen in the lower Reynolds numbers that shows a peak around the base of the bump near the high curvature region that decreases in magnitude as the grid is refined. A decrease then occurs up to the location of lowest $C_{p,ref}$ but is more symmetric for the finer Level 2 grid than for the coarser Level 3 grid. This is then followed up by an increase in $C_{p,ref}$ and subsequent decrease in $C_{p,ref}$ while approaching $z/H = 0$. The Level 2 and 3 results by themselves show that as the grid is refined, the solution becomes more symmetric. There is no coalescence in the ΔCp value as was seen previously and further

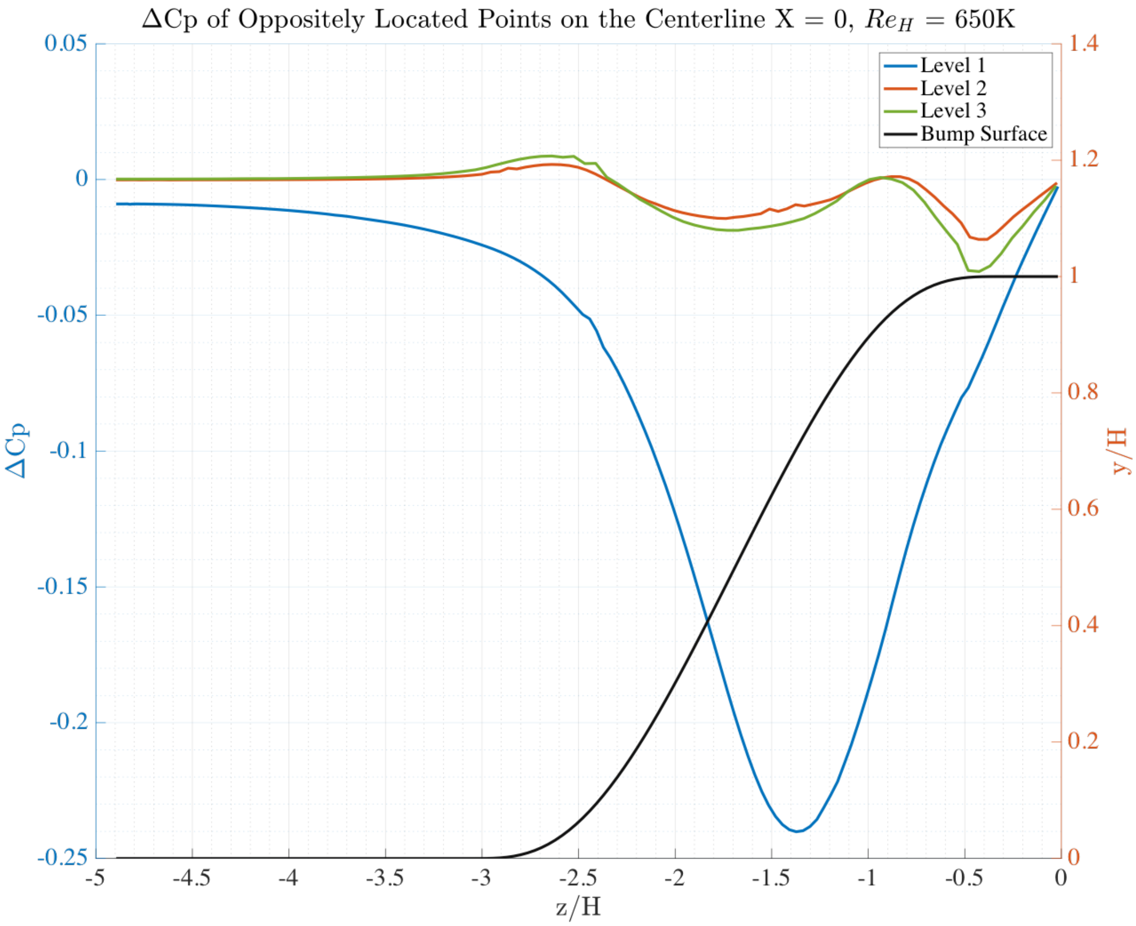

Figure 2.13: Difference in Cp (ΔCp) across the centerspan for $Re_H = 650K$ for Levels 1, 2, and 3.

highlights the issues discussed. Level 1, as was highlighted previously, does a much better job overall at predicting the experimental data than both Level 2 and 3 along the centerspan. When looking at the ΔCp plot, it is now obvious that there is a significant drop in ΔCp at the location of lowest $C_{p,ref}$ that was not seen in Levels 2 or 3. There is a slight change in the slope of the ΔCp profile at the beginning of the flat top region as was seen previously on lower Reynolds numbers. This mimics the coalescence of peaks that was seen in the other two Reynolds numbers. The Level 1 result indicates that there is a major asymmetry that is present and supports the notion that the Level 1 grid has become fine enough for SENSEI to more accurately solve for the asymmetric behavior at the higher Reynolds number.

Flow Topology

To investigate the surface flow topology. the surface was contoured with $C_{p,ref}$ values and surface shear lines for each grid level. The lowest Reynolds number of $Re_H = 250K$ is shown in Figure 2.14 with Level 3 being shown in Figure 2.14a, Level 2 being shown in Figure 2.14b, and Level 1 being shown in Figure 2.14c. Looking at each level, only Level 1 is noticeably different between grid levels. As was previously mentioned, the Level 1 result for a Reynolds number of $Re_H = 250K$ most likely has some convergence issues but was shown for completeness. Between Levels 2 and 3, the differences are minor, the surface foci for Level 2 appears to be slightly more pronounced with larger gradients within the surface shear lines being present around them. Furthermore, the Level 2 result shows slightly more skewing of the surface shear lines within the flat top region of the bump than is seen within the Level 3 results. Additionally, the Level 2 result shows stronger circulation around $z/H = 1.5$ than Level 3 does. Level 1 shows an extremely symmetric solution with little to no separation occurring within the wake. There are no surface focus present and is not consistent with what was seen experimentally or within the Level 1 and 2 results. This will represent the last discussion of the Level 1 results for the Reynolds number of $Re_H = 250K$ as there are obvious issues present.

Next, the Reynolds number of $Re_H = 325K$ is shown in Figure 2.15 with Level 3 being shown in Figure 2.15a, Level 2 being shown in Figure 2.15b, and Level 1 being shown in Figure 2.15c. Looking at the Level 3 results, we see the presence of a single focus approximately along the centerline of the surface. This focus remains in the same location as the grid becomes more refined within Level 2 and then Level 1. The end of the separation region

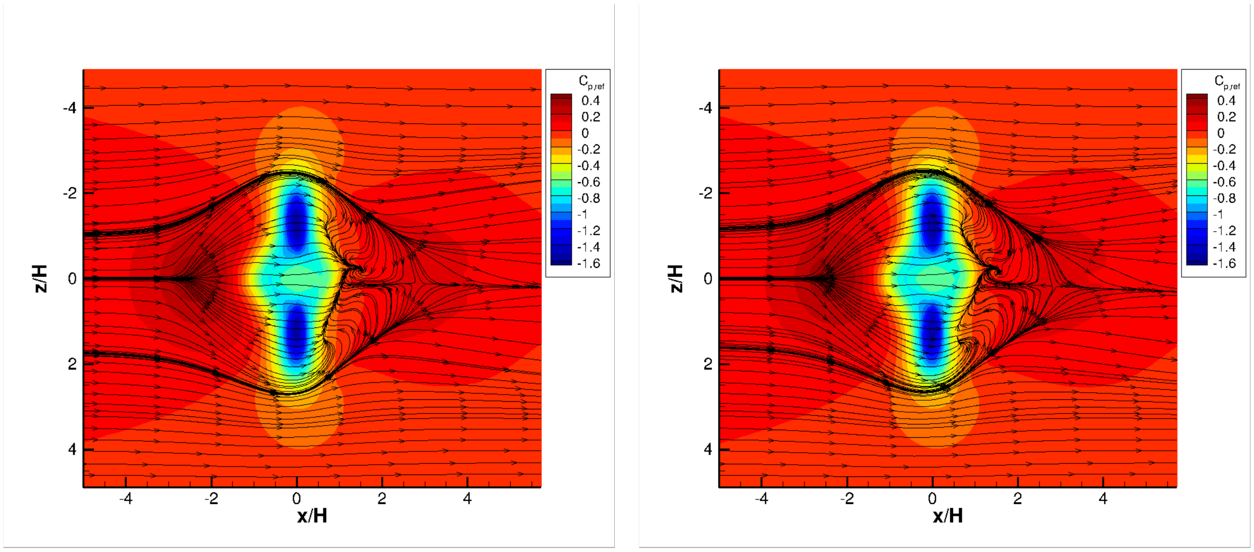

(a) Level 3 $Re_H = 250K$ (b) Level 2 $Re_H = 250K$

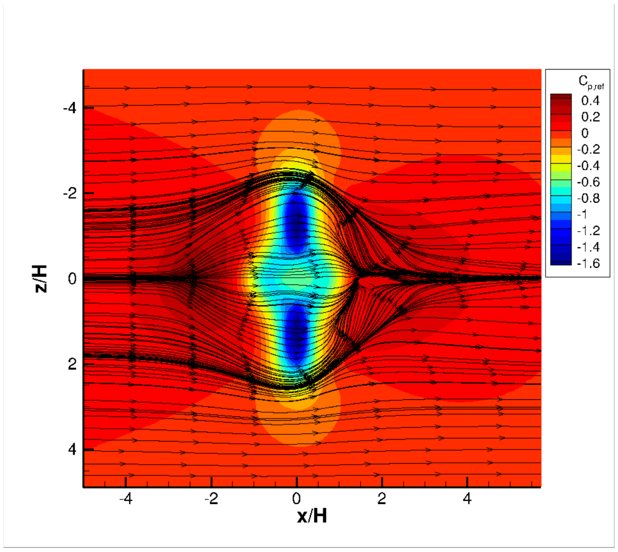

(c) Level 1 $Re_H = 250K$

Figure 2.14: SENSEI $Re_H = 250K$ surface $C_{p,ref}$ contours for Level 1, 2, and 3 with surface shear streamlines.

remains fairly constant as well with the increased grid resolution with only minor changes occurring. Again, the region that appears to change the most as the grids are refined is located at approximately $x/H = 0.5$ and $z/H = 1.5$. This region just inside of the separated region appears to get stronger as the grid is refined. This is being determined based on the gradient of the streamline within that region. As the grid levels get more refined, the gradients within that region become more reversed and switches back sooner. This change occurs while the presence of a saddle feature within the surface shear topology becomes more present with increasing grid resolution.

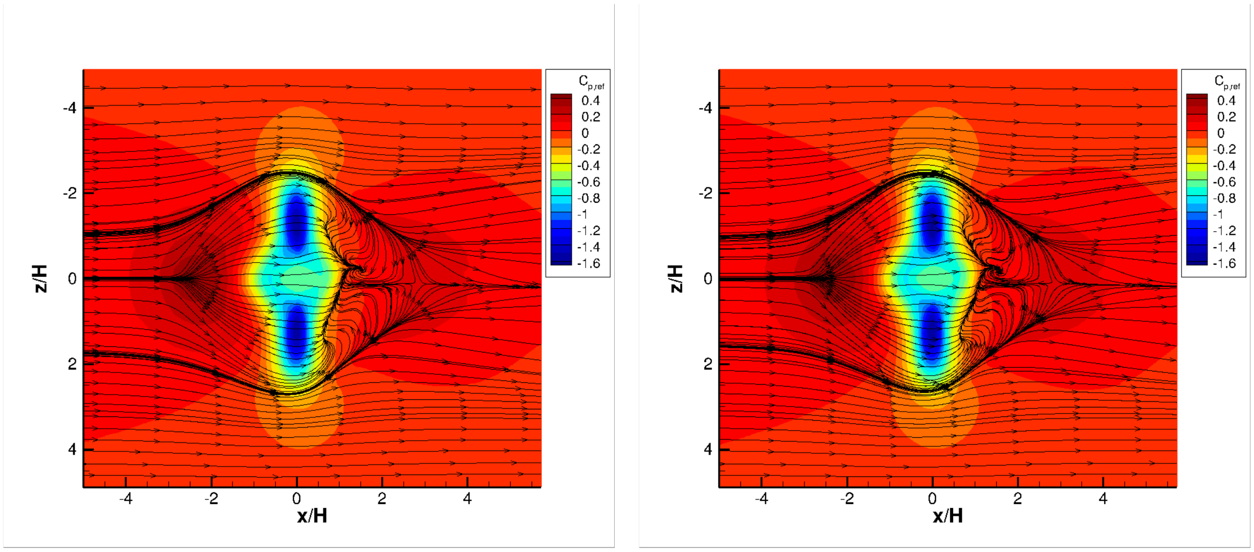

(a) Level 3 $Re_H = 325K$

(b) Level 2 $Re_H = 325K$

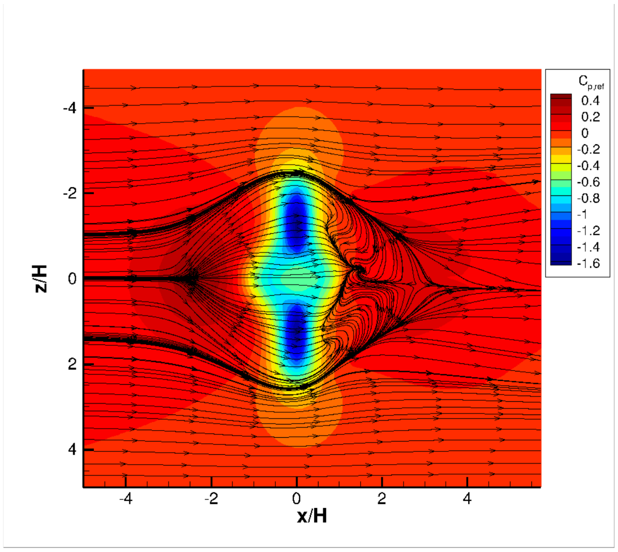

(c) Level 1 $Re_H = 325K$

Figure 2.15: SENSEI $Re_H = 325K$ surface $C_{p,ref}$ contours for Level 1, 2, and 3 with surface shear streamlines.

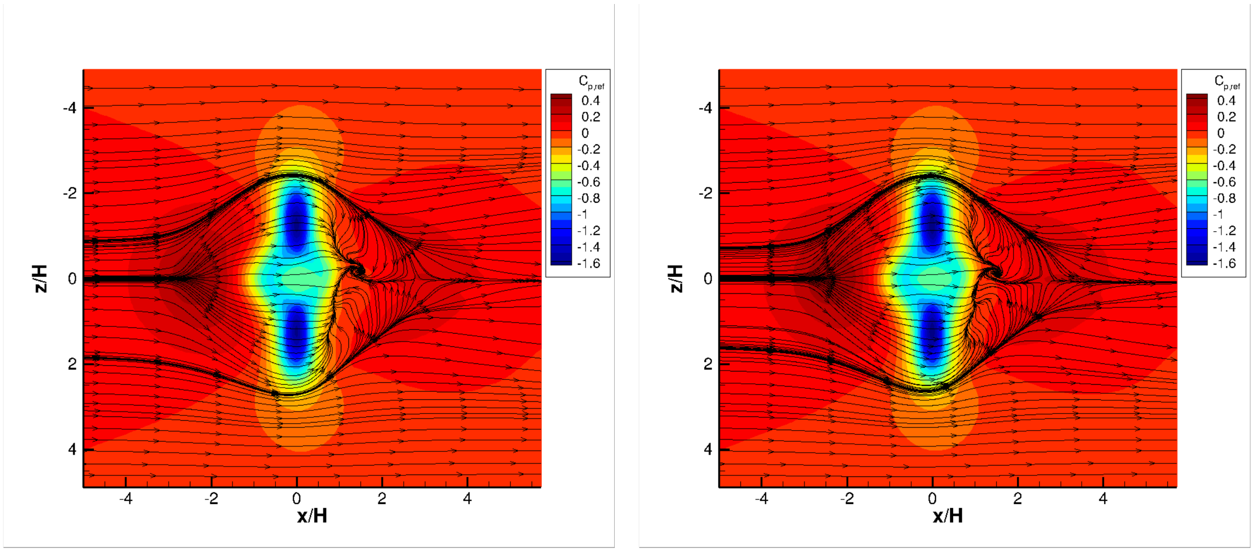

(a) Level 3 $Re_H = 650K$

(b) Level 2 $Re_H = 650K$

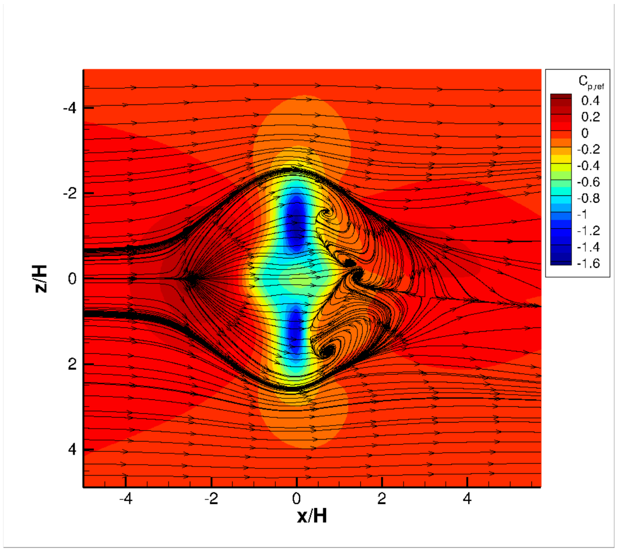

(c) Level 1 $Re_H = 650K$

Figure 2.16: SENSEI $Re_H = 650K$ surface $C_{p,ref}$ contours for Level 1, 2, and 3 with surface shear streamlines.

The highest Reynolds number of $Re_H = 650K$ is shown in Figure 2.16 with Level 3 being shown in Figure 2.16a, Level 2 being shown in Figure 2.16b, and Level 1 being shown in Figure 2.16c. Between Level 2 and Level 3, there are very minimal changes to the overall flow topology. This is supported by the surface slices taken previously that showed minimal changes between the two levels. The primary differences occur from the behavior in the wake changing direction slightly between the two levels due to the influence of the focus on the surface. This focus for Level 2 and Level 3 remains in the same place and does not significantly change between the two levels. The major differences occur though when looking at Level 1. It is seen that the singular focus along the centerline for Levels 2 and 3 has now split into two foci near the centerline with one being formed slightly within the opposite side of the centerline. Furthermore, it is seen that there is the formation of an additional foci that appears at $x/H = 0.5$, $z/H = 1.75$ and $x/H = 0.5$, $z/H = 1.5$. The focus at $z/H = 1.75$ appears to have more influence within its respective side of the separated region. This emergence of 4 foci instead of 1 is a significant change within grid levels not seen between any other solution. The flow topology is also more consistent with what has been seen experimentally and helps to support the changes within the $C_{p,ref}$ profiles shown previously. The addition of these foci drastically changes the shape of the separated region as well. It is seen that the Level 1 result has a larger separated region that what was seen with Level 2 and Level 3.

2.5.2 Reynolds Number Effects

Cp Profiles

In order to compare the effects that the Reynolds number has on the solution, the centerline and centerspan $C_{p,ref}$ profiles that have been used previously will be investigated. Shown in Figure 2.17 are the different Reynolds numbers being analyzed where $Re_H = 250K$ is plotted for Level 2, $Re_H = 325K$ is plotted for Level 1, and $Re_H = 650K$ is plotted for Level 1. Looking first at the centerline $C_{p,ref}$ profile shown in Figure 2.17a, it is seen that there are differences throughout the entirety of the profile. Starting on the windward side of the bump, it is seen that as the flow moves up the hill, the $Re_H = 650K$ case produces the lowest $C_{p,ref}$ values. This could be due to issues with boundary layer growth within the inflow, but will need to be considered future work. Looking at the lower Reynolds numbers, it is seen that they are both similar to the $Re_H = 325K$ case while being slightly higher than the $Re_H = 250K$ case. Moving along the bump to the flat top region, it is seen that the highest Reynolds number case produces a larger $C_{p,ref}$ value over the flat top of the bump than the two lower Reynolds number cases. The $Re_H = 250K$ case and the $Re_H = 325K$ case are extremely similar over the flat top region of the bump with the $Re_H = 325K$ case producing a slightly lower value of $C_{p,ref}$ before separation. Moving into the separated region of the flow, it is seen that the $Re_H = 325K$ case produces a larger value of $C_{p,ref}$ than the $Re_H = 250K$ case within the separated region of the flow with the difference between them shrinking as they get closer to the reattachment location. The $Re_H = 650K$ case produces a significantly lower value of $C_{p,ref}$ than both lower Reynolds number cases within the separated region. It is not until around $x/H = 3.5$ that the $Re_H = 650K$ case begins to predict a higher $C_{p,ref}$ value than the lower Reynolds number cases.

Looking now at the centerspan profiles within Figure 2.17b, it is seen that there are significant differences present between the lower and higher Reynolds number cases. Looking at the $Re_H = 650K$ condition, it is seen that it produces the highest $C_{p,ref}$ value around the region of lowest pressure at approximately $z/H = 1.25$. The data does align with the other two Reynolds number fairly close as the $C_{p,ref}$ decreases and increases to and from this location. Again, around the centerline, it is seen that the $Re_H = 650K$ condition produces higher $C_{p,ref}$ values than the two lower Reynolds numbers. Moving into the negative z/H side of the plot, it is seen that the $Re_H = 650K$ condition is significantly more asymmetric than the lower two Reynolds numbers, producing values of $C_{p,ref}$ that are noticeably higher than that of the two other Reynolds numbers. Looking now at the lower Reynolds number conditions, it is seen that at the location of lowest $C_{p,ref}$ around $z/H = 1.25$, that the $Re_H = 325K$ condition predicts a lower value of $C_{p,ref}$ then the $Re_H = 250K$ condition. Around the centerline, it is seen again that the $Re_H = 325K$ condition is ever so slightly lower than the $Re_H = 250K$ condition and remains lower until the flat top of the bump enters the high curvature region. Once the profiles reach the high curvature region at the top of the bump, within the negative z/H side of the bump, the $Re_H = 325K$ profiles slowly increases the difference in $C_{p,ref}$ compared to the $Re_H = 250K$ condition. Looking at the region of lowest pressure on the negative z/H side of the bump, it is seen that the difference between the solutions is slightly skewed away from the centerline with the differences between the two solutions decreasing slower within the increasing $C_{p,ref}$ portion than during the decreasing $C_{p,ref}$ portion. After the solutions converge around the beginning of the high curvature region near the base of the bump, they remain overlapped through the end of the profile.

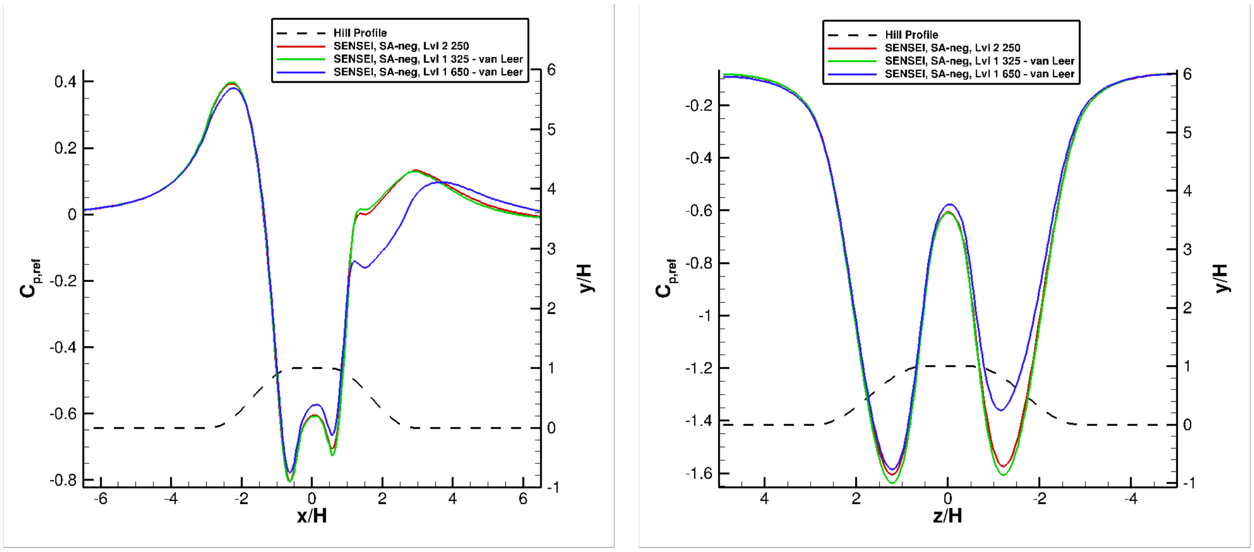

(a) Centerline

(b) Centerspan

Figure 2.17: Reynolds number effects on the Level 2 grid using the SA-neg turbulence model.

Looking now at the differences in Reynolds number for the Menter $k - \omega$ SST (2003) turbulence model, the three baseline Reynolds numbers of $Re_H = 250K$, $Re_H = 325K$, and

$Re_H = 650K$ are shown on the Level 2 grid in Figure 2.18. Looking first at the centerline data shown in Figure 2.18a, it is seen that as the flow moves up the windward side of the bump that the $Re_H = 650K$ condition produces a higher value of $C_{p,ref}$; with the value of $C_{p,ref}$ within the region decreasing as Reynolds number decreases. After the initial high curvature region around the base of the bump, it is seen that all three Reynolds number decrease in $C_{p,ref}$ at a negligible difference until the beginning of the flat top region of the bump. Once the flow reaches the flat top of the bump, it is seen that the trend switches such that the increase in Reynolds number produces a lower $C_{p,ref}$ value for the entirety of the flat top region of the bump. Once the flow separates on the hill, the increase in Reynolds number forces separation to occur sooner, with a more drastic increase in $C_{p,ref}$ occurring. Within the separated region, it is seen that the lowest Reynolds number of $Re_H = 250K$ is positioned slightly above the $Re_H = 325K$ condition, while still remaining below the $Re_H = 650K$ condition. This does not last for long with the $Re_H = 325K$ condition once again being positioned above the $Re_H = 250K$ condition and below the $Re_H = 650K$ condition at around $x/H = 2.5$. This behavior remains consistent after reattachment until all three Reynolds numbers converge at around $x/H = 4.5$ and remain converged through the remaining portion of the plot.

Looking now at the centerspan data shown in Figure 2.18b, similar behavior to the centerline profiles can be observed. Starting within the positive z/H region of the profile, it is seen that when the flow begins to reach the high curvature region, between the floor and the bump, that slight differences in $C_{p,ref}$ begin to emerge. As the profile moves towards the region of lowest pressure on the positive z/H side of the bump, it is seen that as Reynolds number increases, the value of $C_{p,ref}$ predicted gets lower. When the profiles reach the location of lowest $C_{p,ref}$ around $z/H = 1.25$ it is seen that the $Re_H = 650K$ profile is significantly lower than the other two Reynolds numbers. At this same location, it is observed

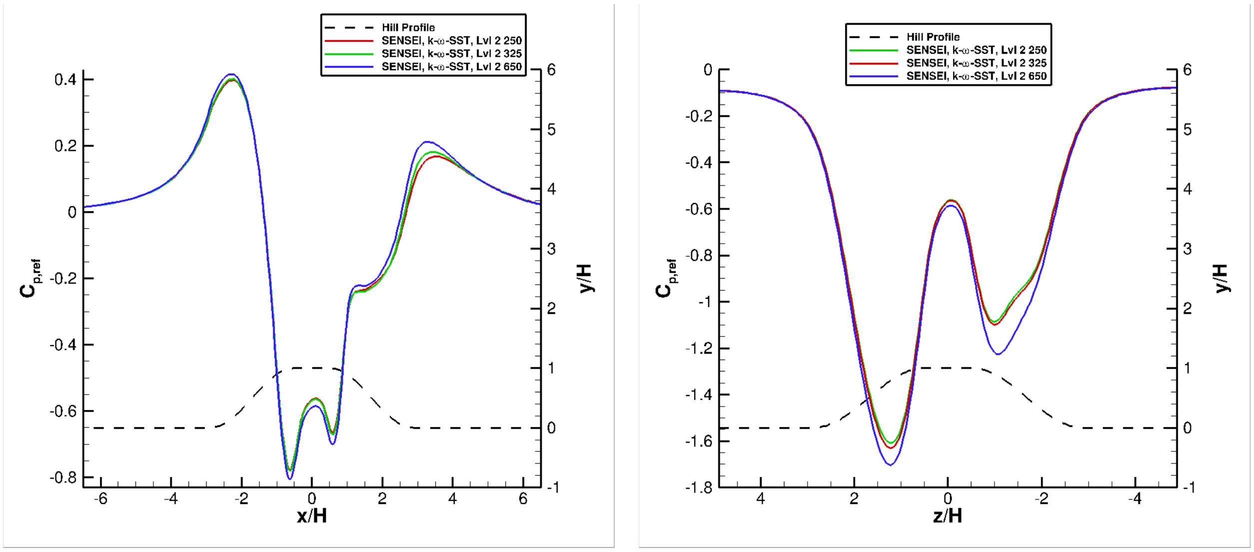

(a) Centerline

(b) Centerspan

Figure 2.18: Reynolds number effects on the Level 2 grid using the Menter $k-\omega$ SST (2003) turbulence model.

that the $Re_H = 325K$ condition predicts a lower value of $C_{p,ref}$ than the $Re_H = 250K$ condition,therefore continuing the decreasing of $C_{p,ref}$ predicted with increasing Reynolds number. Moving towards the centerline of the bump, it is seen that although the lower Reynolds number data are extremely close, that the $Re_H = 250K$ condition predicts the highest value of $C_{p,ref}$. With the $Re_H = 325K$ condition predicting a slightly lower value of $C_{p,ref}$ and the $Re_H = 650K$ condition predicting the lowest value of $C_{p,ref}$ around the centerline. This trend continues to hold true within the negative z/H region of the profile. Looking at the $Re_H = 250K$ condition and comparing it to the $Re_H = 325K$ condition, it is seen that both contain a similar shaping to each other. This is characterized by a sharp decrease in $C_{p,ref}$ from the centerline to the end of the flat top of the bump before an increase around the high curvature region, followed by a more shallow increase in $C_{p,ref}$ along the flat region on the side of the bump. Furthermore, the $Re_H = 250K$ condition produces a slightly larger value of $C_{p,ref}$ when compared to the $Re_H = 325K$ condition within this region. Looking at the $Re_H = 650K$ condition, it is evident that a lower value of $C_{p,ref}$

is still being predicted when compared to the $Re_H = 325K$ condition, but there exist a slight difference in shaping. This difference in shaping is significant because even though the lower Reynolds number data for the $k - \omega$ turbulence model on Level 2 do not predict the experimental $C_{p,ref}$ values well, the shaping is reminiscent of the $Re_H = 650K$ experimental data. But, the $Re_H = 650K$ profile has changed shape when compared to the lower Reynolds number data. It is seen that the change in the rate, at which the $C_{p,ref}$ increases, after the region of lowest pressure, on the negative z/H side of the hill, is more constant and does not change after the high curvature region as was seen with the lower Reynolds number data. This could imply that if SENSEI while running the Level 1 grid were to be able to achieve a converged solution for the $Re_H = 650K$ condition that this change in $C_{p,ref}$ increase within this region could be recovered. This would then imply that the Level 2 grid is not refined enough for the $Re_H = 650K$ data as is the case for the SA-neg turbulence model. But, without a converged solution due to issues with convergence an size, it is unlikely that this can be confirmed.

Centerspan Asymmetry

For the asymmetry analysis when looking at a Reynolds number of $Re_H = 250K$, $Re_H = 325K$, and $Re_H = 650K$, the results along the centerspan were analyzed using the Level 1 grid for $Re_H = 325K$, and $Re_H = 650K$, while Level 2 was used for $Re_H = 250K$ due to the issues with the results previously discussed. The ΔCp value along the centerspan is show in Figure 2.19 using the SA model. All of the data has been collocated as done previously to have the lowest value of $C_{p,ref}$ occurring on the same side of the centerline. Looking at the value of ΔCp for the Level 1 $Re_H = 650K$ result, it is seen that along the wall, the $C_{p,ref}$ is already asymmetric. This behavior is not seen for the other two Reynolds numbers. The $Re_H = 650K$ result also produces much lower value of ΔCp than the two lower Reynolds

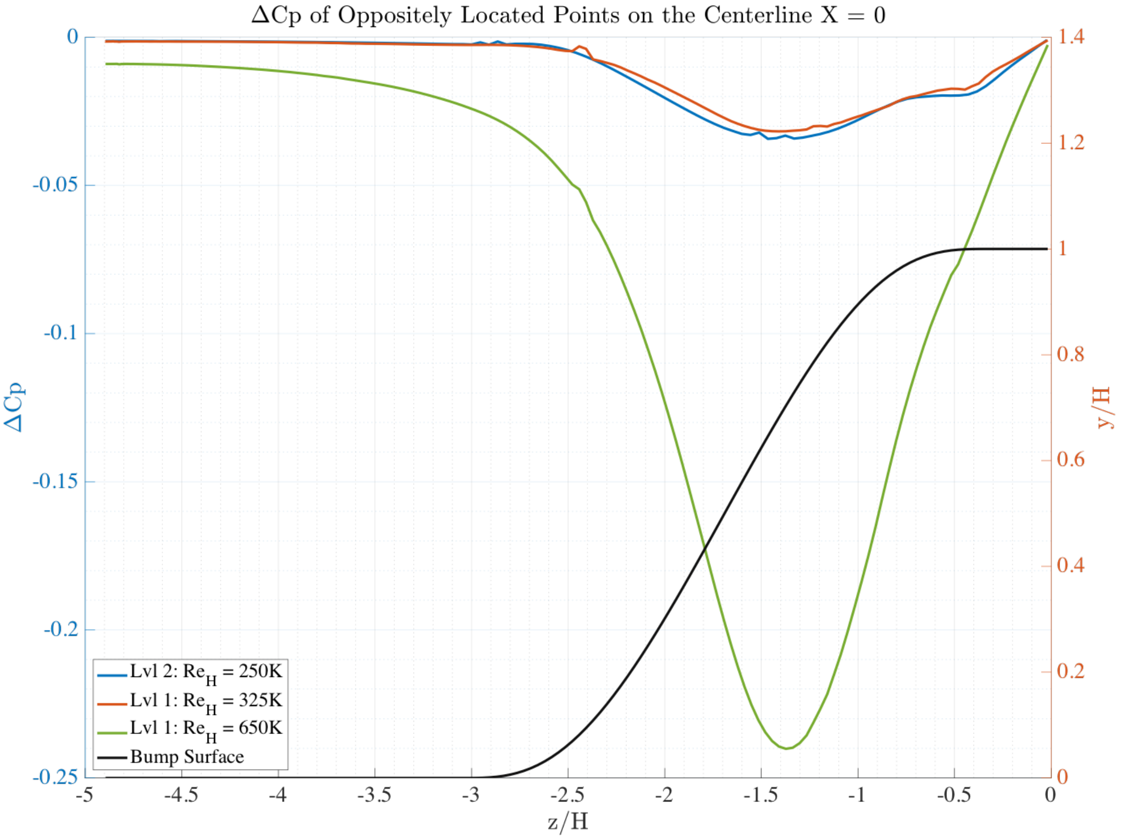

Figure 2.19: Difference in Cp (ΔCp) across the centerspan for grid Level 2 for $Re_H = 250K$ and Grid Level 1 for $Re_H = 325K$ and $Re_H = 650K$ using the SA model.

numbers. Again, it is seen that the lowest value of ΔCp for all of the solutions occurs at the locations of lowest $C_{p,ref}$ along the centerspan. It is seen that each Reynolds number also exhibits a slight flattening of the ΔCp curve as z/H moves around the high curvature region of the hill, near the flat top region. Looking at a Reynolds number of $Re_H = 250K$ and $Re_H = 325K$, it is seen that there is not a consistent trend presenting (within the data shown) that shows an increasing asymmetry with increasing Reynolds number. The $Re_H = 250K$ and $Re_H = 325K$ results show that the Reynolds number of $Re_H = 250K$ is slightly more asymmetric along the centerline than for a Reynolds number of $Re_H = 325K$. Although the results are extremely close predicting a maximum asymmetry of around $\Delta Cp = 0.035$

for $Re_H = 250K$ and $\Delta Cp = 0.030$ for $Re_H = 325K$. Nonetheless, it is seen that at the highest Reynolds number of $Re_H = 650K$ that the maximum amount of asymmetry that occurs within the solution is around $\Delta Cp = -0.24$.

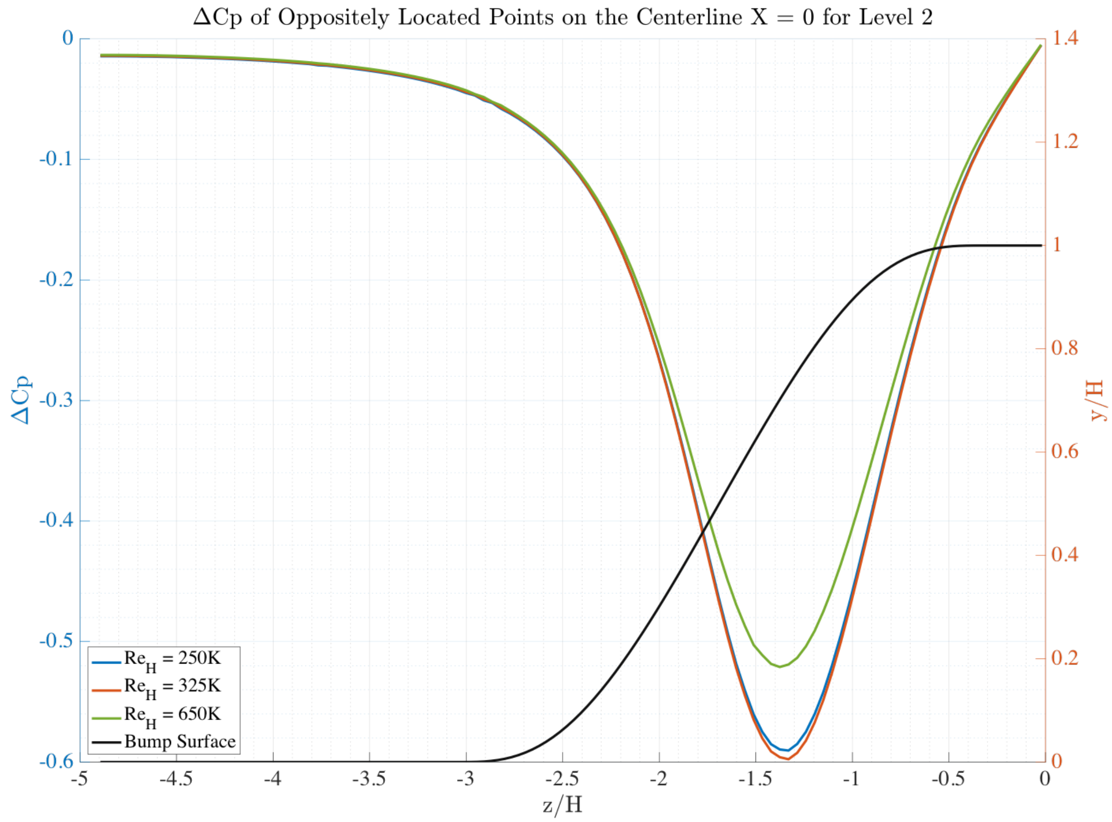

Figure 2.20: Difference in Cp (ΔCp) across the centerspan for grid Level 2 for $Re_H = 250K$, $Re_H = 325K$, and $Re_H = 650K$ using the kw model.

Looking now at the Reynolds number effects for ΔCp across the centerspan for the $k-\omega$ turbulence model, Level 2 was utilized for all Reynolds numbers and is shown in Figure 2.20. It is seen that for the $k-\omega$ results, that the highest Reynolds number of $Re_H = 650K$ is the most symmetric in magnitude and occurs at the location of minimum $C_{p,ref}$. This is alternate of what was seen for the SA model previously and is not consistent with what was seen experimentally. Furthermore, the $Re_H = 325K$ case is seen to be the least symmetric of all of the cases with the $Re_H = 250K$ case being almost as asymmetric. Furthermore, the $k - \omega$ turbulence model predicts that the magnitude of the asymmetry is larger for all three Reynolds numbers than what is seen for the SA model. From this analysis, it is clear that the $k - \omega$ turbulence model is predicting a much more asymmetric flow for all three Reynolds numbers than the SA model does, especially for the lower Reynolds number cases when using SENSEI.

Surface Topology

Looking now at the differences within the surface topology as the Reynolds number increases, surface $C_{p,ref}$ plots, with surface shear lines, will be presented for each Reynolds number and turbulence model. Looking at the SA-neg turbulence model first, Figure 2.21 shows different Reynolds numbers of interest over the surface, around the bump, where Level 2 $Re_H = 250K$ is shown on Figure 2.21a, Level 1 $Re_H = 325K$ is shown on Figure 2.21b, and Level 1 $Re_H = 650K$ is shown on Figure 2.21c. It is seen that the region of low $C_{p,ref}$for the $Re_H = 250K$ condition and the $Re_H = 325K$ condition are similar in both size and magnitude with very little differences being seen between the two for the majority of the surface shown. Looking at the Reynolds number of $Re_H = 650K$, it is seen that the region of high pressure contoured in orange has moved further away from the bump and increased in size when compared to the lower Reynolds numbers. It is also seen that the high pressure regions within the wake have changed shape for the $Re_H = 650K$ condition to be more asymmetrical when compared to lower Reynolds numbers. Looking at the surface shear lines for the low Reynolds number conditions of $Re_H = 250K$ and $Re_H = 325K$, it is seen that they are remarkably similar. The main differences between the two conditions is the amount of skewing of the streamlines around the bump with the $Re_H = 325K$ condition exhibiting more skewing than the $Re_H = 250K$ condition. Looking within the separation

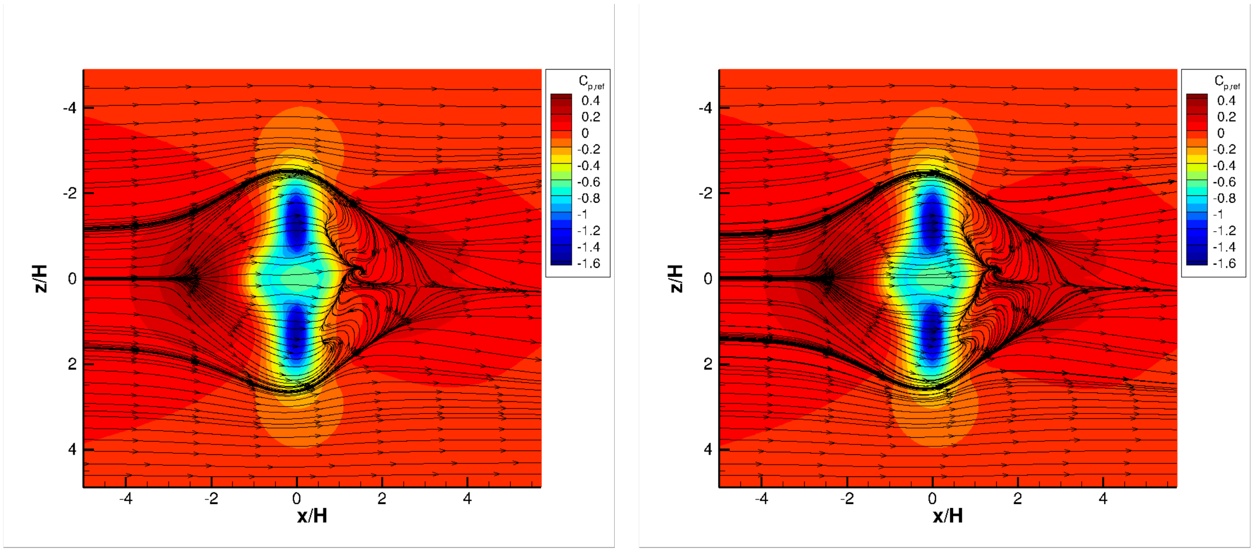

(a) Level 2 $Re_H = 250K$ (b) Level 1 $Re_H = 325K$

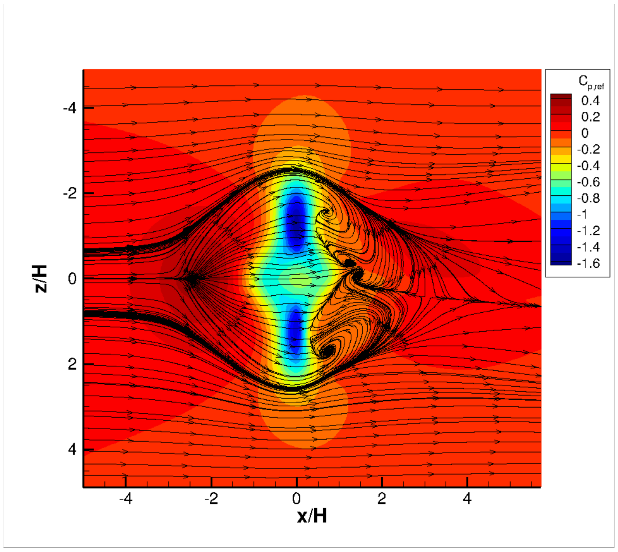

(c) Level 1 $Re_H = 650K$

Figure 2.21: SENSEI SA-neg surface $C_{p,ref}$contours with surface shear streamlines on grid Level 2 for $Re_H = 250K$ and grid Level 1 for $Re_H = 325K$ and $Re_H = 650K$.

region for the $Re_H = 250K$ condition and the $Re_H = 325K$ condition, it is seen that the $Re_H = 325K$ condition exhibits slightly stronger gradients within the reversed flow region than the $Re_H = 250K$ condition does. Both conditions predict similar separation regions and are fairly consistent in predicting the reattachment location as well. Looking at the $Re_H = 650K$ condition, it is seen that the number of foci within the wake has more than doubled when compared to the lower Reynolds numbers. The $Re_H = 650K$ condition predicts further skewing of the streamlines around the bump than the lower Reynolds number cases. Furthermore, the $Re_H = 650K$ condition predicts the separation shear line to move slightly farther up on the bump when compared to the lower Reynolds number conditions. Furthermore, the separated region within the flow for the $Re_H = 650K$ condition is pushed further away from the centerline with the saddle point within the flow becoming angled with respect to the freestream instead of parallel to it.

Looking at the Menter $k-\omega$ SST (2003) turbulence model, Figure 2.22 shows the different Reynolds numbers of interest over the surface around the bump on the Level 2 grid where $Re_H = 250K$ is shown on Figure 2.22a, $Re_H = 325K$ is shown on Figure 2.22b, and $Re_H = 650K$ is shown on Figure 2.22c. Looking at the lower Reynolds numbers of $Re_H = 250K$ and $Re_H = 325K$, it is seen that the $C_{p,ref}$contours are extremely similar over the entirety of the surface with only minor differences existing within the solution. This is consistent with what was seen within the $C_{p,ref}$profiles presented earlier. Looking at the shear lines on the surface, it is seen that both solutions contain 3 foci within the separated region of the flow. The $Re_H = 325K$ condition produces a foci on the negative z/H side of the separated region that is slightly further away from the centerline than the $Re_H = 250K$ condition is. Furthermore, within that same region, the $Re_H = 250K$ condition produces a separation line that is sightly further up the hill than the $Re_H = 325K$ condition. Outside of these features, the two conditions exhibit few differences between them. Looking at the $Re_H = 650K$ condition, it is seen that the separated region has become smaller on both sides of the bump when compared to the $Re_H = 325K$ condition. Furthermore, the focus on the surface, that had moved further away from the centerline for the $Re_H = 325K$ condition, is no longer present for the $Re_H = 650K$ condition. The region of influence of the focus along

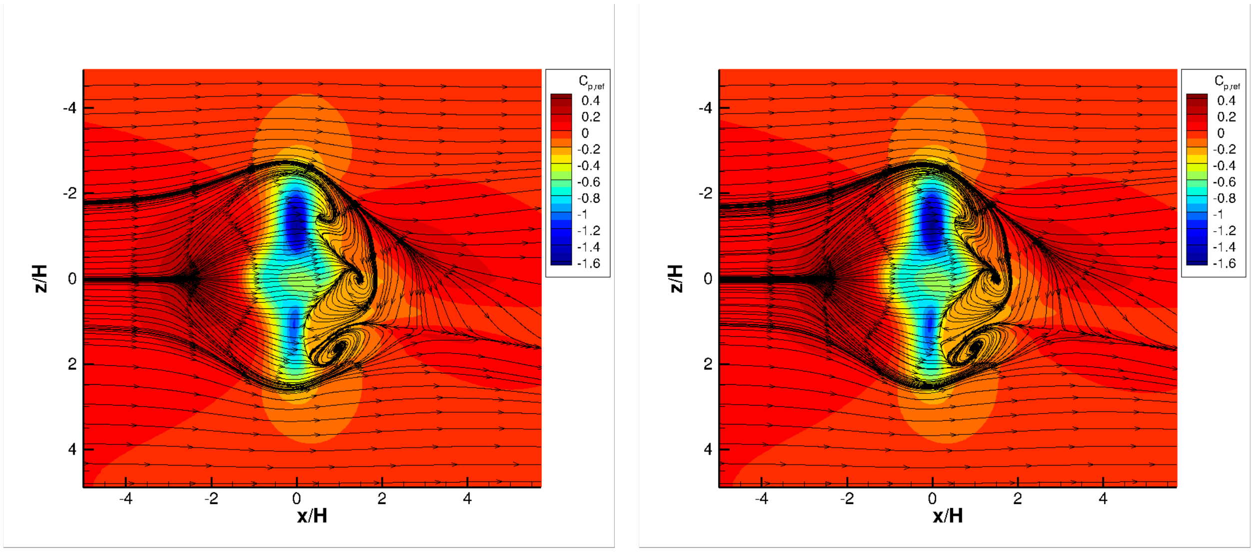

(a) Level 2 $Re_H = 250K$

(b) Level 2 $Re_H = 325K$

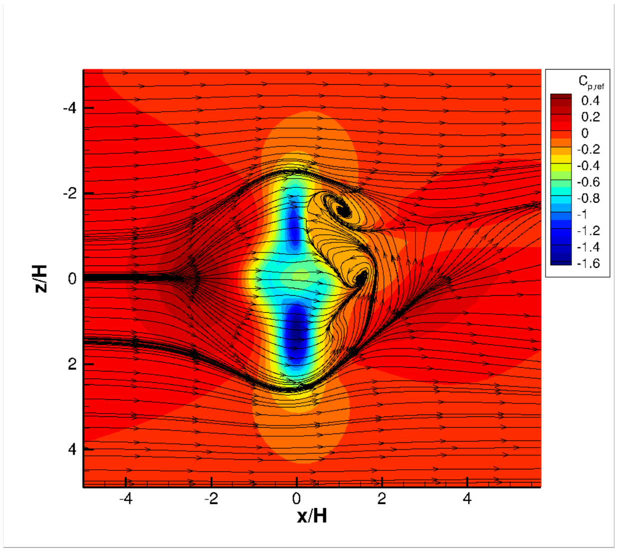

(c) Level 2 $Re_H = 650K$

Figure 2.22: SENSEI Menter $k - \omega$ SST (2003) surface $C_{p,ref}$contours with surface shear streamlines on grid Level 2 for $Re_H = 250K$, $Re_H = 325K$, and $Re_H = 650K$.

the centerline for the $Re_H = 650K$ condition has become slightly smaller than what was seen within the $Re_H = 325K$ and the $Re_H = 250K$ conditions.

2.5.3 Numerical Solver Effects

Flow Solver Comparison

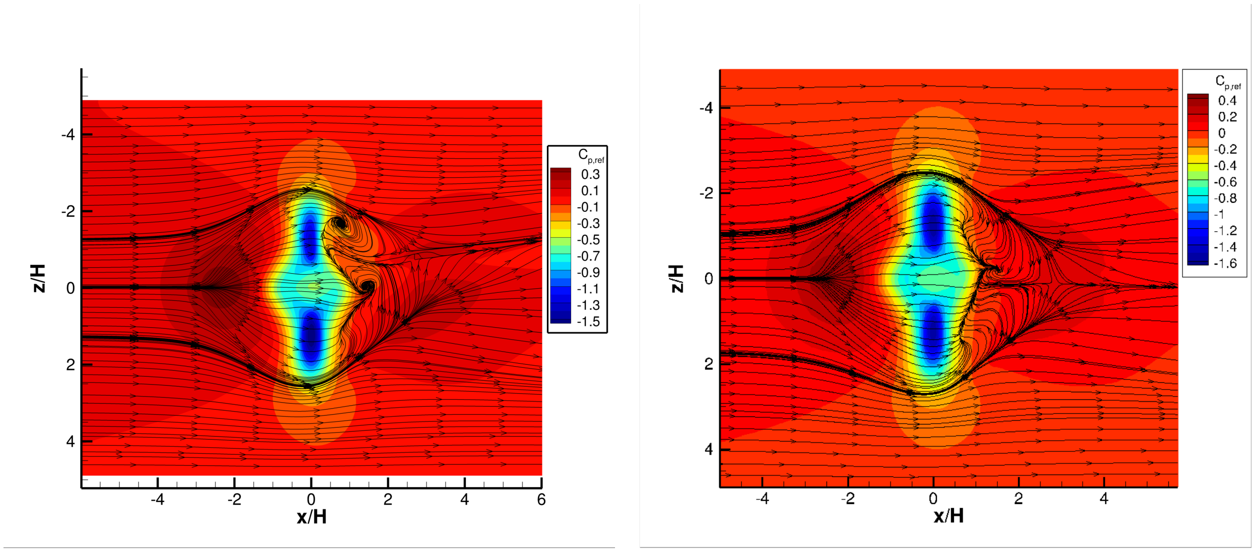

(a) Fluent (b) SENSEI

Figure 2.23: Fluent and SENSEI surface $C_{p,ref}$ distributions using the SA or SA-neg turbulence models at a Reynolds numbers of $Re_H = 250K$ with surface shear lines.

As previously discussed, the two computational solvers currently being utilized for the analysis of the BeVERLI Hill case are ANSYS Fluent and SENSEI. A comparison of the two computational solvers for a Reynolds number of $Re_H = 250K$ using the Level 3 grid is shown in Figure 2.23 where the surface is contoured by $C_{p,ref}$ and the surface shear lines are shown. The surface $C_{p,ref}$ contours with corresponding shear lines for the $Re_H = 250K$ simulation is shown for Fluent in Figure 2.23a and in Figure 2.23b for SENSEI. It is immediately obvious that significant differences in both flow topology and $C_{p,ref}$ distribution are present for the two solvers on the Level 3 mesh. Fluent predicts a much more asymmetric wake with the saddle point moving both closer to the bump in the negative x/H direction and shifting significantly in the negative z/H direction. As previously mentioned, the Level 3 SENSEI solution for $Re_H = 250K$ does not predict additional singularities within the flow but does for Level 2. Fluent though predicts a much larger focus away from the centerline that significantly changes the behavior within the entirety of the separated region. This is further compounded by the centerline focus being larger than what is seen within the SENSEI solution.

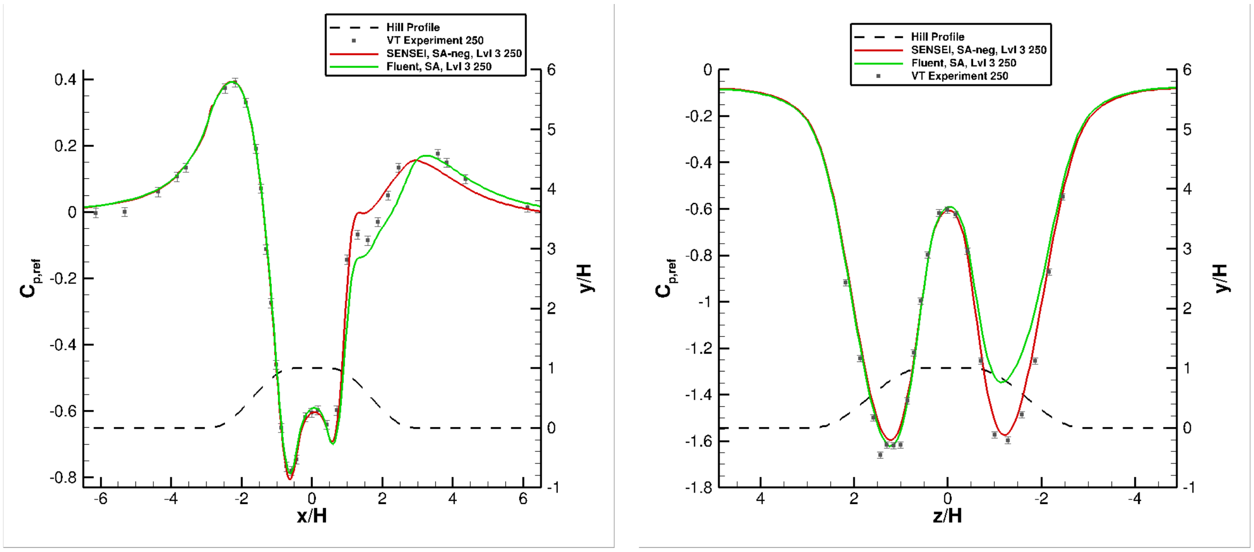

(a) Fluent (b) SENSEI

Figure 2.24: Fluent and SENSEI surface $C_{p,ref}$ distributions using the SA or SA-neg turbulence models at a Reynolds numbers of $Re_H = 250K$ with surface shear lines.

Comparing the centerline $C_{p,ref}$ between SENSEI, Fluent, and the experiment in Figure 2.24a, it is apparent that both solvers model the flow well up to approximately $x/H = 0$. Fluent tends to predict a higher $C_{p,ref}$ over the hill top than SENSEI does, but both solvers predict the experimental $C_{p,ref}$ values well up until around separation. When the flow separates, Fluent predicts that the flow will separate further downstream than SENSEI. This behavior is most likely due to the gradient limiters resisting rapid changes in the flow within Fluent where as this SENSEI computations is not using limiters and therefore does not limit large gradients. Neither solver predicts $C_{p,ref}$ well for the separated region with Fluent underestimating $C_{p,ref}$ and SENSEI overestimating $C_{p,ref}$. Fluent does predict the $C_{p,ref}$ recovery region after the separated region well, but it is not clear whether that prediction is due to the ability of the solver to properly model the behavior, or if the limiters are just allowing the solution to reach the peak $C_{p,ref}$. Fluent predicts the maximum value of $C_{p,ref}$ when $x/H > 0$ further downstream than both SENSEI solutions do. Currently, without a Level 2 solution for Fluent for $Re_H = 250K$, it is not possible to determine whether increased grid resolution will shift the Fluent results closer to the SENSEI results or further away. Additionally, it is not possible to know whether the increased grid resolution will result in Fluent better predicting $C_{p,ref}$ or if it will cause the solutions to drift away from the experimental values.

Comparing the centerspan $C_{p,ref}$ between SENSEI, Fluent, and the experiment in Figure 2.24b for a Reynolds number of $Re_H = 250K$, it is seen that Fluent drastically over-predicts both SENSEI and the experimental values roughly between $-2.0 < z/H < -0.5$. This can be attributed to the upstream effect that the foci are having on the $C_{p,ref}$ prediction and is more evident for the Fluent solution. This significant over-prediction of the experimental $C_{p,ref}$ values is due to the strength and region of influence the large focus Fluent predicts is having on the centerspan $C_{p,ref}$ upstream. This shows that this prediction of a large focus does not just effect the positioning of the saddle and centerline focus in the wake but propagates upstream. The weaker focus that SENSEI predicts does not drastically change $C_{p,ref}$ upstream and allows for SENSEI to better predict the experimental data.

The experiment shows roughly symmetric $C_{p,ref}$ values across the centerspan at the lowest Reynolds number of $Re_H = 250K$. This behavior is captured well by SENSEI on both grid levels, while Fluent predicts a much more asymmetric solution. On the opposing side from where Fluent over-predicts $C_{p,ref}$, the solver does a better job at predicting the $C_{p,ref}$ of the local minimum on the positive z/H side of the bump than SENSEI. This improved prediction on the respective side does not span a relatively large range of z/H unlike for SENSEI on the negative z/H side of the bump. Additionally, the experimental tap quality for the static pressure port located at roughly $z/H = 1.45$ may have some issues, see [21]. The over-prediction of $C_{p,ref}$ along $z/H = 0$ is again seen for Fluent with the peak slightly favoring the negative z/H side of the centerline, but the results are still within the quoted experimental error. This slight shift in the local maximum for $C_{p,ref}$ near the centerline further illustrates the effect the gradients seen by the shear lines has on biasing the $C_{p,ref}$ distribution to one side. For the $Re_H = 250K$ case using Level 3 for SENSEI and Level 3 for Fluent with a variation of the SA turbulence model, both solvers fail to fully model the centerspan $C_{p,ref}$. This inability to accurately predict the flow behavior can be most attributed to both the influence of the high curvature region where there are large spanwise pressure gradient and the upstream effects of the singularity predictions within the wake.

Limiter Effects

The SENSEI computations have been nominally run without limiters in order to ensure confidence in the iterative convergence of the solutions and to reduce iterative errors propagating into the discretization error analysis. SENSEI and Fluent use flux limiters within the discretization for both the mean flow and turbulence equations due to the ability to differentiate between sharp wave fronts and smoothly changing wave fronts in the 2^{nd} order scheme. For the flux limiters used, only the mean flow limiter was on while the turbulent flow did not have any flux limiters active. The effect that limiters had on the flow was conducted using the Level 3 grid with the SA or SA-neg turbulence model at a Reynolds number of $Re_H = 650K$. The limiters used for the SENSEI analyses included Michalak [22], van Leer[23], van Albada 1 also referred to as ”van Albada 1982” [23].

The limiter comparisons are shown in Figure 2.25 where the $C_{p,ref}$ profile along the centerline for the different limiters is shown in Figure 2.25a and along the centerspan in Figure 2.25b. The $C_{p,ref}$ solutions along the centerline for all the cases except the SENSEI solution using michalak are able to predict the incoming $C_{p,ref}$ from $x/H = -4$ to $x/H = -1$. As $C_{p,ref}$ decreases towards the global minimum, each case over predicts the $C_{p,ref}$ values along the leeward side high curvature region in the ZPG region of the bump centerline. The cases then increase towards $x/H = 0$ and begins to behave differently in the APG before increasing quickly due to the flow separation along the centerline. The Fluent solution decreases in $C_{p,ref}$ further than the SENSEI solutions before agreeing quite well with the Michalak solution for separation location and local $C_{p,ref}$ values. The other three solutions all behave almost identically to one another until around $x/H = 1.4$ where they predict the $C_{p,ref}$ distribution within the separated region differently. Additionally, the three solutions do intersect with the experimental $C_{p,ref}$ but do not substantially decrease in pressure. Further downstream, Fluent changes concavity after separation later than the SENSEI solutions do. Within the wake, the SENSEI solution using no limiters, van Leer, and van Albada all cross each other twice while remaining in the same order.

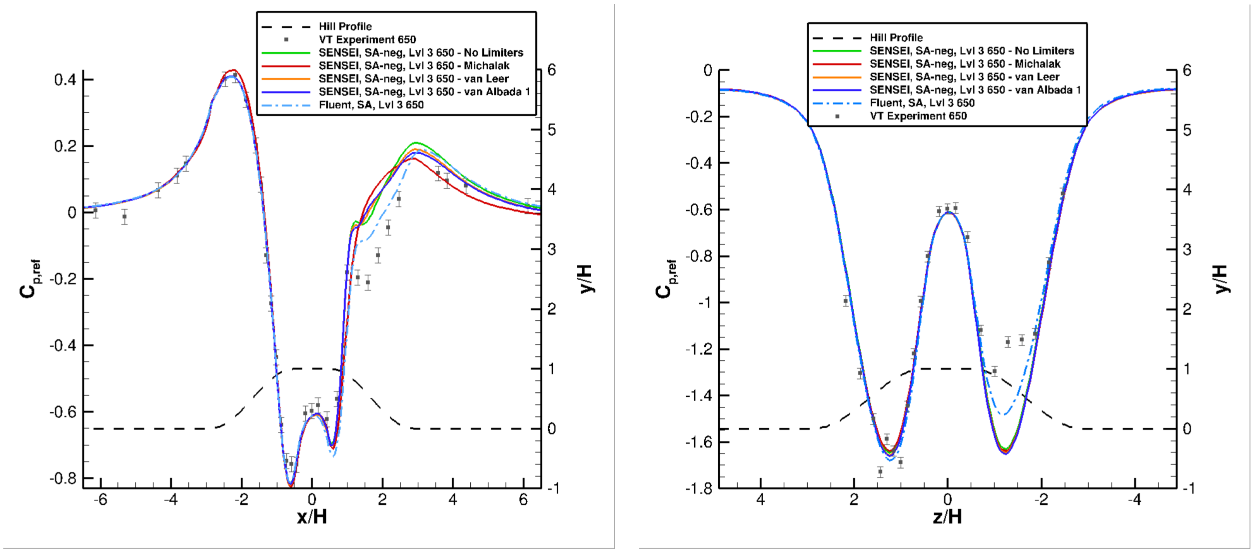

(a) Centerline

(b) Centerspan

Figure 2.25: Level 3 Fluent and SENSEI surface centerline and centerspan $C_{p,ref}$ distributions using the SA or SA-neg turbulence models at a Reynolds numbers of $Re_H = 650K$ with different limiters and limiter schemes applied.

Based upon the centerline $C_{p,ref}$ values for SENSEI with and without a limiter, the differences between solutions is extremely small for most limiters. Even though the solutions all behave different within the separated region, the behavior there is already being poorly modeled by the nominal case with no limiters but at a much higher computational cost for convergence. Additionally, the SENSEI solutions with flux limiters behave more consistently with the no limiter SENSEI case than they do with the Fluent case that is using an alternate limiter. The centerspan $C_{p,ref}$ distribution for the same cases is presented in Figure 2.25b along with the experimentally obtain values for $C_{p,ref}$. The biggest point of interest within the flow exist in that the computations poorly model the pressure distributions within the high curvature regions. Even though they model the experimental $C_{p,ref}$ poorly in certain regions, there exist a lot of consistency within the $C_{p,ref}$ predictions across both solvers and limiters. This is beneficial for future simulations when using SENSEI since the four different flux limiter methods are extremely consistent and whichever method converges the quickest and is similar to the plotted solutions is an efficient option for determining $C_{p,ref}$ distribution along the centerspan. Based on this analysis, the van Leer limiter was selected for cases with convergence issues due to the similarities in predicted $C_{p,ref}$ values and overall shaping.

2.5.4 RANS Turbulence Model Effects

As previously mentioned, the SA-neg and Menter $k-\omega$ SST (2003) turbulence models were utilized for this study. The following sections will present results for both turbulence models while investigating differences in $C_{p,ref}$ profiles along the centerline and centerspan, differences in surface topology, and differences within the flow.

Cp Profile

Starting with the $C_{p,ref}$ profiles, a comparison of the two different turbulence models for the lowest Reynolds number of $Re_H = 250K$ is shown in Figure 2.26, where the centerline $C_{p,ref}$ profile is shown in Figure 2.8a and the centerspan is shown in Figure 2.8b. Looking first at the centerline, it can be seen that both models agree quite well up until around $x/H = -0.5$ where it is seen that the SA model predicts a slightly lower $C_{p,ref}$ value, with both remaining within the experimental uncertainty. Over the flat top region of the bump, the $k-\omega$ results rise to a higher $C_{p,ref}$ value and overshoot the SA model which predicts the experimental data well. The $k-\omega$ model remains higher than the SA model up until separation. Within the separated region, the $k-\omega$ model predicts a significantly lower value of $C_{p,ref}$ than the SA model and underpredicts the $C_{p,ref}$ data obtained experimentally. After the separated region, the $k-\omega$ model predicts the maximum value of $C_{p,ref}$, which is not captured by the SA model. The SA model does overprecit the value of $C_{p,ref}$ within the separated region. This shows that neither model does a good job at predicting the experimental $C_{p,ref}$ values within the separated region of the flow.

Looking now at the centerspan profiles in Figure 2.8b, it is seen that for around half of the domain, the models agree quite well. It is seen that for the majority of the positive z/H aspect of the profile, the models are on top of each other and capture the experimental data quite well. Once the profiles reach around $z/H = 0$, the results for the $k-\omega$ model begin to diverge from the SA model. The SA model does predict the $C_{p,ref}$ values at the local maxima quite well when compared to the experimental data. The $k-\omega$ model continues to diverge away from the SA model as z/H gets more negative. The predicted $C_{p,ref}$ values continue to stray away from both the experimental data and the SA model which is predicting the experimental data well. The $k-\omega$ model begins to agree with the SA model again at around $z/H = -3$ around the base of the bump in the high curvature region.

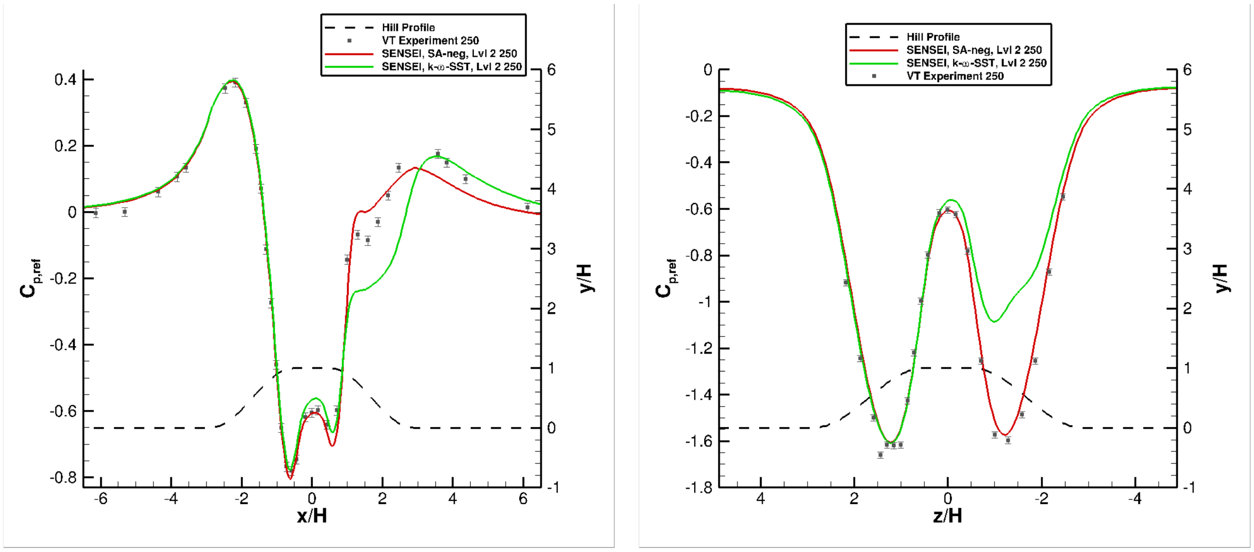

(a) Centerline

(b) Centerspan

Figure 2.26: SENSEI SA-neg and Menter $k-\omega$ SST (2003) $C_{p,ref}$ distributions using the Level 2 grid for a Reynolds number of $Re_H = 250K$.

A comparison of the two turbulence models for the Reynolds number of $Re_H = 325K$ is presented in Figure 2.27, where the centerline $C_{p,ref}$ profile is shown in Figure 2.9a and the centerspan is shown in Figure 2.9b. Starting with the centerline it can be seen that the behavior is extremely consistent with what was seen with a Reynolds number of $Re_H = 250K$. There is an agreement between the two turbulence models up until around the flat top of the bump where the $k-\omega$ model begins to predict a higher value of $C_{p,ref}$ than the SA model. Moving up to separation, they separate at almost the same location, but the $k-\omega$ model predicts a lower $C_{p,ref}$ value within the separated region than the SA model. This behavior then changes after the separated region where the $k-\omega$ model begins to predict a higher $C_{p,ref}$ than the SA model. Looking now at the centerspan data, similarities to the $Re_H = 250K$ plots shown previously can be seen. Looking at the location of lowest pressure at approximately $z/H = 1.25$, it is seen that the $k-\omega$ model predicts a slightly lower $C_{p,ref}$ value than the SA model does. Moving to the local maxima of $C_{p,ref}$ near the centerline, it is seen that the $k-\omega$ model does again predict a higher $C_{p,ref}$ value when compared to the SA model. This behavior continues until the high curvature region along the base of the bump.

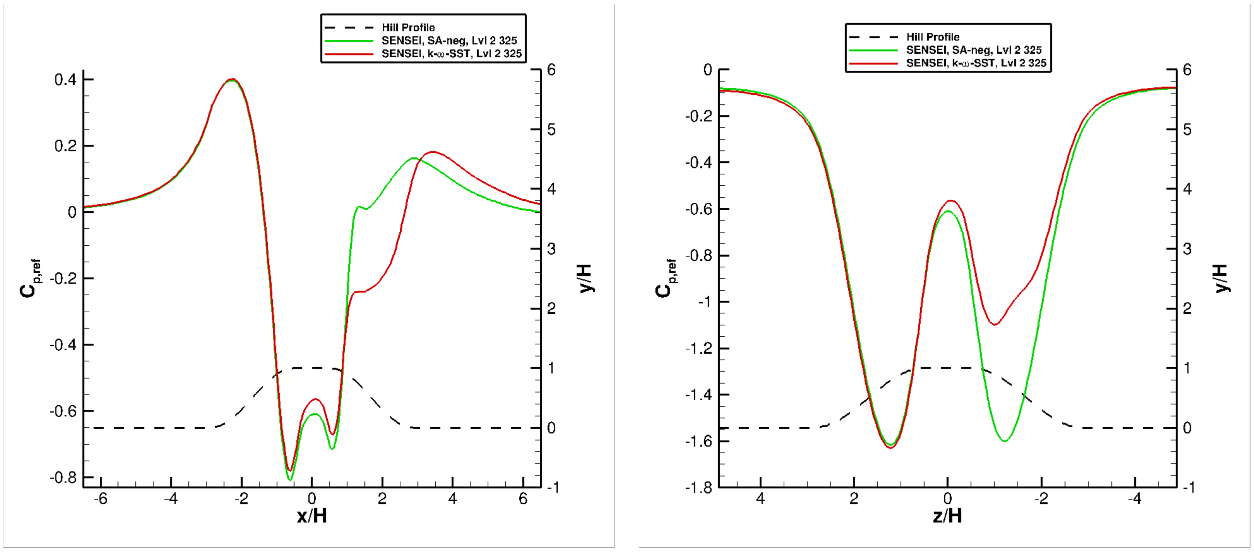

(a) Centerline

(b) Centerspan

Figure 2.27: SENSEI SA-neg and Menter $k-\omega$ SST (2003) $C_{p,ref}$ distributions using the Level 2 grid for a Reynolds number of $Re_H = 325K$.

A comparison of the two turbulence models for the Reynolds number of $Re_H = 650K$ is presented in Figure 2.28 where the centerline $C_{p,ref}$ profile is shown in Figure 2.10a and the centerspan is shown in Figure 2.10b. As discussed previously, the Level 1 result for the $Re_H = 650$ Reynolds number is significantly different than that of the Level 2 results. The following plots differ from the ones presented previously in this section since they will include the Level 1 result for SA along with the Level 2 results for both SA and $k-\omega$ for completeness. Looking first at the centerline data, it is seen that the $k-\omega$ data is collocated with the SA Level 2 results as the flow approaches the bump from the floor. All the data then becomes collocated as the flow moves up the flat portion of the windward side of the bump. At around $x/H = -0.5$ the data all predict a different value of $C_{p,ref}$ with the Level 1 SA model producing the highest $C_{p,ref}$ value, the Level 2 $k-\omega$ producing the second lowest $C_{p,ref}$ value, and the Level 2 SA result producing the lowest $C_{p,ref}$ value. The Level 1 SA model predicts the $C_{p,ref}$ values at the front of the flat top portion best when compared to the experimental data. As the flow moves over the flat top of the bump, it is seen that the Level 2 SA results again contain the lowest $C_{p,ref}$ values. Both the Level 2 $k-\omega$ and Level 1 SA model model the experimental data well along the flat top region up until separation. When the flow separates, it is seen that the Level 2 SA predicts the largest $C_{p,ref}$ values during separation. The Level 1 SA model then produces the second largest $C_{p,ref}$ values within the separated region with the Level 2 $k-\omega$ predicting the lowest $C_{p,ref}$ values. The Level 1 SA result captures a few experimental $C_{p,ref}$ port locations as does the Level 2 $k-\omega$. The Level 2 $k-\omega$ appears to model the shape of the $C_{p,ref}$ distribution the best within the wake but does not predict the $C_{p,ref}$ values at the correct x/H locations.

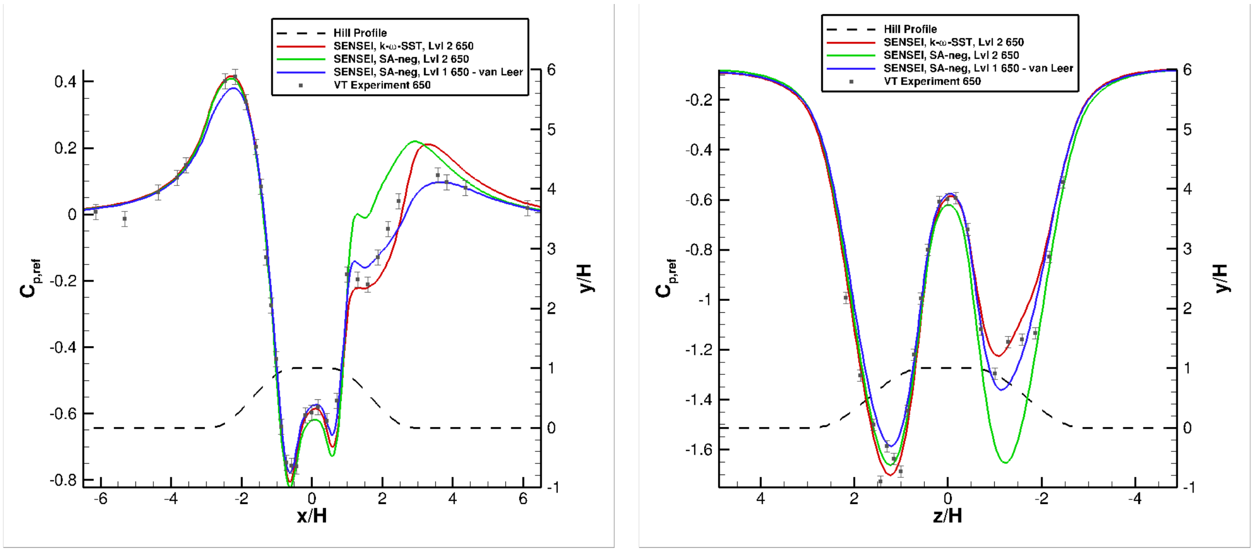

(a) Centerline

(b) Centerspan

Figure 2.28: SENSEI Level 1 SA-neg and Level 2 Menter $k-\omega$ SST (2003) $C_{p,ref}$ distributions for a Reynolds number of $Re_H = 650K$.

Looking at the centerspan data, it is seen that drastic differences between the results exist. Starting at the location of lowest $C_{p,ref}$ around $z/H = 1.25$ it is seen that the Level 2 $k-\omega$ result produces the lowest $C_{p,ref}$ value. Although the $k-\omega$ result does not produce this value of $C_{p,ref}$ at the correct z/H location compared to the experiment, it does reach approximately the same value that was seen experimentally. This was not seen within the Level 2 or Level 1 SA result at this location. Moving to the centerline around $z/H = 0$, it is seen that the Level 1 SA results and the Level 2 $k - \omega$ results behave similarly while the Level 2 result produces a consistently lower value of $C_{p,ref}$ through the rest of the domain. Looking at the Level 1 SA and Level 2 $k - \omega$ results, both models predict the $C_{p,ref}$ values near the centerline well and agree with the experimental data at this location. As z/H gets more negative, it is seen the experimental data straddles the Level 1 SA and Level 2 $k - \omega$ results with neither model out performing the other in this location where the $C_{p,ref}$ is seen to be asymmetric. The Level 2 $k - \omega$ result again seems to predict a shaping that is more consistent with what is seen experimentally. Especially when it is considered that the lower Reynolds numbers produced a flatter region that matches the experimental data shaping. This could be a result of the grid resolution for the $k - \omega$ result needing to be on the Level 1 grid as well. This result could not be obtained though due to solver issues that arose. The Level 1 SA result produces a lower $C_{p,ref}$ value than the $k - \omega$ result with neither model accurately predicting the experimental $C_{p,ref}$ value within the dip correctly.

Surface Topology

Looking at the effect of different turbulence models using SENSEI, the Menter $k - \omega$ SST (2003) is compared against the SA-neg model. Shown in Figure 2.29 the surface $C_{p,ref}$with shear lines is shown for the SA model in Figure 2.29a and the $k - \omega$ model is shown in Figure 2.29b. Looking at the $C_{p,ref}$ values, it is seen that along the centerspan, as was seen within the $C_{p,ref}$ profiles, that the $k - \omega$ result contains more asymmetry around the centerspan region of lowest pressure. It is also seen that the pressure within the wake of the $k - \omega$ result is lower than that of the SA result with the low pressure region extending further away from the bump along the wall. Looking at the shear lines, it is seen that the SA model only produces a single foci on the surface within the wake. This is not seen within the $k-\omega$ result which shows three focus within the wake. A single foci within the $k-\omega$ result is collocated with the SA model results. Additionally, regions within the SA result that have strong reversal of flow, result into foci within the $k-\omega$ result. It is seen that the shear line for the $k-\omega$ result moves closer to the top of the hill when compared to the SA model.

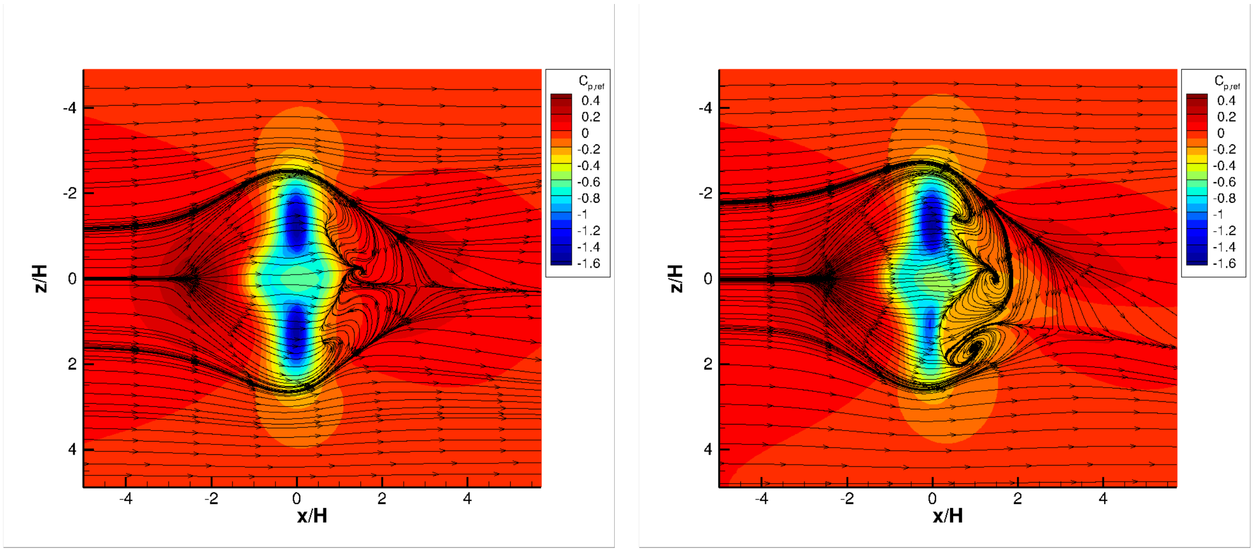

(a) SA-neg (b) Menter $k-\omega$ SST (2003)

Figure 2.29: $Re_H = 250K$ Level 2 SA-neg turbulence model and Level 2 $k-\omega$ surface $C_{p,ref}$ contours with surface shear lines shown.

With the goal of determining the strength and size of the separated region for both turbulence models, the coefficient of the x-component of shear stress on the surface was contoured such that only the reversed region of the flow is shown. Looking at a Reynolds number of $Re_H = 250K$, Figure 2.30 shows the region of separated flow, where the SA-neg turbulence model is shown in Figure 2.30a and the $k-\omega$ turbulence model is shown in Figure 2.30b. It is seen that the $k-\omega$ model produces a significantly stronger reversal of flow within the wake when compared to the SA model. Furthermore, the size of the separated region in which the $k-\omega$ model predicts a stronger reversal, even at the same magnitude, is larger than the SA model. The SA model predicts a continuous separated region with a slight inclusion into the

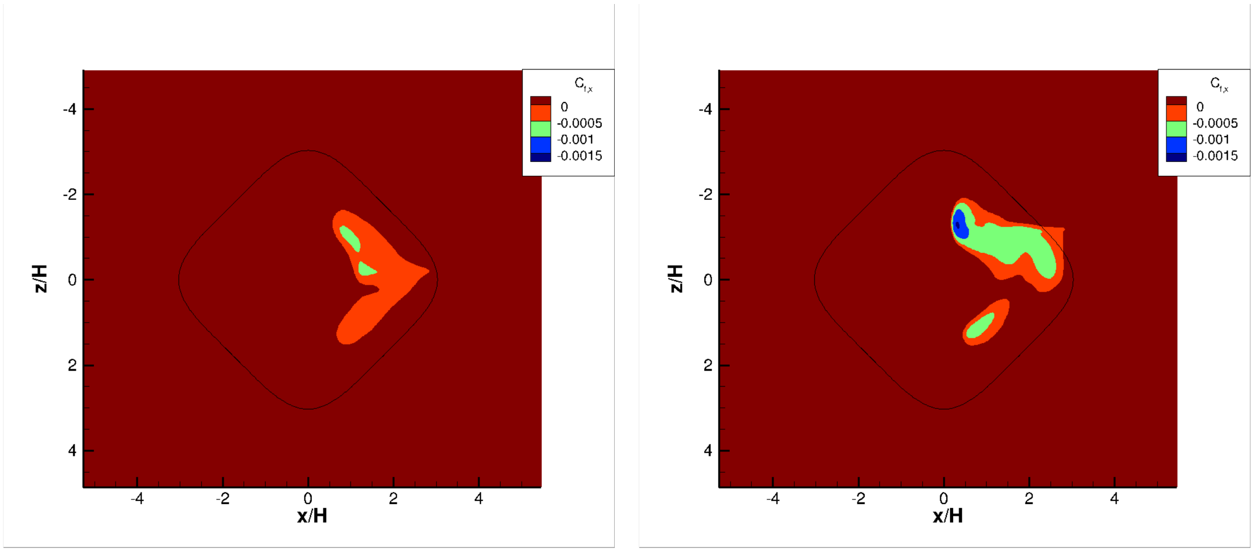

(a) SA-neg

(b) Menter $k-\omega$ SST (2003)

Figure 2.30: $Re_H = 250K$ surface $C_{f,x}$ contours with the bump outline using Level 2 grids for the SA-neg and $k-\omega$ turbulence model.

separated region due to the surface focus, while the $k-\omega$ model predicts that the separated region is split into two distinct regions with the focus being present within the gap. Looking at the location of the separated region for the $k-\omega$ and SA models, it is seen that the $k-\omega$ model predicts that the separation region will extend onto the surface of the tunnel while the SA model predicts that the separation region will be completely encompassed within the bump surface. Looking at where the models will predict that separation will occur, the $k-\omega$ model predicts separation will occur higher up on the bump and closer to the centerspan where as the SA model predicts separation further down the leeward side of the geometry. It is seen that the large focus on the surface seen in Figure 2.29b, at approximately $z/H = 1.75$, $x/H = 0.75$, is producing a stronger reversal of the flow and can be seen in Figure 2.30b to be present at $z/H = 1.75$, $x/H = -0.75$.

Increasing the Reynolds number to $Re_H = 325K$ in Figure 2.31, the surface $C_{p,ref}$ with shear lines is shown for the SA model in Figure 2.31a and the $k-\omega$ model is shown in Figure

2.31b. Looking at the $C_{p,ref}$ values, it is seen that along the centerspan, as was seen within the $C_{p,ref}$ profiles, that the $k-\omega$ result contains more asymmetry around the centerspan region of lowest pressure. It is also seen that the pressure within the wake of the $k-\omega$ result is lower than that of the SA result. This is defined by the low pressure region extending further away from the bump along the sides towards the tunnel walls. Looking at the shear lines, it is seen that the SA model only produces a single focus on the surface within the wake. This is not seen within the $k-\omega$ result which shows three focus within the wake. A single focus within the $k-\omega$ result is collocated with the SA model results. Additionally, regions within the SA result that have strong reversal of flow, present as foci within the $k-\omega$ result. It is seen that the shear line for the $k-\omega$ result moves closer to the top of the hill when compared to the SA model.

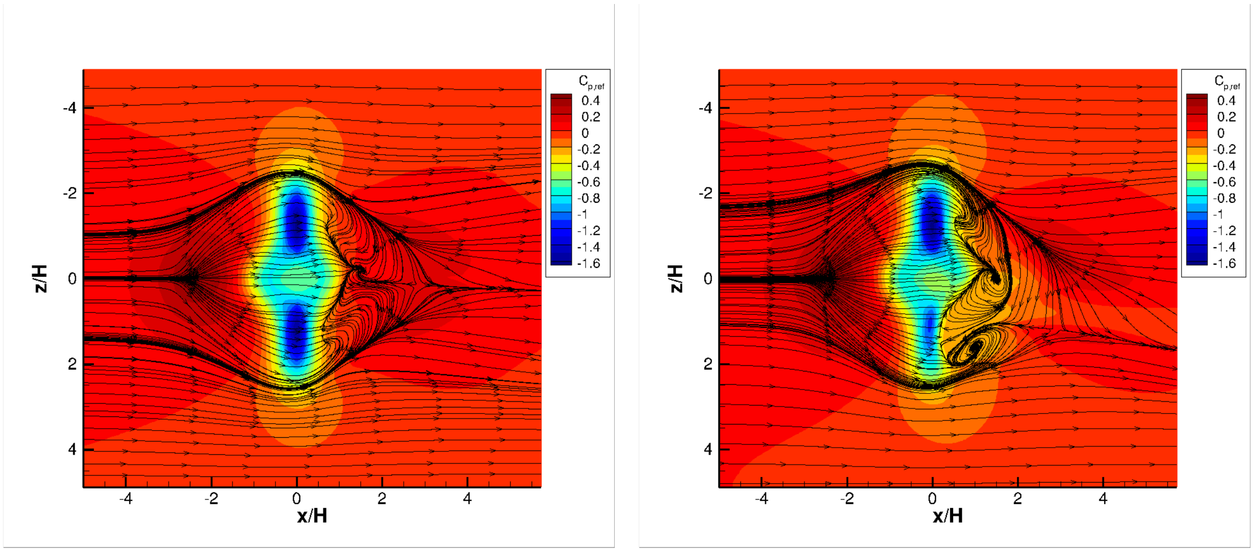

(a) SA-neg

(b) Menter $k-\omega$ SST (2003)

Figure 2.31: $Re_H = 325K$ Level 1 SA-neg turbulence model and Level 2 $k-\omega$ surface $C_{p,ref}$ contours with surface shear lines shown.

Looking at a Reynolds number of $Re_H = 325K$, Figure 2.32 shows the region of separated flow for the SA-neg turbulence model in Figure 2.32a and for the $k-\omega$ turbulence model in Figure 2.32b. It is seen that the $k-\omega$ model produces a stronger reversal of the flow within

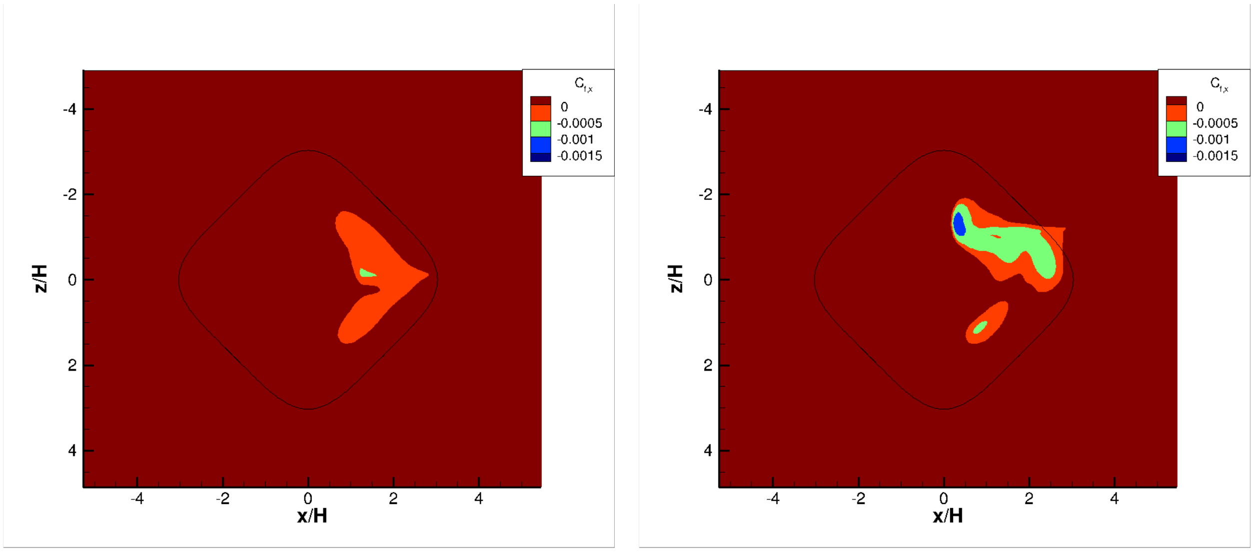

(a) SA-neg (b) Menter $k-\omega$ SST (2003)

Figure 2.32: $Re_H = 325K$ surface $C_{f,x}$ contours with the bump outline using Level 2 grids for the SA-neg and $k-\omega$ turbulence model.

the wake when compared to the SA model. Furthermore, the size of the separated region in which the $k-\omega$ model predicts a stronger reversal, even at the same magnitude, is larger than the SA model. The SA model predicts a continuous separated region with a slight inclusion into the separated region due to the surface focus while the $k-\omega$ model predicts that the separated region is split into two distinct regions with the focus being present within the gap. Looking at the location of the $k-\omega$ and SA separation regions, it is seen that the $k-\omega$ model predicts that the separation region will extend onto the tunnel wall while the SA model predicts that the separation region will be completely encompassed within the bump surface. Looking at where the models predict that separation will occur, the $k-\omega$ model predicts that the flow will separate higher up on the bump and closer to the centerspan where as the SA model predicts that separation will occur further down the leeward side of the geometry. It is seen that the large focus on the surface seen in Figure 2.31b at approximately $z/H = 1.75$, $x/H = 0.75$ is producing a significantly stronger reversal of the flow and can be seen in Figure 2.32b to be present at $z/H = 1.75$, $x/H = -0.75$.

Increasing the Reynolds number to $Re_H = 650K$ in Figure 2.33, the surface $C_{p,ref}$ with shear lines is shown for the SA model in Figure 2.33a and the $k-\omega$ model is shown in Figure 2.33b. Looking at the $C_{p,ref}$ contours, is it seen that the SA result has a larger region of low pressure around the centerspan of the bump. For the SA model, it is seen that there are four foci within the wake compared to the $k-\omega$ which only contains two foci. The SA model has two foci near the centerline while the $k-\omega$ model has predicted a single focus along the centerline, similar to what was seen for the other two Reynolds numbers. Both turbulence models predict foci behind the region of low pressure within the wake. The SA model predicts a larger separation region within the wake where as the $k-\omega$ model, when a foci is not present, predicts a smaller separated region.

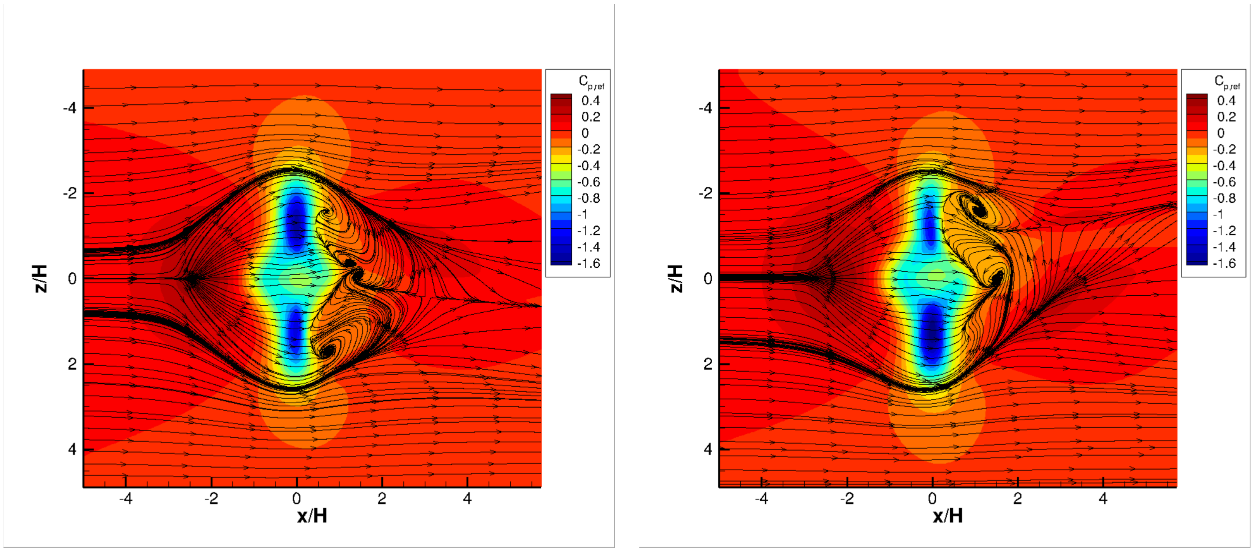

(a) SA-neg

(b) Menter $k-\omega$ SST (2003)

Figure 2.33: $Re_H = 650K$ Level 1 SA-neg turbulence model and Level 2 $k-\omega$ surface $C_{p,ref}$ contours with surface shear lines shown.

Looking at a Reynolds number of $Re_H = 650K$, Figure 2.34 shows the region of separated flow for the SA-neg turbulence model in Figure 2.34a and for the $k-\omega$ turbulence model in Figure 2.34b. It is seen that the $k-\omega$ model produces a stronger reversal of flow within the wake when compared to the SA model. Furthermore, the size of the separated region in

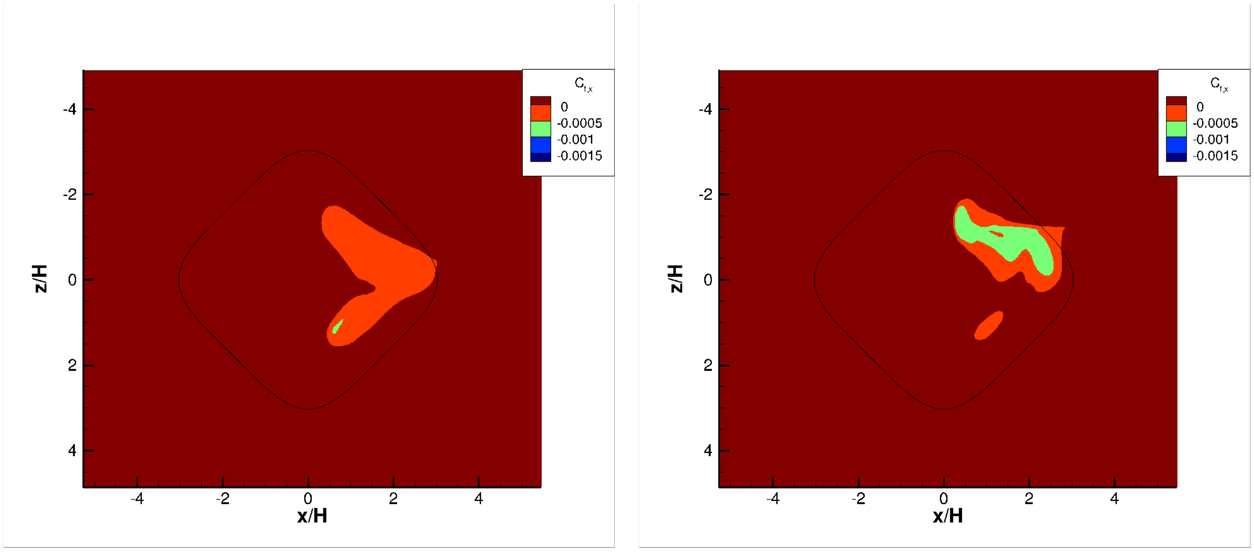

(a) SA-neg

(b) Menter $k-\omega$ SST (2003)

Figure 2.34: $Re_H = 650K$ surface $C_{f,x}$ contours with the bump outline using the Level 1 grid for the SA-neg turbulence model and Level 2 grids for the $k-\omega$ turbulence model.

which the $k-\omega$ model predicts a stronger reversal, even at the same magnitude, is larger than the SA model. The SA model predicts a continuous separated region with an inclusion, that is larger than was seen at lower Reynolds numbers, into the separated region due to the surface foci. While the $k-\omega$ model predicts that the separated region is split into two distinct regions, with the focus being present within the gap. Furthermore, it is seen that the gap produced by the $k-\omega$ result is larger than that of the lower Reynolds number conditions. Looking at the location of the $k-\omega$ and SA separation regions, it is seen that the $k-\omega$ model predicts that the separation region will extend onto the surface of the tunnel wall while the SA model predicts that the separation region will on slightly protrude off of the bump surface. The overall size of the separated region is hard to compare for the $Re_H = 650K$ condition, but it appears that the SA model will predict a slightly larger separated region than the $k-\omega$ model will. Furthermore, both models produced $C_{p,ref}$ profiles along the centerspan that straddled the experimental data on the side with higher $C_{p,ref}$ values. This is of note since for the $Re_H = 650K$ condition, the shaping of the separated region on the negative z/H side of bump is the most alike between any of the Reynolds numbers.

Flow Features

A brief discussion of the flow features for the Level 2 SA and $k-\omega$ cases is presented below along the centerline $z/H = 0$ where flow goes from left to right. Shown in Figure 2.35, U-Velocity component for the SA turbulence model result along the centerline is shown in Figure 2.35a for the SA model and is shown in Figure 2.35b for the $k-\omega$ model. It is seen that the $k-\omega$ model produces a smaller region of influence the bump has on the flow after the bump. The $k-\omega$ model predicts that freestream values of U-Velocity will be present around $x/H = 5$ while the SA model predicts a much larger region of influence and recovers free stream values around $x/H = 9$. Furthermore, the region of low velocity flow after the bump is larger for the SA model than is seen using the $k-\omega$ model. On the windward side of the bump, the U-Velocity is fairly similar between the two results with the $k-\omega$ model predicting a larger region of low U-Velocity moving up the windward face of the bump.

The V-Velocity component of velocity is shown in Figure 2.36, where the SA model is shown in Figure 2.36a and the $k-\omega$ model is shown in Figure 2.36b. Looking at the $k-\omega$ model, it is seen that the V-Velocity after the bump is far more negative than the SA model. The $k-\omega$ model predicts the flow to continue moving down the hill immediately after the bump and for this behavior to continue downstream where as the SA model predicts that the flow will be moving up the bump within this region. These differences are extremely apparent and show that the behavior within the separated region to be vastly different between the two turbulence models. The SA model is predicting that the flow will be driven up the leeward side of the hill and shed a vortex off from near the separation location. While the $k-\omega$ model predicts the opposing behavior with a separation bubble being formed on the leeward side of the bump pushing the flow down past it. Looking at the windward side of

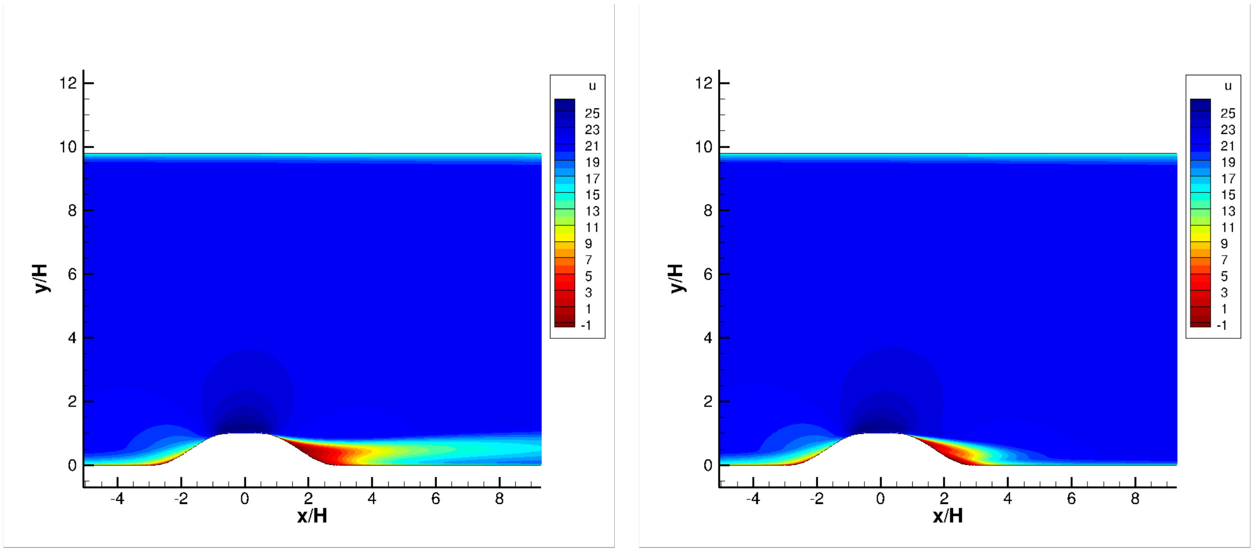

(a) U-Velocity for SA-neg

(b) U-Velocity for Menter $k-\omega$ SST (2003)

Figure 2.35: $Re_H = 250K$ Level 2 U-Velocity contours along the centerline $z/H = 0$ for the SA-neg turbulence model and the $k-\omega$ turbulence model.

the bump, it is seen that the behavior is consistent between the two models with limited differences visible between models.

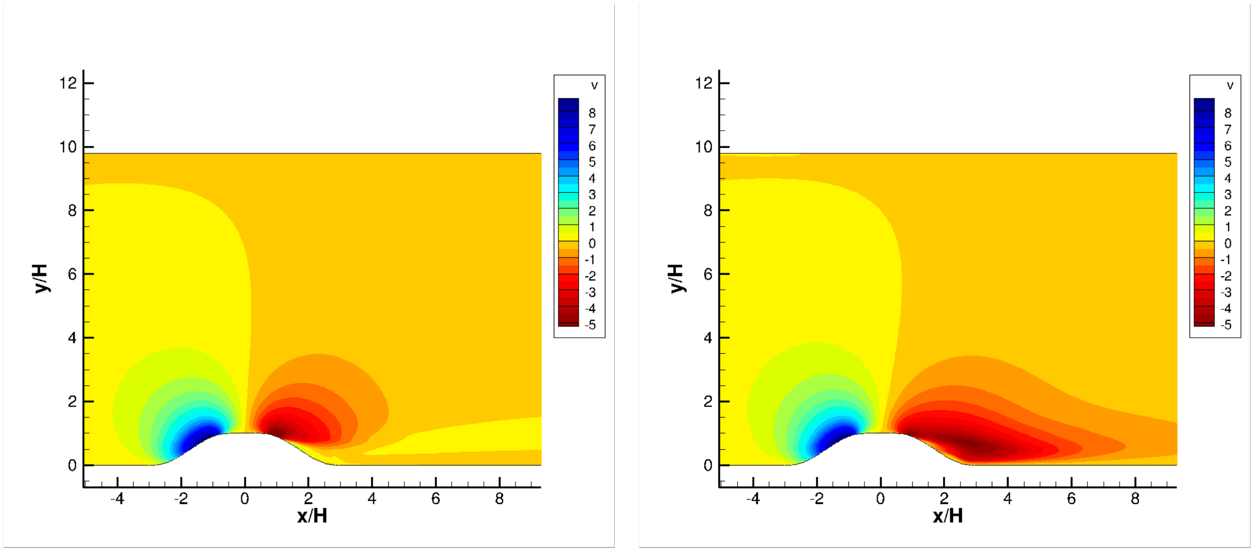

(a) V-Velocity for SA-neg

(b) V-Velocity for Menter $k-\omega$ SST (2003)

Figure 2.36: $Re_H = 250K$ Level 2 V-Velocity contours along the centerline $z/H = 0$ for the SA-neg turbulence model and the $k-\omega$ turbulence model.

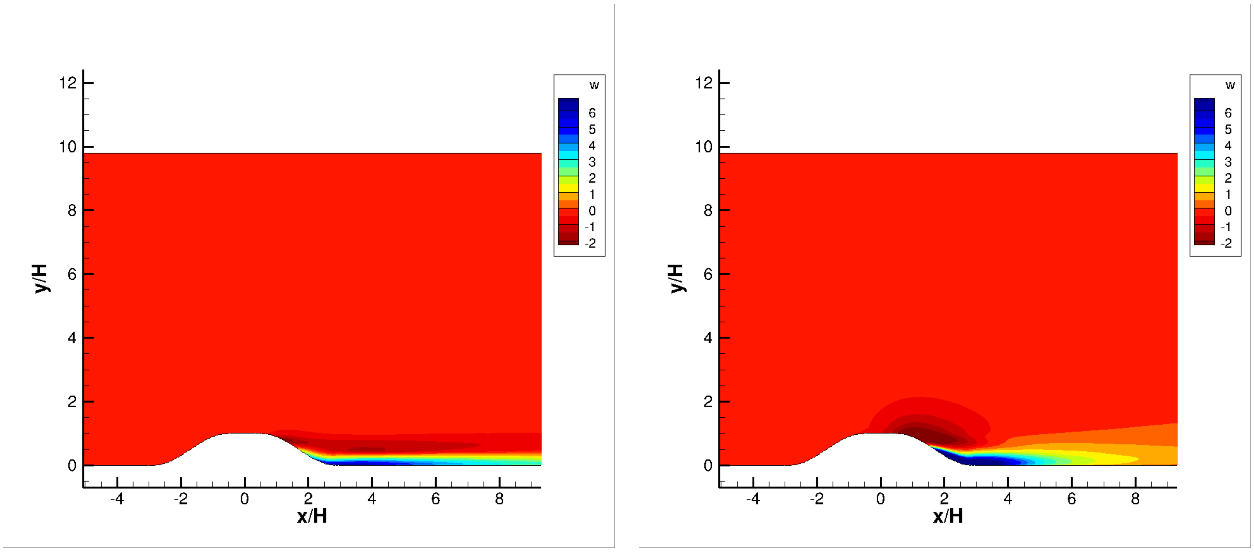

(a) W-Velocity for SA-neg

(b) W-Velocity for Menter $k-\omega$ SST (2003)

Figure 2.37: $Re_H = 250K$ Level 2 W-Velocity contours along the centerline $z/H = 0$ for the SA-neg turbulence model and the $k-\omega$ turbulence model.

The cross-flow velocity represented by the W-Velocity component is shown in Figure 2.37 where the SA model is shown in Figure 2.37a and the $k-\omega$ model is shown in Figure 2.37b. It is seen that the windward side of the hill shows little cross-flow and is consistent between the two turbulence models. Moving downstream, it is seen that the $k-\omega$ model predicts out of plane velocity to occur starting near the flat top region of the bump where the SA model does not start predicting any out of plane velocity until the separation region. The $k-\omega$ model predicts a single region of out of plane velocity that encompasses the entirety of the high curvature region near the bump top. The SA model, while occurring in a similar region, does not encompass the entire high curvature region and predicts a more elongated region of out of plane flow that extends downstream. This further supports the notion that the SA model is producing a single vortex that is being shed from the separation region as was seen on the surface plots while the $k-\omega$ model is predicting a much weaker vortex at this location and produces a separation bumble within the high curvature region by the tunnel wall. Moving to this high curvature region near the tunnel wall and into the region off of the bump. It is seen that the SA model produces an elongated region of in plane velocity that exists up to a distance of $y/H = 0.25$ off of the wall before transitioning to a more out of plane velocity. This further supports the notion that a vortex is being shed near the centerline after the bump for the SA model. Looking at the $k - \omega$ model, it is seen that a strong region of in-plane velocity is present starting around half way up the leeward side of the bump that extends downstream. It predicts that the in-plane velocity component will not be as elongated as compared to the SA model. This further shows the separation bump shaping seen by the $k - \omega$ model within the high curvature region near the tunnel wall.

Chapter 3

Discussion and Conclusions

The current computational status of the Virginia Tech BeVERLI case was presented. The following conclusions have been made based upon the analysis presented:

- The discretization error analysis shows that the strength of the separated region along with the movement of the separation location and surface foci leads to an increase in discretization error.

- The iterative error analysis showed that when using SENSEI, once the convergence criteria is met, the iterative error with the solution becomes negligible to the overall numerical error of the solution.

- The $Re_H = 250K$ case predicted the experimental data well along the centerline up until separation and predicted the experimental $C_{p,ref}$ data along the centerspan well with minor differences in the minimum $C_{p,ref}$ values.

- In an investigation of the asymmetry of the centerline $C_{p,ref}$ data showed that an increase of grid resolution leads to the coalescence of variations in asymmetry.

- The Level 1 grid is needed in order to properly resolve the $Re_H = 650K$ case.

- A recommendation moving forward is set that, if possible, a new grid is established that is tailored specifically towards the highest Reynolds number case.

- The effects due to a change in Reynolds number on the numerical solution produced no increased asymmetry trend for the SA $C_{p,ref}$ profiles and was inconsistent with what was seen experimentally.
- It is recommended that Reynolds number trends be reevaluated for the computational results after the Level 1 $Re_H = 250K$ case can be converged.
- When using the $k - \omega$ turbulence model, increasing $C_{p,ref}$ asymmetry along the centerspan with increasing Reynolds number was seen but the profiles themselves did not agree well with the experimental data at low Reynolds numbers.
- When using the same turbulence model, SENSEI predicts fewer surface focal points than Fluent within the separated region.
- The use of limiters does not affect the $C_{p,ref}$ profiles enough to justify the increase in computational cost without them.
- The van Leer limiter was identified as the best limiter option due to the similarities in the values of $C_{p,ref}$ obtained and the overall shaping of the subsequent profiles.
- As Reynolds number increased, the $k - \omega$ and SA models agreed more with each other for the $C_{p,ref}$ profiles and flow topology in the separated region than at lower Reynolds numbers.
- If SENSEI could converge the Level 1 $k - \omega$ case for the $Re_H = 650K$ condition, an improved agreement with experimental data may arise as was seen with the SA model.
- A streamwise slice along the centerline showed that the $k - \omega$ model predicted more spanwise flow than the SA model while the SA model predicted a larger region of low momentum flow after separation.

Appendix A

Appendix

The iterative error analysis results for the 3 locations within the volume solution that were extracted are presented here.

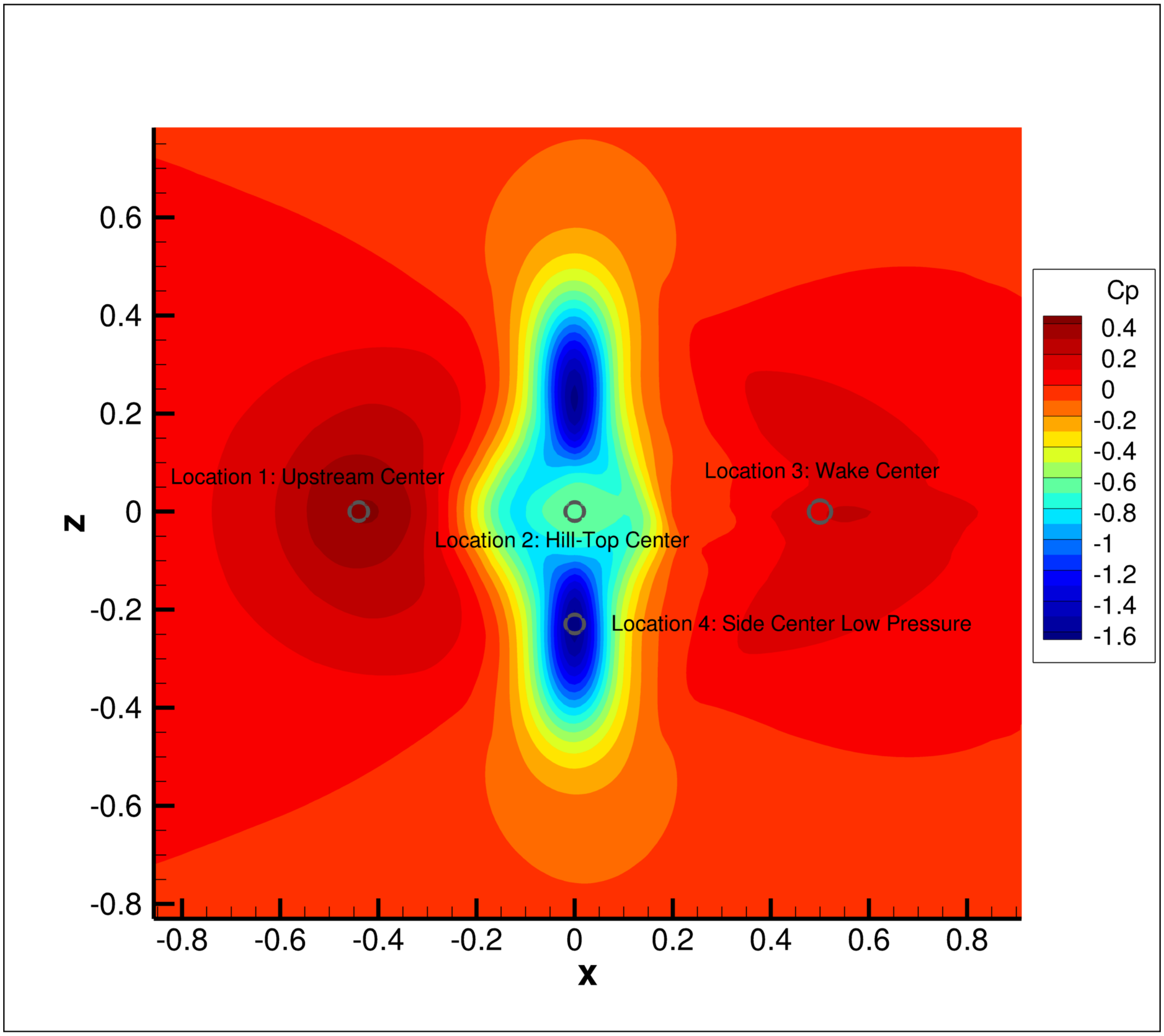

Figure A.1: Locations where the iterative error estimates were extracted.

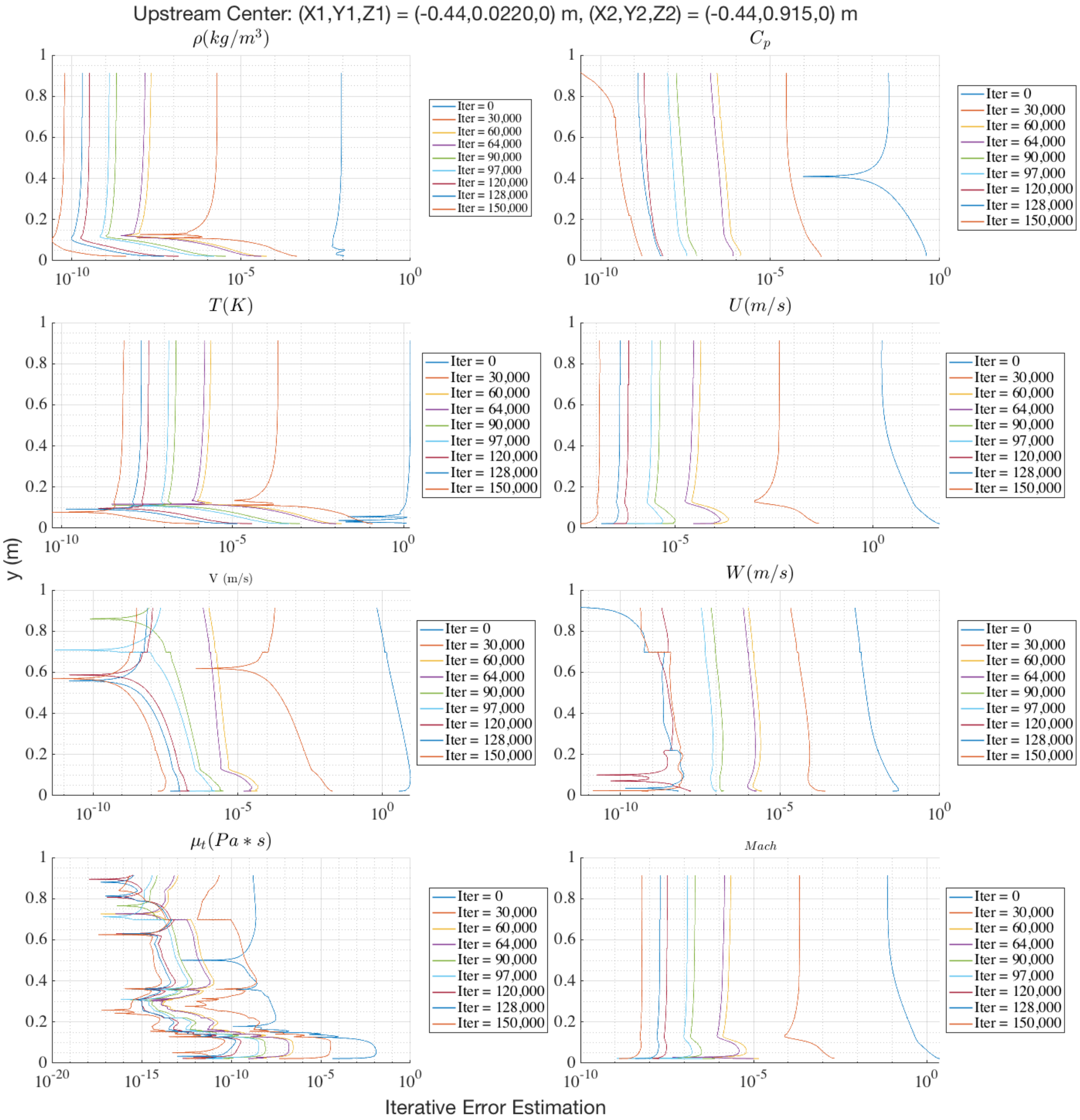

Figure A.2: Iterative error of $C_{p,ref}$ for the 45° case using Level 3 with $Re_H = 650K$ using the SA-neg turbulence model at the upstream bump center.

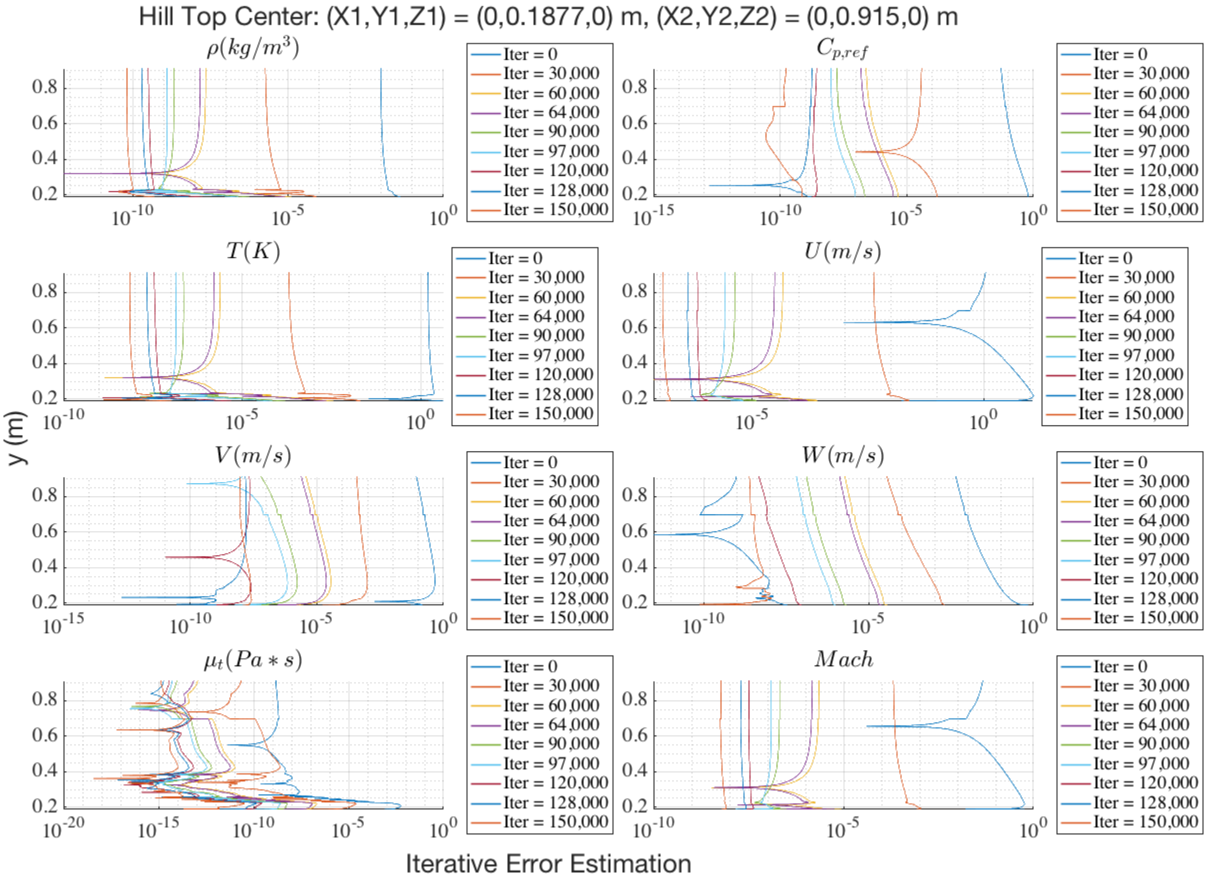

Figure A.3: Iterative error of $C_{p,ref}$ for the 45° case using Level 3 with $Re_H = 650K$ using the SA-neg turbulence model at the hill top center.

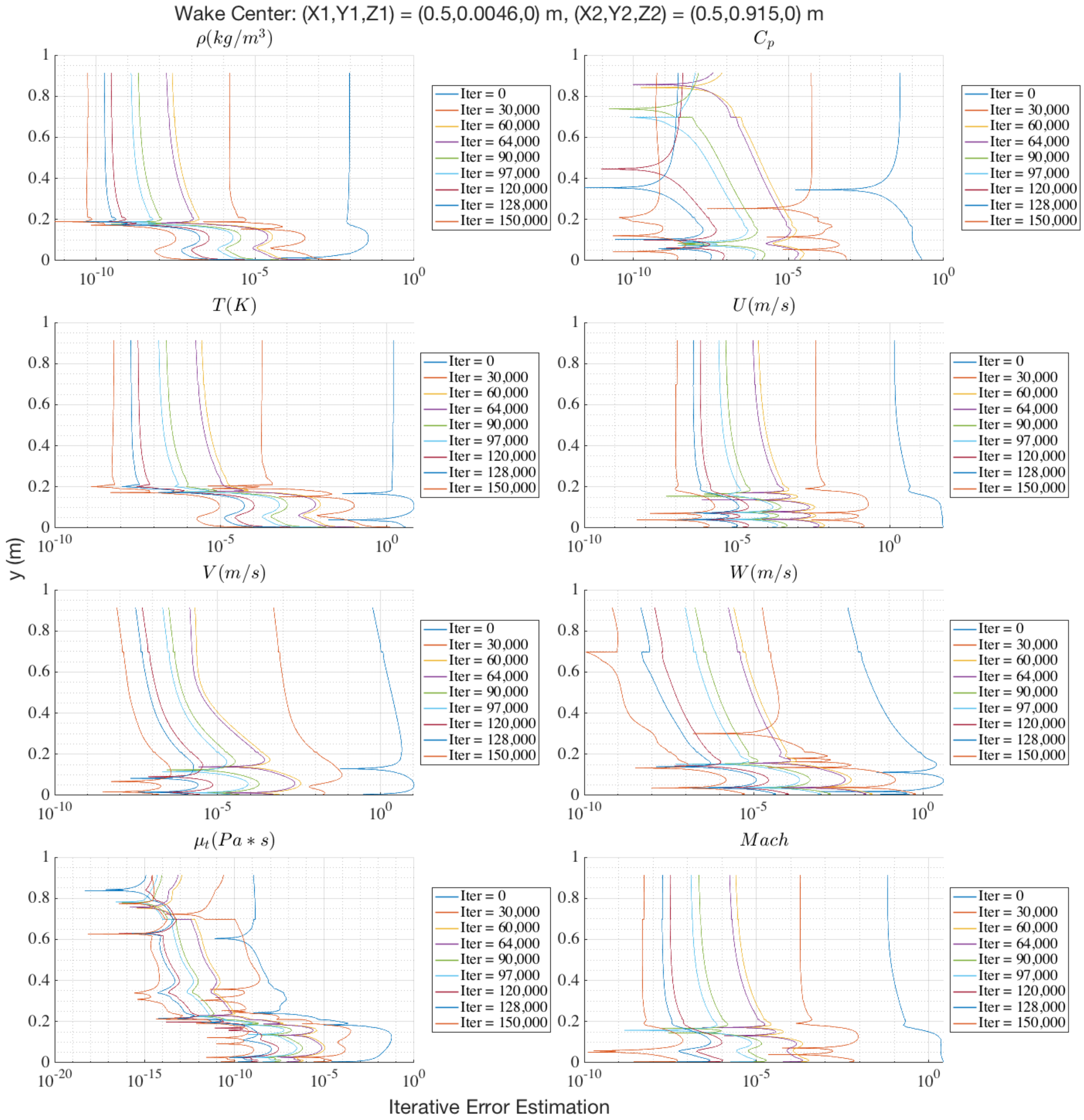

Figure A.4: Iterative error of $C_{p,ref}$ for the 45° case using Level 3 with $Re_H = 650K$ using the SA-neg turbulence model within the downstream wake center.

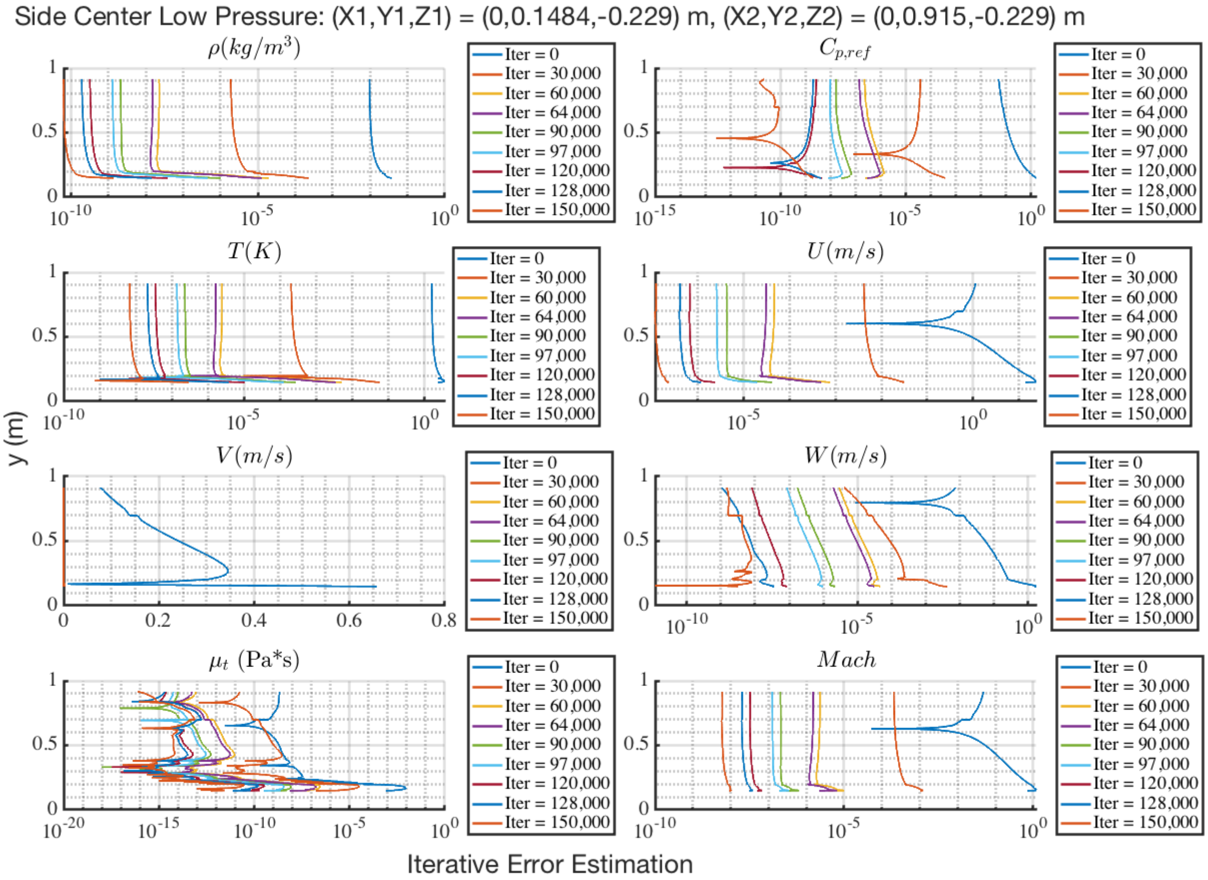

Figure A.5: Iterative error of $C_{p,ref}$ for the 45° case using Level 3 with $Re_H = 650K$ using the SA-neg turbulence model within the side low pressure region.

Bibliography

[1] Oberkampf, W. L., and Smith, B. L., "Assessment Criteria for Computational Fluid Dynamics Model Validation Experiments," *Journal of Verification, Validation and Uncertainty Quantification*, Vol. 2, No. 3, 2017, p. 031002.

[2] Spalart, P. R., "Philosophies and Fallacies in Turbulence Modeling," *Progress in Aerospace Sciences*, Vol. 74, 2015, pp. 1–15.

[3] Spalart, P. R., "Strategies for turbulence modelling and simulations," *International Journal of Heat and Fluid Flow*, Vol. 21, No. 3, 2000, pp. 252–263.

[4] Moin, P., and Kim, J., "Tackling Turbulence with Supercomputers," *Scientific American*, Vol. 276, No. 1, 1997, pp. 62–68.

[5] Bell, J., Heineck, J., Zilliac, G., Mehta, R., and Long, K., "Surface and Flow Field Measurements on the FAITH Hill Model," *50th AIAA Aerospace Sciences Meeting including the New Horizons Forum and Aerospace Exposition*, 2012, p. 704.

[6] Simpson, R. L., Long, C. H., and Byun, G., "Study of Vortical Separation from an Axisymmetric Hill," *International Journal of Heat and Fluid Flow*, Vol. 23, No. 5, 2002, pp. 582–591.

[7] Lowe, T., Borgoltz, A., Devenport, W. J., Fritsch, D. J., Gargiulo, A., Duetsch-Patel, J. E., Roy, C. J., Szoke, M., and Vishwanathan, V., "Status of the NASA/Virginia Tech Benchmark Experiments for CFD Validation," *AIAA SciTech 2020 Forum*, 2020, p. 1584.

[8] Gargiulo, A., Beardsley, C., Vishwanathan, V., Fritsch, D. J., Duetsch-Patel, J. E., Szoke, M., Borgoltz, A., Devenport, W. J., Roy, C. J., and Lowe, K. T., "Examination of Flow Sensitivities in Turbulence Model Validation Experiments," *AIAA SciTech 2020 Forum*, 2020, p. 1583.

[9] Sutherland, W., "LII. The Viscosity of Gases and Molecular Force," *The London, Edinburgh, and Dublin Philosophical Magazine and Journal of Science*, Vol. 36, No. 223, 1893, pp. 507–531.

[10] Pointwise, "Pointwise Manual," `https://www.pointwise.com/doc/user-manual/`, 2021. Accessed: 2021-05-28.

[11] Jackson, C. W., Tyson, W. C., and Roy, C. J., "Turbulence Model Implementation and Verification in the SENSEI CFD Code," *AIAA Scitech 2019 Forum*, 2019, p. 2331.

[12] Derlaga, J. M., Phillips, T., and Roy, C. J., "SENSEI computational fluid dynamics code: a case study in modern Fortran software development," *21st AIAA Computational Fluid Dynamics Conference*, 2013, p. 2450.

[13] Ansys, "FLUENT Manual," `http://www.afs.enea.it/project/neptunius/docs/fluent/html/ug/main_pre.htm`, 2019. Accessed: 2020-06-04.

[14] Weicheng Xue, W. C., and Roy, C. J., "Code Verification for Turbulence Modeling in Parallel SENSEI Accelerated with MPI," *AIAA Scitech 2020 Forum*, 2020.

[15] Roe, P. L., "Approximate Riemann Solvers, Parameter Vectors, and Difference Schemes," *Journal of Computational Physics*, Vol. 43, No. 2, 1981, pp. 357–372.

[16] Barth, T., and Jespersen, D., "The Design and Application of Upwind Schemes on Unstructured Meshes," *27th Aerospace Sciences Meeting*, 1989, p. 366.

[17] Allmaras, J. F. T., S. R., and Spalart, P. R., "Modifications and Clarifications for the Implementation of the Spalart-Allmaras Turbulence Model," *International Journal of Heat and Fluid Flow, Big Island, Hawaii*, 9-13 July 2012, pp. ICCFD7–1902.

[18] Menter, F. R., "Two-Equation Eddy-Viscosity Turbulence Models for Engineering Applications," *AIAA Journal*, Vol. 32, No. 8, 1994, pp. 1598–1605.

[19] Roache, P., *Verification and Validation in Computational Science and Engineering*, Hermosa Publishers, 1998. URL `https://books.google.com/books?id=ENRlQgAACAAJ`.

[20] Oberkampf, W. L., and Roy, C. J., *Verification and Validation in Scientific Computing*, Cambridge University Press, 2010.

[21] Duetsch-Patel, J. E., MacGregor, D., Jenssen, Y. L., Henry, P.-Y., Muthanna, C., Savio, L., Lavoie, P., Gargiulo, A., Sundarraj, V., Ozoroski, T., Roy, C. J., Devenport, W. J., Borgoltz, A., and Lowe, K. T., "The BeVERLI Hill Three-Dimensional Separating Flow Case: Cross-Facility Comparisons of Validation Experiment Results," *SciTech 2022 Forum*, San Diego, CA & Virtual, 2022.

[22] Michalak, K., and Ollivier-Gooch, C., "Limiters for Unstructured Higher-Order Accurate Solutions of the Euler Equations," *46th AIAA Aerospace Sciences Meeting and Exhibit*, 2008. doi: 10.2514/6.2008-776.

[23] peng Bai, F., hua Yang, Z., and gang Zhou, W., "Study of total variation diminishing (TVD) slope limiters in dam-break flow simulation," *Water Science and Engineering*, Vol. 11, No. 1, 2018, pp. 68–74. doi: https://doi.org/10.1016/j.wse.2017.09.004, URL `https://www.sciencedirect.com/science/article/pii/S1674237018300255`.